UiT
THE ARCTIC
UNIVERSITY
OF NORWAY

Faculty of Science and Technology
Department of Physics and Technology

Measuring velocities of a surge type glacier with SAR interferometry using ALOS-2 data

Truls Karlsen

EOM-3901 Master's thesis in energy, climate and environment 30 SP June 2021

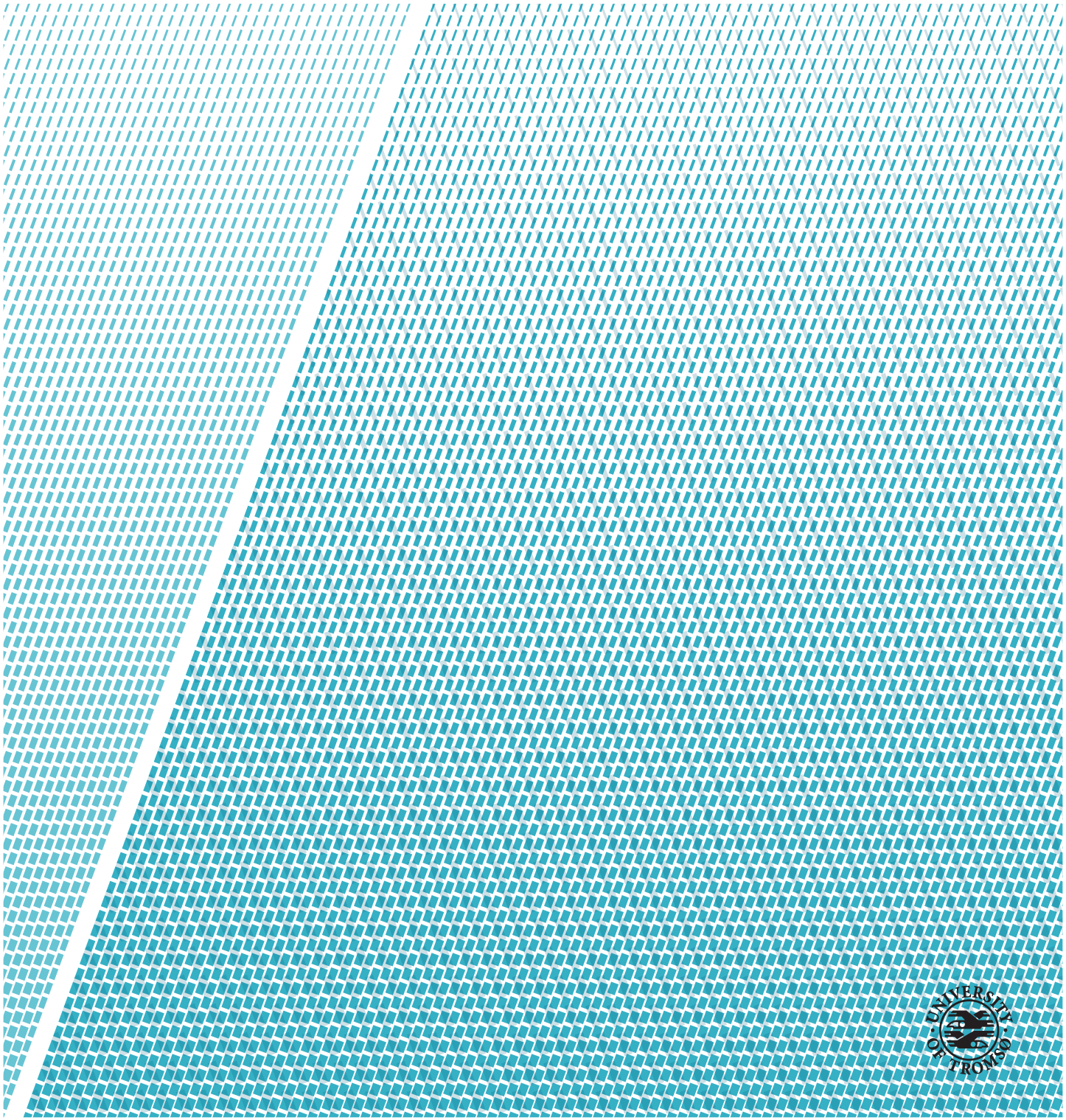

Abstract

In recent years, in-situ measurements on Kongsvegen, a surge-type glacier located in the Kongsfjorden area, have showed an acceleration in the flow speeds of the glacier. This could indicate the onset of a surging event, which presents the opportunity to study the dynamics of a glacier surge using remote sensing techniques with in-situ data for reference. Synthetic aperture radar (SAR) is well suited for this, as it does not rely on the sun for illumination and is not obstructed by clouds. In addition, SAR can be used to measure displacement with high accuracy and resolution through the use of interferometric SAR (InSAR).

This study investigates the acceleration of Kongsvegen using InSAR, MAI and offset tracking. Velocity measurements from the combination DInSAR - MAI are then compared to in-situ data as well as the offset tracking measurements. For image pairs where InSAR measurements are not possible due to phase decorrelation, offset tracking is attempted as a back-up. Data from 2015, 2018 and 2019 was available, and the evolution of flow speeds over time could therefore be evaluated. The image pairs from 2018-2019 were acquired with 14 days separation in time, while the 2015 image pairs were acquired with 28 and 42 days separation. Due to the longer separation in time, the 2015 image pairs decorrelated in time. In addition, a pair acquired in the summer of 2018 decorrelated as a result of surface melting on the glaciers. Therefore only 3 of the total 8 pairs available were suited for interferometric analysis.

For the image pairs from 2018-2019, the InSAR measurements were in good agreement with the in-situ data, as they also indicated an acceleration of the flow speeds on Kongsvegen. The offset tracking results on these pairs overestimated the velocity magnitudes, but also showed an increase in time. Similar to the InSAR estimates, the offset tracking failed to produce reasonable results on the 2015 image pairs, likely because of the large temporal baseline and lack of surface features on Kongsvegen. Overall, InSAR could be used to measure flow speeds on Kongsvegen successfully, but more data with a short temporal baseline is needed for an in-depth analysis.

Acknowledgements

First and foremost I would like to thank my supervisors Malin Johansson, Jelte van Oostveen, Geir Moholdt and Anthony Doulgeris. Working with you all has been a true pleasure, and without your expertise and tireless efforts to support me, this project would not have been possible.

The ALOS-2 PALSAR-2 scenes were provided by JAXA under the 2nd Research Announcement on the Earth Observations Collaborative Research Agreement (PI No: PER2AN013).

I would also like to give thanks to the Norwegian Polar Institute for providing in-situ data and to all those who participated in the different fieldwork experiments.

The "Centre for Integrated Remote Sensing and Forecasting for Arctic Operations" (CIRFA) is thanked for providing the software package Icedrift, a project supported by the Research Council of Norway (RCN project 237906).

Meteorological data was provided by the Norwegian Meteorological Institute, through the web portal; seklima.met.no.

I would like to give a huge thanks to my family. To my grandmother Rut, having an unlimited supply of cakes and coffee has been a lifesaver for a student, and I always look forward to visiting you. A big thanks also goes to my sister Marte, for guiding me through my first years as a student in Tromsø. Last but not least, to my dear parents Gøril and Torgeir, thank you for always supporting me in all my projects, big and small, and for always believing in me. I would not be where I am today without you.

To all my classmates, thank you for all the hours spent drinking coffee. You helped make life as a master's student enjoyable and I could not have wasted so much time in a better way.

Truls Karlsen
Tromsø, June 2021

Contents

List of Figures

List of Tables

1

Introduction

Since the turn of the 20th century, the global annually averaged surface temperature has increased by approximately 1.0° C as a result of anthropogenic greenhouse gas emissions [1]. In response to this warming, glaciers worldwide are losing mass at a rate unprecedented in modern time. This has major implications for the global climate, as increased glacier melt and calving rates are major contributors to global sea level rise (SLR), which can have catastrophic consequences for people living in coastal areas around the world. In addition, surface melt on glaciers darkens the glacier surface. This reduces the amount of solar irradiation reflected by the glacier surface, which leads to an increase in surface temperatures, further increasing surface melt [2].

In response to the increase in global temperatures, an acceleration of the flow speeds of ocean terminating glaciers (tidewater glaciers) in Svalbard has been observed [2]. The acceleration of flow speeds increases the mass loss from these glaciers as the amount of ice discharged to the ocean through a process known as calving increases, contributing further to SLR [2]. Measuring glacier flow speeds is therefore important for assessing the contribution from glaciers to SLR.

As most glaciers are located in remote and hazardous regions, measuring flow speeds in-situ can be challenging [3]. Remote sensing is therefore a valuable tool, as it can supply data routinely with global coverage. Glacier flow speeds have successfully been measured from both synthetic aperture radar (SAR) and

optical remote sensing platforms (see for example [4] and [5]). Two techniques for measuring glacier flow speeds from remote sensing data are interferometric SAR (InSAR) and offset tracking.

InSAR techniques have previously been used to measure glacier flow successfully (see for example [6], [7] [8]), and can deliver displacement measurements at cm accuracy. A major limitation of InSAR is however changes in surface properties, which decorrelates the signals used. This is particularly challenging for velocity measurements on snow covered glaciers, as the snow cover is easily affected by changing meteorological conditions. For this application, the L-band SAR sensor Phased Array type L-band Synthetic Aperture Radar 2 (PALSAR-2) carried by the Advanced Land Observing Satellite 2 (ALOS-2) satellite presents a promising option, as it operates with a longer wavelength (L-band) than other systems such as Sentinel-1 (C-band). This is beneficial for InSAR, as longer wavelength signals can penetrate deeper into snow, which reduces phase decorrelation due to changing surface properties [9].

Offset tracking is a technique based on estimating the displacement of small patches in images acquired at different times. As with InSAR, offset tracking is also an established technique for measuring glacier flow speeds (e.g. [4, 5, 9]). In this study, offset tracking will mainly be used for comparisons with InSAR, but will also be used as an alternative in situations where InSAR fails to produce reliable velocity estimates.

The focus of this study will be to use both InSAR and offset tracking for measuring flow speeds on the glacier Kongsvegen. Kongsvegen is a surge type tidewater glacier located in the vicinity of Ny-Ålesund, where in-situ measurements have been made since 1987 by the Norwegian polar institute (NPI). A surge type glacier is characterized by long periods of slow movement, followed by shorter periods of high flow speeds [10]. In-situ measurements provided by NPI is also used for comparisons with the remote sensing velocity estimates where possible. As the in-situ measurements on Kongsvegen indicate an acceleration over the past 15 years, the main goal of this study is to investigate if it is possible to observe this acceleration using remote sensing techniques.

While Kongsvegen is accelerating, a surging event is not yet initiated. The flow speeds on Kongsvegen are therefore still relatively slow $\left(\sim 15\,\mathrm{m\,a^{-1}}\right)$. A secondary goal of this study is therefore to compare the performance of InSAR and offset tracking on Kongsvegen, to see how the techniques perform on a slow moving glacier.

In chapter 2 the relevant theory on electromagnetism (EM) and SAR will be presented. Chapter 3 will contain a description of the techniques used for measuring velocities. Relevant glacier theory and a description of the glacier

studied, as well as the area it is located in, will be presented in chapter 4. Chapter 5 contains information about the data used in this study. A description of the methods used will be given in chapter 6, while the results obtained will be presented in chapter 7. This includes the results from InSAR, as well as the results from the combination of InSAR and MAI and from offset tracking. In chapter 8, the achieved results will be evaluated and compared to the in-situ data. Known limitations and sources of error will also be discussed. Finally, the study will be summarized in chapter 9, where possible future work also will be presented.

2

SAR Theory

In this chapter, relevant theory about SAR for this project will be presented. As SAR operates by transmitting and receiving EM radiation, a basic introduction to EM is required. This chapter will therefore start with a brief introduction to some key aspects of EM theory.

An EM wave can be expressed as:

$$\boldsymbol{E} = \boldsymbol{A}e^{i(kr-\omega t+\varphi)} \tag{2.1}$$

where $\boldsymbol{E}$ is the electric field vector, $\boldsymbol{A}$ is the amplitude of the wave, $k = 2\pi\sqrt{\epsilon_r}\lambda^{-1}$ is the wave vector in the propagation medium, λ is the wavelength of the EM wave, ω is the angular frequency of the wave $\left(\omega = 2\pi c\lambda^{-1}\right)$ and φ is the phase of the wave. Here, c denotes the speed of light in vacuum and ϵ_r is the relative permittivity. The term $(kr - \omega t + \varphi)$ is referred to as the phase term, which from here on is denoted as ϕ [11].

The relationship between the frequency and wavelength of a sinusoidal wave travelling at constant speed v is given as

$$\lambda = \frac{v}{f} \tag{2.2}$$

where λ is the wavelength of the wave and f is the frequency of the wave. For an EM wave travelling in vacuum, the speed of the wave is c.

2.1 Fundamentals of SAR

A SAR is, as its name suggests, a radar system where the forward motion of a radar is used to synthesize a larger aperture than the physical aperture. This allows a SAR system to image the Earth at a high spatial resolution from orbit. A SAR sensor is an active system, meaning that it both transmits and receives signals. As such, factors such as the ratio between transmitted and received power, phase and polarization can be controlled, which can be used to extract useful information about the scene imaged [12].

The image resolution of a SAR in the heading direction (azimuth or along track) is given as

$$X_{\text{Az}} = \frac{1}{2}L \tag{2.3}$$

where L is the length of the radar antenna. As the length of a radar antenna is usually on the order $L \sim 10^1$ m, this results in an azimuth resolution on the order $X_{\text{Az}} \sim 10^1$ m, regardless of the wavelength of the system [11].

The resolution in the direction perpendicular to the antenna (range or across track) on the ground is given as

$$X_{\text{gr}} = \frac{c\tau}{2\sin\theta} = \frac{c}{2B\sin\theta} \tag{2.4}$$

where τ is the length of the radar pulse and B is the bandwidth of the transmitted pulse. τ and B are related as $\tau = \frac{1}{B}$. This will be referred to as the slant range resolution. The range resolution in radar coordinates (azimuth, range), referred to as slant range resolution, is given as

$$X_{\text{sr}} = \frac{c\tau}{2} = \frac{c}{2B} = X_{\text{gr}} \cdot \sin\theta \tag{2.5}$$

The slant range and range resolution only differs by the factor $\frac{1}{\sin\theta}$, which is the projection of the radar pulse onto the ground [11].

In an active microwave imaging system, the time a pulse uses to travel from the antenna to a point and then back to the antenna again is referred to as the round-trip time. The round-trip time is used to discriminate between points in the range direction. The system must therefore be side-looking, as it can only measure total distance, and can not discriminate between left and right [11]. The geometry of a SAR system can be seen in Figure 2.1, with key aspects such as the look angle (θ), azimuth and range and the imaged area (swath) highlighted.

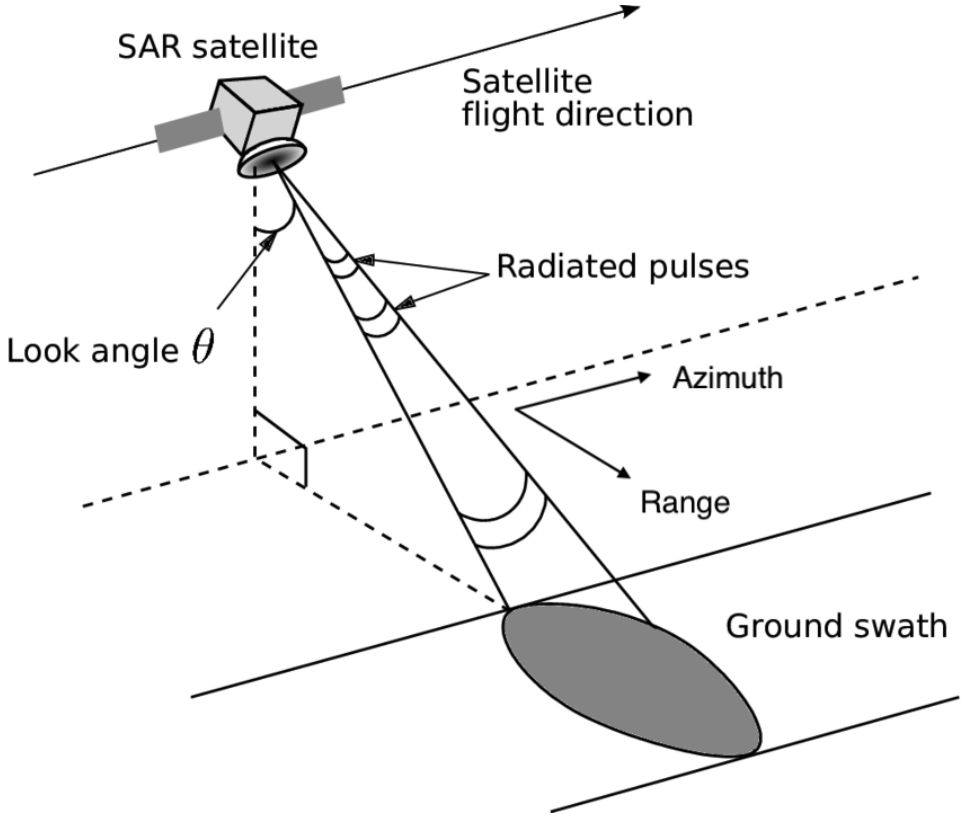

Figure 2.1: The geometry of a SAR system. The flight direction (azimuth or along-track) and the look direction (range or across-track) is shown, as well as the area imaged by the system (swath). Modified from Lauknes (2011) [13].

In a SAR, both the amplitude and phase of the backscattered EM radiation is measured. The received phase follows a uniform distribution on the form

$$\phi \sim U(0, 2\pi) \tag{2.6}$$

where $U(a, b)$ denotes a uniform distribution between a and b. The phase

component of a single SAR scene is therefore random, and does not convey any meaningful information about the scene. The phase difference between two or more SAR scenes can however be used to extract useful information, such as topography or displacement with high accuracy [14]. This will be further explained in section 3.2.

The resolution of a SAR image is typically in the range $10^0 - 10^1$ m, while the wavelength of the radar beam is typically on the order $10^{-2} - 10^{-1}$ m. As the dimensions of a pixel in the SAR image are significantly larger than the wavelength of the system, the returned signal is the sum of the return of the independent scatterers contained in the pixel area. This is the source of the effect referred to as speckle. Speckle is an effect that has a salt and pepper noise-like appearance, but as it is a part of the measured signal it is not actual noise. Speckle is a result of constructive or destructive interference between the returns from the scatterers contained in a resolution cell. This can degrade the visual appearance of an image, but the visual degrading can be reduced by processes such as multi-looking or averaging [12].

Another benefit of SAR is that since it is an active system, it does not rely on an external source of illumination. There is also low atmospheric interaction with EM waves in the microwave region, which is the region where SAR operates. This means that SAR systems can view the surface of the Earth regardless of external conditions such as weather and sun illumination, which are limiting factors for optical imaging systems [12]. This is particularly useful in the polar regions of the Earth, as there is a limited amount of sunlight during large parts of the year.

2.2 SAR Data

SAR data can generally be divided into three categories: level-0, -1 and -2 data. Level-0 data refers to raw SAR-data, level-1 data is focused SAR data and level-2 consists of products derived from level-1 data. In this study, level-1 data will be used. Level-1 data consists of two sub-categories: single look complex (SLC) data and ground range detected (GRD) data. SLC data is complex, thus the phase information of the signal is preserved and therefore suitable for interferometric applications. GRD data on the other hand only contains amplitude information, and can therefore not be used with interferometric techniques. The advantage of GRD data is that it is projected to ground range and terrain corrected, which makes it more visually intuitive. GRD data is also multi-looked, which reduces speckle and creates an image with approximately square pixels. This does however degrade the spatial resolution of the image [15].

2.3 Penetration Depth

The relationship between the ability of EM wave to penetrate a medium and the wavelength of the EM wave is given as

$$d_p = \frac{\lambda}{4\pi N_i} = \frac{c}{4\pi f N_i} \tag{2.7}$$

where d_p is the penetration depth, also referred to as skin depth and N_i is the imaginary part of the complex index of refraction, $n = N_r + iN_i$ [11]. From this expression it can be seen that penetration depth is proportional to the wavelength of an EM wave, and must therefore be inversely proportional to the corresponding frequency. Some common radar frequencies are listed in Table 2.1, which gives an indication of the ability of different SAR systems to penetrate a given medium, compared to each other. Penetration depth is also dependent on incidence angle, which is the angle between the surface normal and the incident radar beam, with greater penetration at steeper angles. [12].

Table 2.1: Overview of common radar frequency bands for SAR [16]

Frequency band	Frequency range [GHz]	Wavelength range [cm].
P	0.25 - 0.5	60 - 120
L	1 - 2	15 - 30
S	2 - 3.75	8 - 15
C	3.75 - 7.5	4 - 8
X	7.5 - 12	2.5 - 4
Ku	12 - 17.6	1.7 - 2.5
Ka	25 - 40	0.75 -1.2

SAR systems carrying lower frequency P- or L-band radars would therefore penetrate further into a medium than other commonly used radar frequencies in SAR applications, such as C- or X-band. This is beneficial in glacier flow studies, especially in cases where the glaciers are covered by snow. As the characteristics of snow covered surfaces change rapidly due to meteorological effects, which decorrelates radar signals, deeper penetration could increase the coherence between images acquired at different times [5]. The coherence is increased as longer wavelength signals penetrate further through the snow cover into glacier ice, where surface characteristics are more stable in time [17]. Rignot et al. (2001) found that L-band signals penetrated $5 - 10$ m deeper than C-band signals over most forms glaciated terrain, and $60 - 120$ m deeper on smooth cold exposed ice [18].

2.4 Polarization

The polarization of an EM wave refers to the direction the corresponding electric field oscillates in. Three main types of polarization exists, linear, elliptical and circular polarization [11]. The polarization of the transmitted SAR signal is determined by the orientation of the radar antenna, while the polarization of the return signal is influenced by the surface viewed. As the polarization of the transmitted signal is known, the polarization of the received signal can be used to gather information about surface properties. Different configurations for transmitting and receiving exists, with the most common being single-polarization, dual-polarization and quad-polarization. In these configurations, the antenna can be in horizontal (H) or vertical (V) position. Single-polarization refers to transmitting and receiving on the same polarization, dual-polarization refers to transmitting on one polarization and receiving on both, while quad-polarization refers to transmitting and receiving on both polarizations. HH polarization refers to transmitting and receiving on H polarization, HV refers to transmitting on H and receiving on V, etc. [11]. A newer configuration referred to as compact-polarization consists of transmitting either on H + V or circular polarization and receiving on H and V [19].

2.5 Terrain Correction

Because of the side-looking configuration of SAR systems, geometric distortions related to topography can occur in SAR images. The three main sources of geometric distortions in SAR images are foreshortening, layover and shadowing. These distortions depends on the topography of the imaged area, as well as the look angle of the imaging system. Foreshortening occurs in areas of modest topography, and causes slopes to appear steeper in the near-range portion of the image and shallower in the far-range portion of the image. Layover occurs in more rugged terrain, where the return signal from the top of an object reaches the satellite before the return signal from the base of the object. In slant-range geometry, this causes the top of the object to appear closer to the receiving antenna than the base does, while the top and base appears to occupy the same space in ground range. Shadowing occurs when an object blocks the radar beam such that areas behind the object are not. This manifests as black regions in radar images [12]. Terrain correction is used for correcting these geometric distortions. In addition, terrain correction is also required for comparison between SAR data and external sources of information, such as digital elevation models (DEMs), field data and external remote sensing data [20].

A common method for terrain correcting SAR images is the Range-Doppler

(RD) method [20]. The RD method is based on solving the Doppler and range equations to determine the position in radar coordinates that corresponds to a given position on Earth. A detailed description of the RD terrain correction method can be found in [21]. The transformation to map geometry position from radar coordinates is known as geocoding. For geocoding the image, an external DEM is used. DEMs are represented in a 2D cartographic (northing, easting) system or a geographic system (latitude, longitude). For geocoding, the DEM is transformed from its original reference system to a cartesian representation (x, y, z). The SAR image is usually multi-looked such that the pixels are approximately square before geocoding [21].

3

SAR Interferometry and Offset Tracking

This chapter will present a description of the methods used for measuring displacement, interferometric SAR (InSAR), multiple aperture InSAR (MAI) and offset tracking, used in this study. As InSAR is the man focus of this study, a more detailed description of this method compared to the other methods will be given.

InSAR refers to a group of techniques where phase differences between SAR images acquired from different positions or at different times are used to extract information such as topography and displacement within the scenes imaged. InSAR has been used to measure surface displacement at millimeter accuracy [6] and to create high resolution DEMs [22].

To produce an interferogram, two SAR images of the same area acquired from different positions or at different times are required. The InSAR technique involving two images acquired simultaneously but separated in space is referred to as single-pass interferometry. Single-pass interferometry can be performed on two images separated in across-track or along-track direction (see Figure 2.1), referred to as across-track interferometry and along-track interferometry. Using two images acquired at separate times is referred to as repeat-pass interferometry. Repeat-pass interferometry utilizes the retracing of trajectories by satellites in orbit, which enables images from nearly the same viewing point

but separated in time to be acquired [23].

Differential SAR interferometry (DInSAR) refers to InSAR products where either the phase variation from the altitude variations of targets or the phase contribution from the displacement of scatterers has been removed from the interferogram. The DInSAR application where displacements have been removed is used for measuring topography, and is performed by subtracting two interferograms covering the same area, but acquired at different times. By assuming that the displacement in the scene is the same for both interferograms, the difference between the two interferograms should contain only information about the topography in the scene [24]. As displacement measurements are the main focus of this study, this technique will not be discussed any further, and DInSAR will from here on refer to the technique for measuring surface displacement. DInSAR is the technique most commonly used in repeat-pass interferometry [25] when measures of surface displacements are of interest. In general, InSAR is more sensitive to surface displacement than to topography [23].

3.1 Coregistration

The first step in InSAR processing is coregistration. This refers to the alignment of two images from the same geometry, such that the overlapping pixels in the images correspond to the same areas on the ground. The image that is aligned is referred to as the secondary image, while the image used as a reference is referred to as the reference image. After coregistration, both images are in the reference image geometry. For InSAR purposes, subpixel accuracy in coregistration is required in order to obtain useful interferograms. It is also important that movement within the scene does not affect the coregistration [5]. An accuracy of 0.1 pixel is widely considered sufficient for conventional stripmap data [17].

Among many different types of coregistration, the processing software Sentinel Application Platform (SNAP) [26] offers 3 options: cross-correlation (CC) based coregistration, DEM-assisted coregistration and DEM-assisted coregistration with cross-correlation. A description of the three methods will be given in the following subsections, starting with CC based coregistration.

A common method used for the coregistration of two images is based on using CC to detect offsets between the images. This is usually performed in two steps: an initial coarse coregistration and shift of the secondary image, followed by a fine coregistration. In the coarse coregistration, the offset between the reference and secondary image is determined on pixel level accuracy, whereas the fine

coregistration determines the offset between the reference and secondary image on subpixel level accuracy. The CC based coregistration operates by segmenting the reference image into patches around selected ground control points (GCPs), and finding the patch in the secondary image that gives the highest correlation. By calculating the correlation between the patch in the reference image and every patch in the secondary image, a correlation surface is formed. To increase the accuracy of the coregistration, the correlation surface can be upsampled [4][27]. For the coarse coregistration in SNAP, a large patch size is used, while the correlation surface is upsampled with a small number of points. A smaller patch size is used in fine coregistration, while the correlation surface is upsampled with a large numper of points.

After the subpixel offset between the reference and secondary image is determined, the secondary image must be transformed to the geometry of the reference image, such that the two images overlap. This is achieved by applying a set of transformation equations to the secondary image, where the coefficients are estimated from the offset derived from the fine coregistration. The order of the equations depends on how much the two images overlap. For images with only a small difference in geometry, a first order polynomial is sufficient, while a higher degree polynomial may be required if the difference is large. A second order transformation is required if highly distorted images are used. The amount of parameters in the equations also depends on the degree of offset. The transform equations for a first order transformation are on the form

$$\begin{aligned} x_s &= x_m + ax_m + by_m + c \\ y_s &= x_m + dx_m + ey_m + f \end{aligned} \tag{3.1}$$

where (x_s, y_s) is the position in the secondary image and (x_m, y_m) is the corresponding position in the reference image. The first order coefficient for y can in many cases be omitted, as the offset between images in azimuth is often negligible. After the transformation equations have been determined from the coregistration, the secondary image can be resampled to the reference image geometry. Different methods of resampling exists, such as nearest neighbour interpolation, bilinear interpolation and cubic convolution [12][27].

Another method for coregistering images is DEM-assisted coregistration. This method often performs better than the CC based method in areas with large topographic differences. In DEM-assisted coregistration, the similarity between the reference and secondary image is calculated using orbital data and a reference DEM as additional data sources. For comparisons between the reference and secondary images and the DEM, the DEM is transformed to radar coordi-

nates, a process referred to as radarcoding. The precision of the applied DEM is a source of error in the DEM-assisted coregistration method. Another source of error, although not as significant as the precision of the DEM, is the accuracy of the radarcoding of the DEM [28]. A major drawback of using the DEM assisted coregistration approach is that it is computationally more expensive than the standard CC based method for coregistration, as the offset between the reference and secondary image is estimated for each pixel [29].

A third method for performing coregistration combines the two previous methods. This is referred to as DEM-assisted coregistration with CC. In this method, a DEM-assisted coregistration is performed on the image pair, followed by a CC based coregistration on the coregistered pair. As coregistration is performed twice in this method, it is more computationally expensive than the previous methods. A comparison of the performance of the three methods is presented in section 6.1.1.

3.2 Interferogram

After a precise coregistration of the secondary image to reference image geometry is performed, the phase difference between the reference and secondary image can be computed. The phase difference is calculated for each pixel, and the resulting image is referred to as the interferogram.

As SAR data is complex, the phase can be calculated as the argument of a complex variable. The phase difference between the reference and secondary image at pixel location (x, y) is therefore given as

$$\Delta\phi(x,y) = \arctan\left(\frac{\mathrm{Im}\big(I_R(x,y)\,\bar{I}_S(x,y)\big)}{\mathrm{Re}\big(I_R(x,y)\,\bar{I}_S(x,y)\big)}\right) \tag{3.2}$$

where I_R is the reference image, I_S is the secondary image and $\bar{I}$ denotes the complex conjugate of an image I [25][30].

The phase difference between two complex SAR images can be modelled as

$$\Delta\phi = \Delta\phi_{\text{flat}} + \Delta\phi_{\text{topography}} + \Delta\phi_{\text{displacement}} + \Delta\phi_{\text{noise}} \tag{3.3}$$

where $\Delta\phi$ is the total phase difference, $\Delta\phi_{\text{flat}}$ is the phase contribution from

the curvature of the Earth, often referred to as the flat Earth contribution, $\Delta\phi_{\text{topography}}$ is the phase contribution from the topography of the terrain, $\Delta\phi_{\text{displacement}}$ is the phase contribution from displacement within the scene and $\Delta\phi_{\text{noise}}$ is the phase contribution from varying noise sources. Noise sources include interactions with the neutral atmosphere and the ionosphere, thermal noise and changes in the surface properties of scatterers [31]. For displacement applications, $\Delta\phi_{\text{displacement}}$ is the signal of interest. The remaining phase terms must therefore be removed, or assumed negligible.

If a scatterer changes its location between reference and secondary image, the resulting change in the interferometric phase is given as

$$\Delta\phi_d = \frac{4\pi}{\lambda} d \tag{3.4}$$

where d is the displacement of the scatterer projected on the slant range direction. The topographic phase contribution is given as

$$\Delta\phi_{\text{topography}} = -\frac{4\pi B_n q}{\lambda R \sin\theta} \tag{3.5}$$

where B_n is the perpendicular baseline between the reference and secondary image, q is the altitude difference between point targets, R is the distance from the satellite to a point target and θ is the beam incidence angle [25]. An in depth description of the remaining phase terms can be found in [25] and [30].

3.2.1 Phase Noise

In the ideal case, each resolution cell in a SAR image would contain only one dominant scatter that was stable in time. In reality, this is not the case. As such, each pixel in a SAR image contains many scatterers, with characteristics that can change over time, independently of each other. These changes can introduce phase noise in the interferograms. While it is not possible to remove this source of phase noise, it is possible to improve the temporal correlation between images by increasing the wavelength of the signal. As longer wavelength signal can penetrate deeper into surfaces (Eq. 2.7), where the scatterers are less affected by external factors and are therefore more stable over time, the temporal correlation is improved. This is particularly useful for glaciers covered by snow, as the snow cover changes rapidly, while the glacier ice beneath is more stable [9].

Other important sources of noise for DInSAR are atmospheric interactions (ionospheric effects and tropospheric delay) and thermal noise. While it is currently impossible to remove the thermal noise [32], several techniques exists for removing the influence of the atmosphere on interferograms. Tropospheric delay is caused by interactions between the troposphere and the radar signals. Several methods exists for estimating and correcting for the influence of the neutral atmosphere on phase measurements, which are described in detail in [33].

Signal delay caused by ionospheric disturbances is proportional to the total electron content (TEC) of the ionosphere, as well as the squared wavelength of the signal. L-band SAR is therefore more susceptible to ionospheric disturbances than for instance C-band or X-band SAR [34]. These ionospheric disturbances are most severe close to the auroral zones around the northern and southern magnetic poles, and often manifest as so-called azimuth streaks in interferograms and coherence images. Ionospheric disturbances cause errors mainly in azimuth direction as the disturbances affects the travel time of radar signals, which is used for focusing SAR images. This causes a pixel shift in azimuth direction, which for L-band data can be several pixels. Such a shift can have considerable effects on the coregistration of an image pair, which in turn degrades the coherence of the signal [35].

3.3 Noise Filtering

To lower the amount of phase noise present in interferograms, an adaptive filtering algorithm commonly referred to as the Goldstein phase filter is often applied. This algorithm is based on dividing the interferogram into overlapping patches, and computing the power spectrum for each patch by smoothing the intensity of its 2-D fast Fourier transform (FFT). The Goldstein phase filter algorithm is described in detail in [31].

Another technique used for reducing phase noise in interferograms is multi-looking. Multi-looking the interferogram refers to averaging over neighbouring pixels, which improves the signal-to-noise ratio (SNR). This procedure has the added benefit of creating square pixels in the interferogram [14]. Multi-looking is however unable to remove noise from spatially correlated sources, such as atmospheric effects and errors in flattening and topographic phase removal [30]. In addition to noise reduction, multi-looking the interferogram reduces computational costs, as the number of pixels is decreased. This is particularly important for phase unwrapping (see section 3.6), as this is a computationally expensive operation. This does however lower the spatial resolution of the interferogram and the measurements derived from it.

3.4 Orbital Errors

Removing of the flat earth phase contribution (Eq. 3.3) is referred to as flattening the interferogram. For performing this operation, the orbital information of satellites is used [25]. Inaccuracies in the orbital data therefore leads to errors in the interferogram flattetning. These errors manifest as long-wavelength signals which causes a ramping effect in the unwrapped interferogram. The phase contribution from orbital errors is therefore often referred to as a phase ramp, which can be modelled on the form

$$\hat{\phi}^{\text{orbit}}(x, y) = a_0 + a_1 x + a_2 y \tag{3.6}$$

where (x, y) is the position in the interferogram given in radar coordinates and a_0, a_1, a_2 are the coefficients of the phase ramp. If no precise orbital information is available, the orbital errors can be accounted for by estimating this phase ramp [36].

Several methods exists for compensating for orbital errors, such as estimating the coefficients of the phase ramp in the frequency domain or estimating the phase ramp from the unwrapped phase in the spatial domain using a least squares (LS) approach. The spatial method for removing orbital errors is based on modeling the orbital errors as a polynomial, usually of the 1^{st} or 2^{nd} degree. These models will be referred to as linear and quadratic models from here on. For estimating the coefficients of these models, the unwrapped phase values are used [36][37][38]. Only the methods based in the spatial domain will be used in this project, as they are simple to implement.

Linear Model

The linear model is given by Eq. 3.6. For the spatial method, the ramp coefficients are estimated using a LS approach:

$$A = \left(B^T B\right)^{-1} A^T \Phi \tag{3.7}$$

where $A = \begin{bmatrix} a_0 & a_1 & a_2 \end{bmatrix}$ is the 3×1 vector containing the coefficients to be determined, $B = \begin{bmatrix} \underline{1} & \underline{X} & \underline{Y} \end{bmatrix}$ is the $N \times 3$ coordinate matrix containing a $N \times 1$ column of ones to account for the constant term, as well as the coordinates of the N phase values, $\underline{X}_{N\times 1}, \underline{Y}_{N\times 1}$, used in the estimation, and Φ is a $N \times 1$ vector containing the phase values used in the estimation. A drawback of this method is that it is susceptible to unwrapping errors. It also does not take into

consideration the quality of the interferogram, but this can be accounted for by introducing a weighting matrix [36][37][38].

Quadratic Model

The previous method is based on the assumption that the orbital error is linear. If this is not the case, a nonlinear error model could be required. Even though high order polynomials will account for small scale errors better than a quadratic model, they introduce oscillations which cause computational error. The quadratic model is therefore a popular choice for orbital error removal. The quadratic model is on the form

$$\hat{\phi}^{\text{orbit}}(x,y) = a_0 + a_1 x + a_2 y + a_3 xy + a_4 x^2 + a_5 y^2 \tag{3.8}$$

The coefficients in this model can also be estimated using a LS approach, as described in Eq. 3.7. For the quadratic model, the coordinate matrix is given as $B = \begin{bmatrix} \underline{1} & \underline{X} & \underline{Y} & \underline{XY} & \underline{X^2} & \underline{Y^2} \end{bmatrix}$ [37].

3.5 Coherence

The influence of phase noise on the interferogram can be estimated from the coherence image. Coherence is a measure of the phase similarity, calculated as a cross-correlation between two complex SAR images over small patches of the images. Assuming that the scatterers present in the images follow a Gaussian distribution [39], the coherence can be estimated as

$$\Delta\Omega(x,y) = \frac{\left\langle I_1(x,y)\,\bar{I}_2(x,y)\right\rangle}{\sqrt{\left\langle I_1(x,y)\,\bar{I}_1(x,y)\right\rangle \left\langle I_2(x,y)\,\bar{I}_2(x,y)\right\rangle}} \in [0,1] \tag{3.9}$$

where I_1 and I_2 are two complex SAR images and $\langle\rangle$ denotes the average over a small image patch.

Loss of coherence for glacier surfaces could be caused by rapid incoherent surface flow or meteorological conditions, such as precipitation and wind displacement of snow [5]. As L-band signals penetrate deeper into snow cover than C-band signals, the temporal stability of the signals are increased which is important for repeat-pass interferometry [18]. On the other hand, as previously

discussed, L-band signals are highly susceptible to ionospheric disturbances, which could degrade the coherence between signals.

3.6 Phase Unwrapping

As the phase in the interferogram is only known modulo 2π, the correct number of phase cycles of the unambiguous phase must be determined to convert the phase to displacement. This is expressed as

$$\psi = \phi + 2\pi \cdot n \tag{3.10}$$

where ψ is the unambiguous phase value, ϕ is the ambiguous phase value and n is the integer number of phase cycles [30]. The process of converting the ambiguous phase values to unambiguous values is referred to as phase unwrapping. In this context, the ambiguous phase values can also be referred to as the wrapped phase, and the unambiguous phase values as the unwrapped phase.

If no discontinuities were present in an interferogram, unwrapping would simply be a matter of selecting a reference point, and integrating the fringes from that point along a path. However, as most interferograms contain discontinuities, the process of unwrapping is not that straight-forward. Discontinuities in the interferogram are usually caused by either phase noise or steep terrain [30]. When discontinuities are present in the interferogram, the point chosen as a reference points affects the resulting unwrapped phase. More sophisticated methods are therefore required for unwrapping interferograms [40].

A common method for performing phase unwrapping is the Statistical-Cost, Network-Flow Algorithm (snaphu), which estimates the most likely unwrapped solution given the data by posing the phase unwrapping as a maximum a posteriori (MAP) estimation problem. As the statistical relationship between the input data (wrapped interferogram) and the solution (unwrapped interferogram) depends on the quantity to be measured (displacement or topography), three different statistical models are built-in in the snaphu software. The models are for topography data, deformation data and smooth generic data. In addition, a mode with no statistical cost function can be selected [41]. For initializing the network solver, a minimum spanning tree (MST) or minimum cost flow (MCF) algorithm can be used. Both initialization options are L1 optimal for solving the phase unwrapping [42]. For large interferograms, snaphu can segment an interferogram into smaller tiles that can be unwrapped individu-

ally to reduce computational costs, before being assembled into a complete, unwrapped interferogram. A more thorough description of snaphu is given in [40].

After successful phase unwrapping is performed, the slant range displacement can be calculated as

$$d_{\text{unw}} = \frac{\lambda}{4\pi}\psi \tag{3.11}$$

d_{unw} is given in units meters. The displacement can then be used to calculate the flow speed as

$$v = \frac{d_{\text{unw}}}{t} \tag{3.12}$$

where t is the temporal baseline, given in units days.

As the phase value measured by interferometry is a difference, and not an absolute value, the corresponding velocities are not absolute values. Instead, the velocities are measured relative to an arbitrary point in the image. By choosing a point with known velocity, such as stable ground, the absolute value of the velocities can be obtained [6].

3.7 Multiple Aperture InSAR

A major drawback of DInSAR for measuring surface displacement is that it can only be used to measure displacement in the slant range direction unless interferometric pairs from ascending and descending passes are available. A method for solving this limitation is the MAI method. In MAI, the synthetic aperture is split in azimuth direction which creates a forward- and backward-looking interferogram with slightly different line of sight (LOS). Taking the difference between the two interferograms results in a phase value that is proportional to the displacement in azimuth [43].

Assuming that the squint angle and beam width are small, the phase can be estimated as

$$\phi_{\text{az}} \approx \frac{2\pi\alpha x}{\lambda} = \frac{2\pi}{l}x \tag{3.13}$$

as the beam width can be approximated as $\alpha \approx \frac{\lambda}{l}$, where l is the length of the antenna and x is the displacement in azimuth direction [43].

The MAI method produces the phase component of the azimuth displacement directly, as the topographic phase and the range and vertical phase contributions are equal in both the forward- and backward-looking interferograms, and therefore cancel each other out. Similarly, the neutral atmospheric contributions can also be assumed to cancel each other out [43]. As well as measuring the azimuth displacement component, MAI can also be used for detecting the presence of azimuth streaks [44].

3.8 Offset Tracking

Offset tracking, also known as image matching or template matching, is an established technique for measuring glacier flow [4], which can either be used to measure the velocity by itself or for estimating the azimuth velocity component for combination with DInSAR measurements [5]. If the coherence between SAR images is sufficiently high, the speckle pattern of the reference and secondary image is correlated. The speckle pattern can then be tracked, which is referred to as speckle tracking. Offset tracking can also be based on intensity tracking, where surface features such as crevasses and rock debris is tracked. This is particularly useful in situations where coherence is low, as this both limits the performance of DInSAR and speckle tracking.

Offset tracking is based on looking for similarities between patches in the images. As with InSAR techniques, the reference and secondary image needs to be coregistered with subpixel accuracy before offset tracking can be applied. After coregistration is performed, the reference and secondary images are divided into smaller patches, with the patch size in the reference image being smaller than or equal to the patch size in the secondary image. For every patch in the reference image, the normalized cross-correlation (NCC) with every patch in the secondary image is calculated [4]. NCC is calculated as

$$\mathrm{NCC}(i,j) = \frac{\sum_{k,l}(r(i+k,j+l)-\mu_r)\,(s(i+k,j+l)-\mu_s)}{\sqrt{\sum_{k,l}(r(i+k,j+l)-\mu_r)^2\ \sum_{k,l}(s(i+k,j+l)-\mu_s)^2}} \tag{3.14}$$

where (i,j) is the position of the search patch in the search image, (k,l) is the position in the reference patch, r is the pixel value from the reference patch, s is the pixel value from the search image, μ_r is the mean value of the reference patch and μ_s is the mean value of the search image.

This results in a 2-D correlation surface, where the correlation peak corresponds to a match. Sub-pixel accuracy can be achieved by fitting a function, such as a Gaussian or a quadratic, to the neighbourhood around the peak [45]. The distance between the patch in the reference image and the peak can then be calculated to estimate the displacement between the images. This method for estimating offsets follows a similar procedure as the CC based coregistration technique.

Calculating NCC requires gliding each patch in the reference image with every patch in the secondary image. This is in essence a convolution operation, and is computationally expensive. The computational costs can be reduced by computing the CC in the frequency domain. Calculating the CC in the frequency domain is more efficient as this only involves cross-multiplying the reference image with the secondary image, which follows from the convolution theorem. CC in the frequency domain is calculated as

$$\mathrm{CC}(i, j) = \mathcal{F}^{-1}\left(F_{ij}(u, v)\, \bar{G}(u, v)\right) \tag{3.15}$$

where $F_{ij}(u, v)$ is the FFT of the patch in the reference image and $G(u, v)$ is the FFT of the search image. The denominator in Eq. 3.14 can be estimated from the mean and variance of the patch in the reference image, which can be used to estimate NCC from the Fourier based CC. This is referred to as Fourier-based NCC [46].

A crucial parameter in offset tracking is the size of the search and reference patches. When determining the size of these patches, a trade off between the spatial resolution and the chance of getting a good match has to be made. Choosing a larger patch size means that more pixels are included when computing the NCC, which increases the chances of getting a good match. The larger patch size also means that there will be fewer displacement measurements, and that each measurement will cover a larger area. This results in a coarser displacement map.

Offset tracking can be a useful alternative to DInSAR for measuring displacement in situations where the displacement of features exceeds the maximum detectable displacement from DInSAR. In cases where strong velocity gradients are present, offset tracking can also perform better than DInSAR as phase unwrapping algorithms may be unable to resolve these gradients [47]. The downside of using offset tracking instead of DInSAR is that offset tracking produces coarser velocity maps with lower accuracy than DInSAR [48] [49]. DInSAR also performs better than offset tracking when measuring the velocity of slow moving glaciers, as well as glaciers containing small scale velocity

gradients [47].

3.9 Displacement

From Eq. 3.4 it can be seen that the interferometric phase is only sensitive to LOS displacement. DInSAR can therefore only be used to measure displacement in the slant range direction. As such, additional measurements in different directions are required to estimate the full 3-D velocity field. If interferometric image pairs from both ascending and descending orbits are available, this can be used to estimate the full 3-D (azimuth, range, vertical) velocity field by generating azimuth and slant range components from both ascending and descending passes [50]. Alternatively, the 3-D velocity field can also be estimated from velocity measurements in two directions, by assuming surface parallel glacier flow. Measurements in both azimuth and slant range can be obtained by combining DInSAR with MAI or the azimuth component from offset tracking [5].

4

Glaciers and Study Area

The necessary theory on glaciers for this study will be presented in this chapter, as well as a description of the study area. A description of the glaciers Kongsvegen and Kronebreen will also be given.

4.1 Glacier Theory

A glacier is a body of ice formed by the compression of snow, as the snow is accumulated over several years. Due to the influence of gravity and the relative softness of the glacier ice, glaciers can flow similar to a slow moving river. This is referred to as plastic deformation. In addition, glaciers that are not frozen to the glacier bed also move by sliding. As water acts as a lubricant between the glacier and its bed, movement by sliding increases during the melting season of a glacier. Generally, the magnitude of the glacier flow speed is highest in the central part of the glacier and decreases towards the the sides of the glacier. The flow speed is also highest at the glacier surface and decreases towards the bed of the glacier because of increased friction though this effect is not as significant for glaciers where sliding is the dominant movement form. Due to the tension in the glacier ice caused by movement, fractures in the ice can form. These fractures are referred to as crevasses [10].

The mass balance of a glacier is the sum of the mass added to the glacier (accumulation) and the mass lost (ablation). The area of a glacier where the

annual mass balance is positive is called the accumulation zone, while the area where the annual mass balance is negative is referred to as the ablation zone. The boundary between these zones is called the equilibrium line, and the altitude of the equilibrium line is referred to as the equilibrium line altitude (ELA). The main source of mass increase for glaciers is precipitation in the form of snow, but avalanches, rime formation and freezing of rain can also be sources of accumulation. Ablation is the collective term for all processes were a glacier loses mass. Surface melting and sublimation are common ablation processes for all glaciers [10]. For tidewater glaciers, which are glaciers that terminate in a body of water, calving and submarine melting are additional major sources of mass loss. These processes are collectively referred to as the frontal ablation rate, as they occur near the front of the glacier [51]. The front, or terminus, of a glacier is the lowest end of the glacier [52]. Normally, glacier fronts retreat and advance periodically, depending on the balance between accumulation and ablation. This is the case for most glaciers in the world [52]. Glaciological processes relevant for tidewater glaciers can be seen in Figure 4.1.

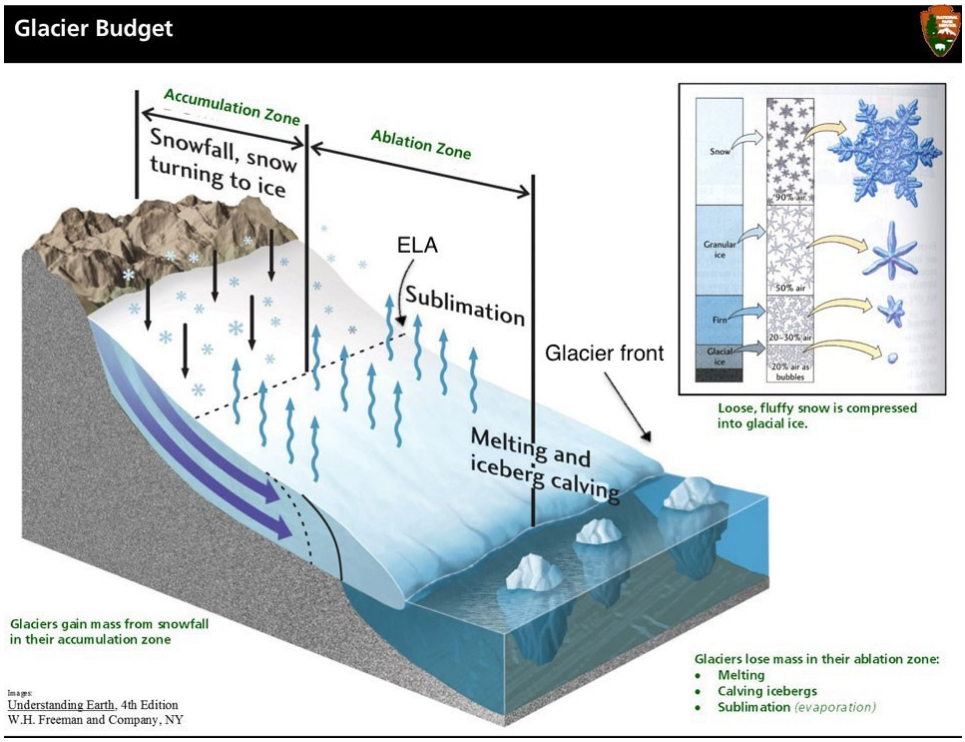

Figure 4.1: Illustration of key processes for a tidewater glaciers. The accumulation and ablation zones are highlighted, as well as processes in each zone. The transformation from snow to glacier ice is also illustrated. Modified from [53].

4.1.1 Surge Type Glaciers

While most glaciers have fronts that retreat and advance periodically with changes in climate, a small portion of the worlds glaciers exhibit what is known as surging behaviour. A surge refers to a sudden, large increase in the velocity of a glacier accompanied by an advance of the glacier front. Glaciers that undergoes surges are known as a surge type glaciers or a surging glaciers. Surge type glaciers have two phases: the quiescent phase, where the glacier is characterized by low flow speeds, and the surge phase, where the flow speed of the glacier is high. During a surge, flow speeds can increase by ten to one hundred times the flow speed during its quiescent phase. The surge phase often lasts for a relatively short period of time, from several months to several years, while the quiescent phase often lasts for a long period of time. In Svalbard, quiescent phases usually last from 50 to 500 years [10]. Leading up to a surging event, Svalbard surge type glaciers have been shown to have a steady increase in flow speed magnitude. This period typically lasts a few years, and is followed by a months long period of large increases in flow speed [48]. Surge type glaciers in Svalbard have previously been studied using both DInSAR and offset tracking [5][8].

4.2 Study Area

Svalbard is an archipelago situated between 74° and 81° North that contains over 2100 glaciers, covering roughly 60% of its land area. A portion of the glaciers in Svalbard are surge type glaciers, with estimates ranging from 13% to over 90% of the total amount of glaciers exhibiting surging behaviour [54]. One such Svalbard surge type glacier is Kongsvegen, which will be the main focus of this study. Flow speed measurements on Kongsvegen's neighbouring glacier, Kronebreen, will also be made for comparisons, as Kronebreen has a high flow speeds, contrasting the slow movement of Kongsvegen. Both glaciers can be seen in Figure 4.2.

4.2.1 Kongsvegen and Kronebreen

Kongsvegen and Kronebreen are two of the four glaciers situated near Ny-Ålesund where mass balance is measured annually by the Norwegian polar institute (NPI) using stakes in the ice to measure accumulation and ablation. The mass balance of Kongsvegen and Kronebreen has been measured since 1987 and 2003 respectively, with both glaciers exhibiting a negative mass balance in these periods [55]. Kongsvegen shared the same front as Kronebreen in the past, but as the front of Kongsvegen has had a large retreat in recent years their fronts

have been separated [56]. A large medial moraine marks the boundary between Kongsvegen and Kronebreen [57]. While Kronebreen has a crevassed surface, particularly near the front, the surface of Kongsvegen is almost featureless. This can be seen in Figure 4.2, where the surface of Kongsvegen is almost completely smooth and covered in snow while the surface of the lower part of Kronebreen is bare ice without any smooth regions.

The Kongsvegen drainage basin is composed of two main tributaries, Kongsvegen and Sidevegen, and has a total area of approximately 102 km^2 [57]. Kongsvegen is currently in its quiescent phase, with its last surge occurring in 1948. Since this surging event, the front of Kongsvegen has retreated over 4 km. The mean surface velocity of Kongsvegen was found to be $2 - 3\ m\ a^{-1}$ for the period 1987-1997 [58]. In the last few years, in-situ measurements have indicated an acceleration of Kongsvegen's flow speed (see Figure 5.3 and Figure 5.4). This will be further discussed in section 5.2.

Kronebreen is a fast flowing tidewater glacier, that actively calves in Kongsfjorden. Schellenbreger et al. (2015) found a peak summer flow speed of $3.2\ m\ d^{-1}$ for Kronebreen in 2013 [56], which is considerably higher than the flow speeds seen on Kongsvegen. The total area of Kronebreen and its drainage baisins, Holtedahlfonna and Infantfonna, was found to be ~390 km^2. A surging event on Kronebreen has never been observed, but one likely occurred around the turn of the 20^{th} century [59]. Kronebreen has previously been successfully studied with both X- and C-band offset tracking [51] [56] and C-band InSAR [60].

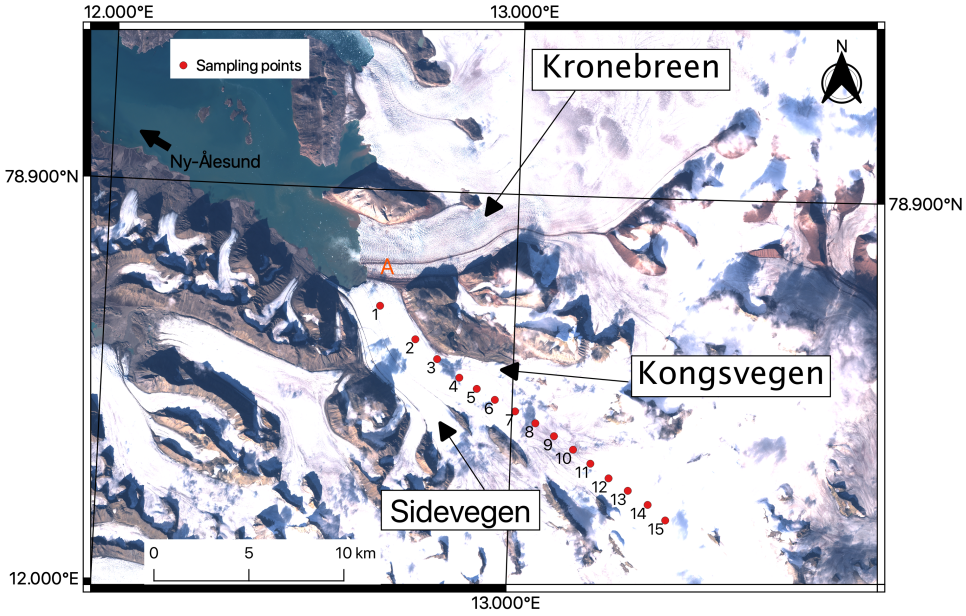

Figure 4.2: Overview of Kongsvegen and the nearby glaciers Kronebreen and Sidevegen seen in a Sentinel-2 image from 24.08.2020. The mass balance stakes for in-situ measurements of annual or seasonal displacements are shown as red dots, and the morraine separating Kongsvegen and Kronebreen is marked with the letter "A". © Copernicus data (2020).

5 Data

This chapter contains descriptions of the data used. The two types of data used in this study are remote sensing data (ALOS-2) and in-situ data (GPS stake measurements). A description of the ALOS-2 data will be given first, followed by a description of the in-situ data.

5.1 ALOS-2

The data used in this study is from the ALOS-2 mission, launched by the Japanese space agency (JAXA) in 2014. ALOS-2 carries the PALSAR-2 sensor, which is an L-band (wavelength: 22.9 cm) SAR system. ALOS-2 is in a sun-synchronous orbit at an altitude $H \approx 628$ km, with a revisit time of 14 days [61]. The specifics for the different imaging modes can be found in Table 5.1. One of the scenes used in this study, converted to GRD format can be seen in Figure 5.1.

The data used in this project were SLC images acquired in 2015, 2018 and 2019. The data acquired in 2015 was High-sensitive mode Full (Quad.) polarimetry data, from right-looking descending passes. The data acquired in 2018 and 2019 was Fine mode dual polarization (HH and HV) data, from right-looking ascending passes. See Figure 5.2 for an overview of the area covered by the different scenes. Data specifics for each image pair can be found in Table 5.2 and Table 5.3. As the acquisition mode of the 2018-2019 data differed from the

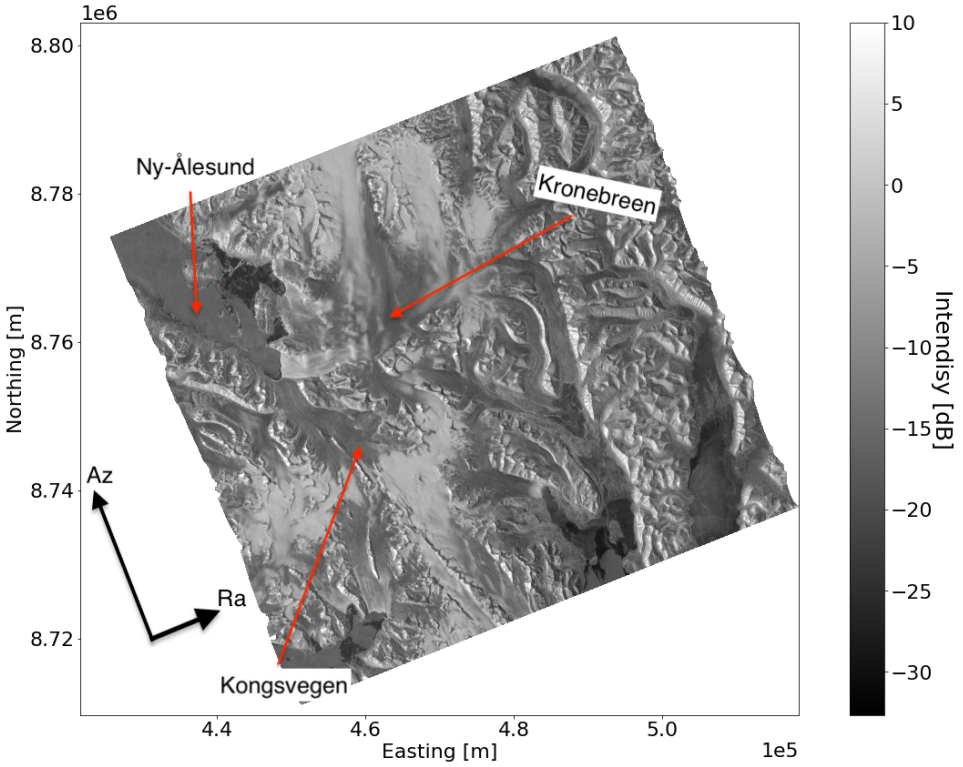

Figure 5.1: Speckle filtered GRD image of the HH channel displayed on dB scale. The scene used was acquired on 11.02.2019 (see Table 5.2). Kongsvegen and Kronebreen are highlighted, as well as Ny-Ålesund for context. The image is displayed in geographical coordinates.

Table 5.1: ALOS-2 PALSAR-2 imaging modes. Single polarization (SP): HH or HV or VV, dual polarization (DP): HH and HV or VV and VH, quad polarization (QP): HH, HV, VH and VV [62]. The imaging modes used in this study are marked with a bold font.

Imaging mode	Mode	Pixel resolution [m]	Spatial coverage [km]	Channels
Spotlight	-	3×1	25×25	SP
Stripmap	Ultrafine	3×3	50×50	SP/DP
	High sensitive	6×6	50×50	SP/DP/**QP**/CP
	Fine	10×10	70×70	SP/**DP**/QP/CP
ScanSAR	Normal	100×100	350×350	SP/DP
	Wide	60×60	490×490	DP/DP

acquisition mode of the 2015 data, the data is separated into two tables. The data was ordered from JAXA in 2021, and therefore has the latest updates for

calibration parameters [63]. Only the HH channel of the data was used, as this channel preserves amplitude better and has a higher SNR than the other channels over glacier ice [47]. All available image pairs as of January 2021, with a time separation of 42 days or less, that could enable InSAR analysis over the two chosen glaciers were included in this analysis.

Table 5.2: 2018-2019 image pairs. B_n denotes the perpendicular baseline. θ is the look angle in the middle of each scene.

	Pair 1	Pair 2	Pair 3	Pair 4
Reference	12.02.2018	30.03.2018	14.06.2018	11.02.2019
Secondary	26.02.2018	13.04.2018	28.06.2018	25.02.2019
Temporal baseline	14 days	14 days	14 days	14 days
Image size	18266×9990	21348×8742	21114×10226	18266×9990
B_n	-132.95 m	-29.33 m	-59.50 m	-70.30 m
θ [°]	36.336	31.446	40.620	36.333
Spatial resolution [m^2]	3.95×7.24	3.38×8.22	3.42×6.59	3.95×7.24

Table 5.3: 2015 image pairs. B_n denotes the perpendicular baseline. θ is the look angle in the middle of each scene.

	Pair 5	Pair 6	Pair 7	Pair 8
Reference	04.01.2015	01.02.2015	15.03.2015	25.10.2015
Secondary	01.02.2015	15.03.2015	26.04.2015	06.12.2015
Temporal baseline	28 days	42 days	42 days	42 days
Image size	23023×6032	23023×6032	23023×6032	23023×6032
B_n	-57.62 m	-337.21 m	-101.28 m	-176.39 m
θ [°]	19.814	19.807	19.804	19.801
Spatial resolution [m^2]	3.14×8.44	3.14×8.44	3.14×8.44	3.14×8.44

5.2 In-situ Data

The in-situ data used in this study is repeated GPS measurements of stakes collected between 2004 and 2020. The stakes are measured annually in August/September. In addition, measurements were made for the summer periods in 2018, 2019 and 2020. The summer period flow speeds are made by measuring the position in April and calculating the difference between this position and the position in August/September. For the years 2018, 2019 and 2020 the ratios between the summer average speeds and the yearly average speeds were

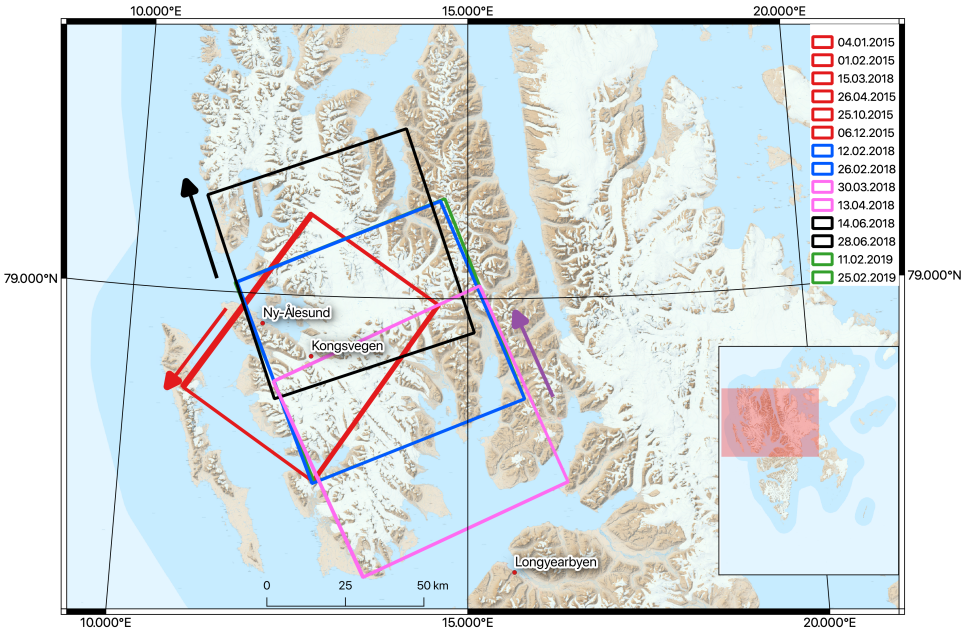

Figure 5.2: Map with the scenes used, and some key locations highlighted for spatial context. The rectangular windows show the areas imaged in each scene. The different swaths are highlighted with different colors. The red arrow indicates the heading for the images highlighted in red, the purple arrow indicates the heading for the images highlighted in blue, green and pink, and the black arrow indicates the heading for the images highlighted in black. The range directions are not included, but as the scenes are acquired from a right looking pass, range direction is to the right of the heading (see Figure 2.1). The background map is created from the "S100 Raster" from NPI [64]. The corresponding image pairs to the dates can be found in Table 5.2 and 5.3.

1.33, 1.57 and 1.21 respectively. This suggests that Kongsvegen has a higher flow speed in the summer than in the winter (see Figure 5.4).

From Figure 5.3, a gradual increase in flow speeds, particularly in the upper part of Kongsvegen, can be seen. The overall shape of the flow speed profile seems consistent, while the magnitude of the flow speed is gradually increasing. This is in line with previous observations of onsets of glacier surges in Svalbard, which suggests that a surging event on Kongsvegen is imminent [48].

5.2.1 Meteorological Data

Meteorological data from the Ny-Ålesund meteorological station is included for discussing the performance of DInSAR and offset tracking on pair 3, which

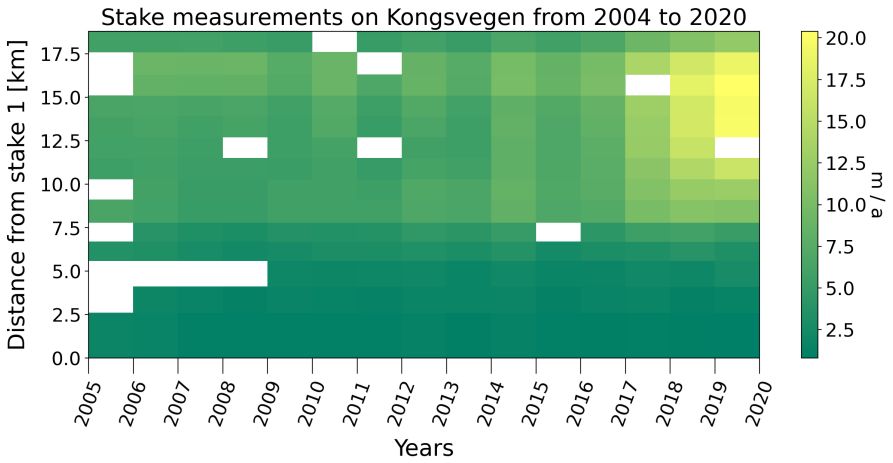

Figure 5.3: Time series of the flow speed profile on Kongsvegen, from in-situ data.

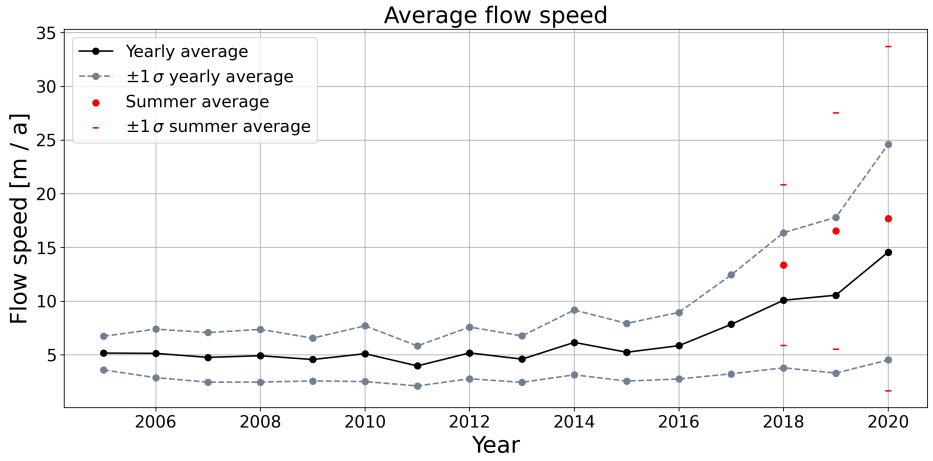

Figure 5.4: Figure showing the flow speeds averaged over the whole flow speed profile $\pm 1\,\sigma$ (standard deviation). The lines show the average flow speed over a whole year, while the dots show the average flow speed over the summer.

will be presented in section 8.2.4. The data included is daily average, minimum and maximum temperatures and precipitation from the period June 15^{th} - June 28^{th}. This can be seen in Figure 5.5.

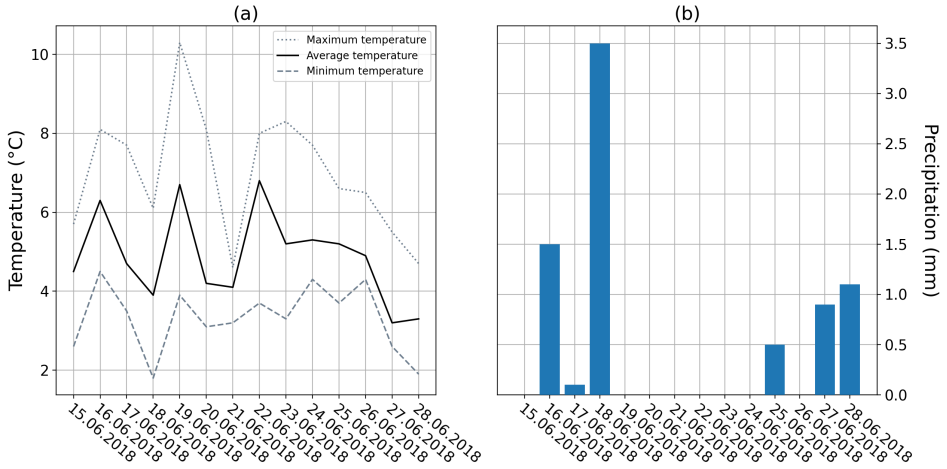

Figure 5.5: Figure showing selected meteorological conditions in Ny-Ålesund for the period June 15th - June 28th. In figure (a) the daily average temperature, as well as daily maximum and minimum temperatures are shown. In figure (b), daily precipitation is shown. Retrieved from seklima.met.no [65].

6 Methods

A thorough description of the different methods used for measuring flow speeds will be given in this chapter, based on the background theory on InSAR, MAI and offset tracking presented in chapter 3. For the DInSAR method (section 6.1) this includes the methods for producing interferograms and transforming these to displacements. In section 6.2 the method for determining the azimuth velocity component using MAI will be presented. Following this, the procedures for performing offset tracking will be presented in section 6.3. Finally, the generation of velocity fields and flow speeds from DInSAR, MAI and offset tracking will be presented in section 6.4 while section 6.5 will present the methods used for evaluating error sources in the measurements obtained.

6.1 DInSAR Workflow

In this section the methods for testing the performance of different algorithms, determining what operations are required and determining optimal parameters for DInSAR are described. The workflow for generating displacement measurements using DInSAR is illustrated in Figure 6.1, where each of the different stages are explained in the subsections below. Unless otherwise is stated, all operations in the DInSAR workflow were performed in SNAP.

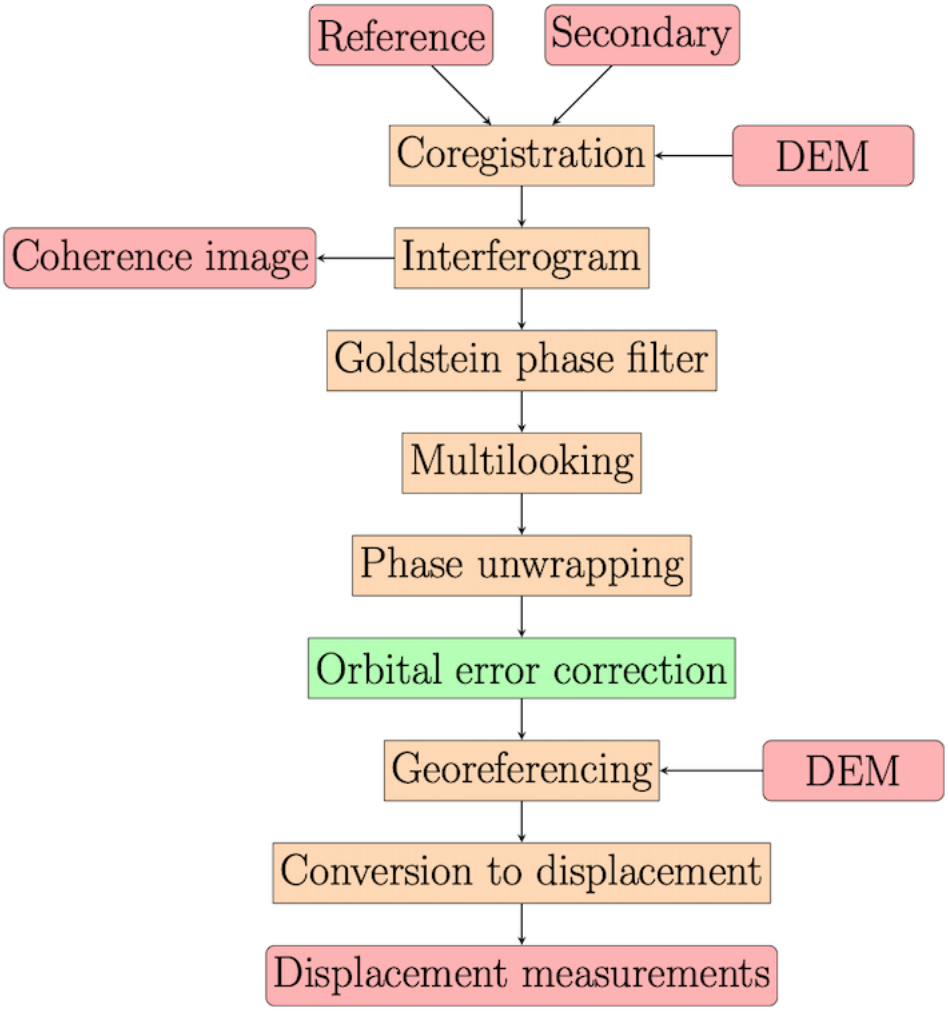

Figure 6.1: Schematic illustration of the interferometric workflow. The red boxes indicate input/output, the orange boxes indicate operations performed in SNAP and the green box indicates operations performed outside of SNAP. The details for the operations are described in section 6.1.

6.1.1 Coregistration

As precise coregistration is crucial for InSAR, several coregistration procedures were tested. The coregistration techniques tested were CC based coregistration, DEM-assisted coregistration and DEM-assisted coregistration with CC, which were the coregistration methods available in SNAP. To compare the performance of each coregistration method, the coherence image is used. An example

of this can be seen in Figure 6.2. For the DEM-assisted coregistration, the ArcticDEM [66] projected in geographic coordinate system WGS 84 (EPSG:4326) was used.

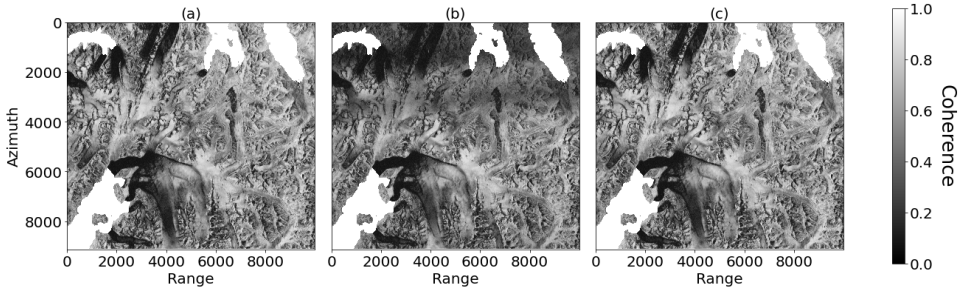

Figure 6.2: Comparison of the coherence for pair 4 (February 2019) from the different coregistration methods used: CC based coregistration (a), DEM-assisted coregistration (b) and DEM-assisted with CC (c). The images are multilooked 2 times in azimuth and displayed in radar coordinates.

Visual inspection of the coherence images produced with the different coregistration methods (Figure 6.2) was used to determine which method produced the best results. If visual inspection was not adequate for choosing one method over another, the average coherence value was used as a criterion [27]. The reason for not using the average coherence value as the primary decision criterion was that isolated regions of low or high coherence could greatly impact the average value, giving an inaccurate representation of the overall coherence in the image.

The average coherence values can be seen in Table 6.1. The DEM does not contain values over open water and these areas were therefore not included in the coherence images from the DEM based coregistration methods. For this reason the open water areas were also removed from the analysis using the CC based method. The open water areas can be seen as the white regions in the coherence images.

Table 6.1: Average coherence ±1 SD for the different coregistration methods tested on pair 4 (February 2019).

Coregistration method	Cross-correlation	DEM-assisted	DEM-assisted with cross-correlation
Average coherence	0.508 ± 0.229	0.411 ± 0.208	0.506 ± 0.227

In Figure 6.2 (b) low coherence regions can be seen in the top part of the coherence image from the DEM-assisted coregistration. This was not present for the other methods. This method was therefore discarded from further

analysis in this thesis. The average coherence from this method was also the lowest out of the three. The coherence images from CC based coregistration and DEM-assisted with CC based coregistration visually looked similar, and the difference in average coherence and SD for the two methods was negligible. The GCP movement was therefore used for determining which coregistration method to proceed with.

To evaluate if the glacier flow between the reference and secondary image had an impact on the coregistration, the movement of the GCPs from the CC based coregistration algorithm was extracted. This can be seen in Figure 6.3. The arrows indicate the GCP movement used to estimate the coefficients in Eq. 3.1. The GCP movement in Figure 6.3 (a) is much larger than in 6.3 (b). This is because the reference and secondary images are already coregistered with the DEM-assisted method in 6.3 (b), and so the CC based coregistration only does minor coregistration adjustments. In 6.3 (b) several of the GCPs have movement close to 0 (white arrows), but there is an almost uniform movement downwards in the top half of the image. Glacier movement does not appear to have a big impact on the coregistration from either method, but least in the DEM-assisted with CC, as almost all the vectors with significant magnitude were pointing straight down. Most of the GCPs in this method also appear to be on stable ground, whereas more appears to be on glaciers from the CC method. The higher average coherence from this method could therefore be a result of overfitting, if some glacier movement was used for coregistration.

For the CC based coregistration, a 128×128 patch size and an oversampling factor of 4 in both azimuth and range was used for the coarse coregistration. For the fine coregistration, a patch size of 32×32 and an oversampling rate of 16 was used, with a coherence threshold of 0.6. For both the coarse and fine coregistration, up to 2000 GCPs were used. The transform function was a first order polynomial, and cubic convolution with six points was used for interpolation. A root mean square (RMS) threshold of 0.05 on the pixel accuracy of the coregistration was used. For the DEM-assisted coregistration, bilinear interpolation was used for resampling the DEM to radar coordinates and for resampling the secondary image to the reference image geometry.

6.1.2 Interferogram Formation

When forming the interferogram, the flat Earth phase contribution from Eq. 3.3 was removed using a 5^{th} degree polynomial, estimated from the orbit state vectors. The topographic phase contribution was not removed as an error was present in the topographic phase removal operator in SNAP [67]. This error remained unsolved for the duration of this project. The implications this had for the results will be discussed in section 8.2.1.

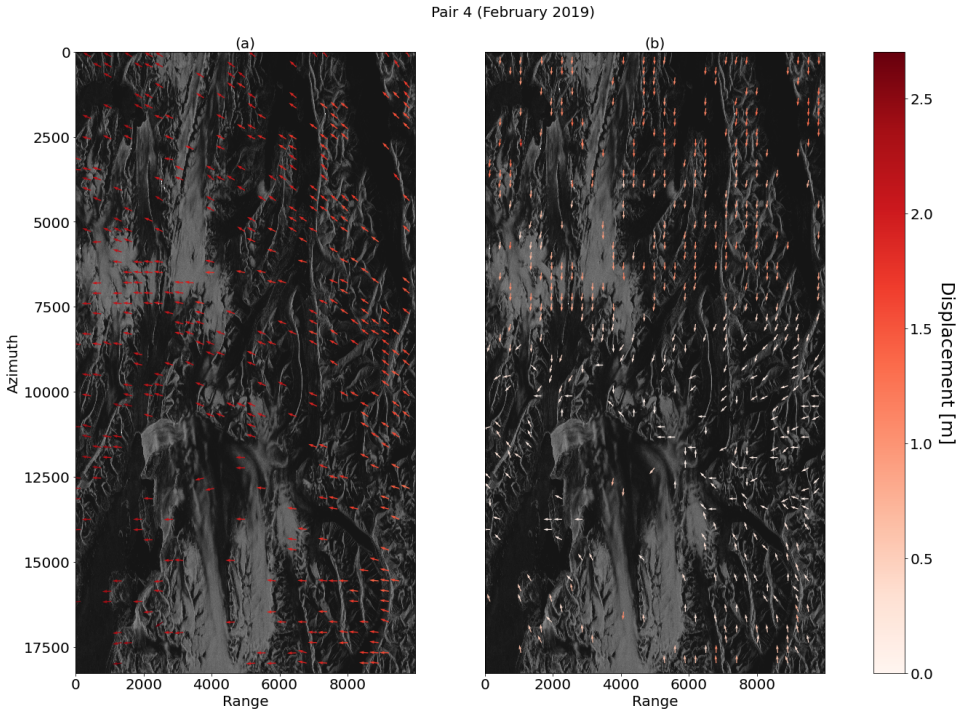

Figure 6.3: GCP movement from normal CC based coregistration (a) and DEM-assisted with CC coregistration (b) on pair 4 (February 2019). The vectors are displayed in unit length, with the colorbar indicating magnitude. The background image is the intensity image of the image acquired on 11.02.2019. The images are displayed in radar coordinates.

The operator used for producing the interferogram in SNAP also has the option of producing the corresponding coherence image. This is useful for an early indication of the quality of the interferogram.

6.1.3 Noise filtering

After the interferograms were produced, the Goldstein phase filter was applied to reduce phase noise. The size of the patches in the filter were 64×64 pixels and the filter parameter, α, was set to 1.

multi-looked was also applied to the interferograms. The wrapped phase of the pairs 1 - 4 data was multi-looked 2×1 times, producing square pixels with a resolution of $7.39 \times 7.39\,\mathrm{m}^2$ for pairs 1 and 4, $7.90 \times 7.90\,\mathrm{m}^2$ for pair 2 and $6.83 \times 6.83\,\mathrm{m}^2$ for pair 3. Pairs 5-8 were multi-looked 3×1 times, producing square pixels with a resolution of $9.43 \times 9.43\,\mathrm{m}^2$. The different multi-looking levels were due to the different image sizes (see Table 5.2 and Table 5.3).

Figure 6.4 shows a comparison between an unfiltered interferogram (Figure 6.4 (a)) and a filtered and multi-looked interferogram (Figure 6.4 (b)) from pair 4.

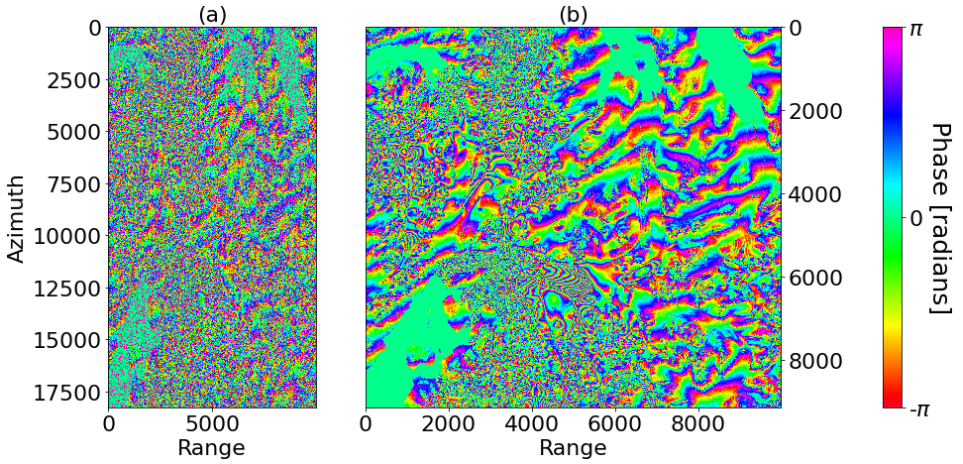

Figure 6.4: Raw (a) and filtered (b) interferogram computed from pair 4 (February 2019). The filtered interferogram was filtered with the Goldstein phase filter and multi-looked 2 times in azimuth. The uniform green regions in (b) are ocean areas, where no coherent phase was obtained. Note the difference in the y-axis of the two images. The images are displayed in radar coordinates.

Atmospheric Effects

No correction for neutral atmospheric effects were made, as SNAP offered no such software packages, and implementing the required methods was deemed to be beyond the scope of this study. Moreover, no designated step for correcting ionospheric azimuth streaking was included either, which affected some of the image pairs.

6.1.4 Phase Unwrapping

The software snaphu was used for performing the phase unwrapping. Several configurations were tested, to optimize the parameter settings in the initialization algorithm. The parameters evaluated were the number of tiles, the statistical cost mode, the tile cost threshold (TCT) and the overlap between adjacent tiles. Snaphu has four different options for the statistical cost mode used: DEFO, TOPO, SMOOTH and NOSTATCOSTS. Only DEFO and SMOOTH were tested, as TOPO is designed for topography measurements while NOSTATCOSTS is intended for initialization purposes [42].

The performance of the unwrapping algorithm for the different configurations was evaluated by visual inspection of the unwrapped interferograms. Ideally, the unwrapped interferogram should be smooth, without the presence of block-like features. The parameters in snaphu were then tuned manually to find the parameters that resulted in the smoothest interferogram. Different amounts of tile overlap were not tested, as this parameter is only used for "stitching" together the tiles after individual unwrapping. The tile overlap should therefore be kept low, as computational costs increase with a larger overlap, and the tile overlap was therefore set to 100. The procedure for determining the remaining parameters is presented in the subsections below.

Number of Tiles

As the tiling process is only performed to reduce computational costs, and the reassembling of adjacent tiles is a challenging operation, the number of tiles should be kept as low as possible to reduce errors in the unwrapped interferogram. The unwrapped interferograms computed from different numbers of tiles can be seen in Figure 6.5, where prominent block-like features or discontinuities are highlighted by black boxes. All tile numbers produced block like features to some degree. This was most prominent in the top right corner of the interferograms, but as this region corresponds to ocean, which contains no coherent phase it can be discarded from the evaluation process. Unwrapping the interferogram with 3×3 tiles introduced a horizontal line which can be seen in the black box in Figure 6.5 (a). For the unwrapped interferograms with 10×10 and 20×20 tiles, a region of discontinuities can be seen in the black boxes in Figure 6.5 (c) and (d). Of the selected number of tiles, 5×5 tiles produced the smoothest interferogram (Figure 6.5 (b)), with block-like features mainly occurring over ocean areas.

Tile Cost Threshold

A comparison between TCT values 0, 500 and 1000 can be seen in Figure 6.6. For TCT 0, discontinuities between the adjacent tiles were introduced, which can most clearly be seen in the yellow/red region, marked by a black rectangle in Figure 6.6 (a). A clear vertical line was introduced in the top half of the unwrapped interferogram computed with TCT 1000. This is marked by the arrow in Figure 6.6 (c). TCT 500 was therefore selected as the TCT value to proceed with, as this produced the least amount of discontinuities.

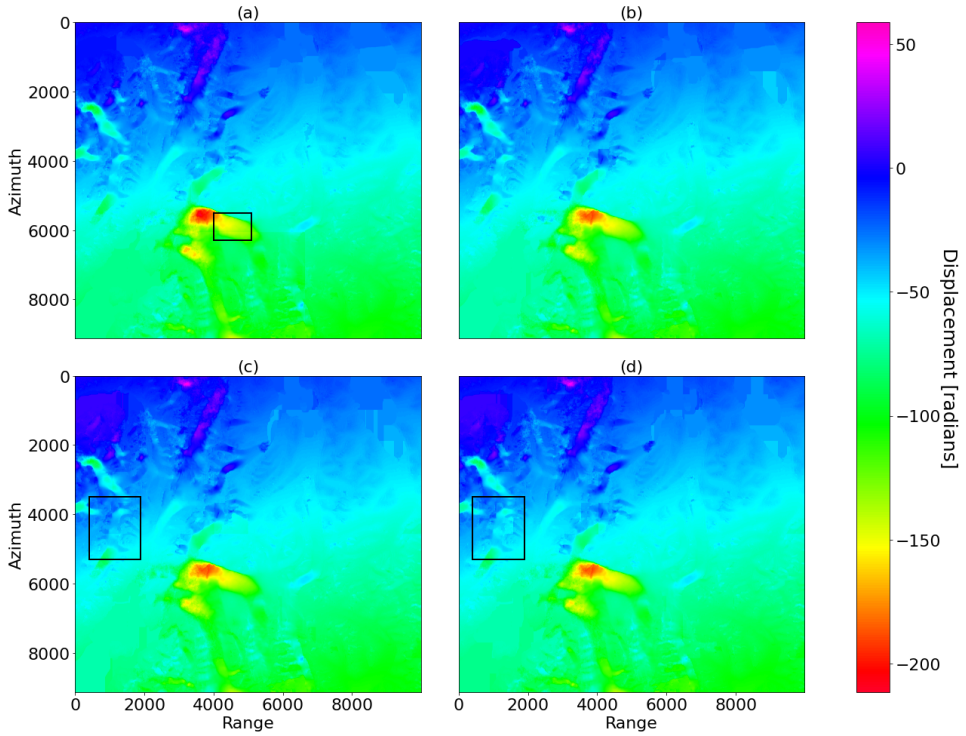

Figure 6.5: Unwrapped interferograms from pair 4 (February 2019) computed with 3×3 tiles (a), 5×5 tiles (b), 10×10 tiles (c) and 20×20 tiles (d). Discontinuities are highlighted by black boxes. The initialization mode was MCF, the statistical cost mode was DEFO and the TCT was 500. The images are displayed in radar coordinates.

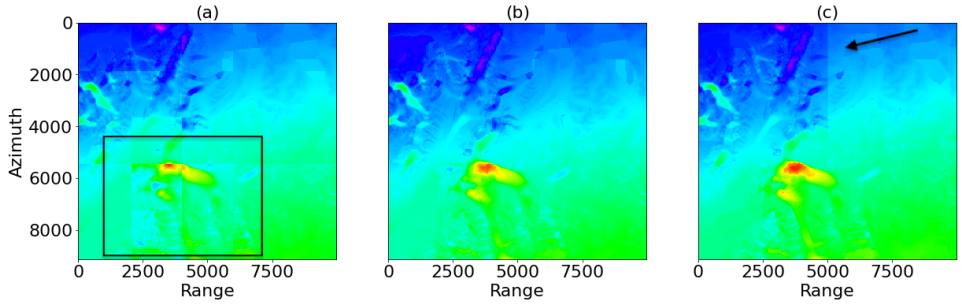

Figure 6.6: Unwrapped interferograms from pair 4 (February 2019) computed with TCT 0 (a), 500 (b) and 1000 (c). Regions of discontinuities are highlighted by a black rectangle (a) and an arrow (c) The number of row and column tiles was 5, the initialization mode was MCF and the statistical cost mode was DEFO. The images are displayed in radar coordinates.

Statistical Cost Mode

The statistical cost modes SMOOTH and DEFO were also compared. The unwrapped interferograms produced with the different statistical cost modes can be seen in Figure 6.7. DEFO produced a generally smooth unwrapped interferogram, with clear areas of displacement (Figure 6.7 (a)). In the unwrapped interferogram computed with SMOOTH, some edges were introduced, marked by arrows in Figure 6.7 (b). Also, the displacement appears visually smoothed out in this interferogram. DEFO mode was therefore selected as the optimal statistical cost mode. As the SMOOTH mode is best suited for smooth interferograms without discontinuities [42], which is not the case in the interferograms produced, this was as expected.

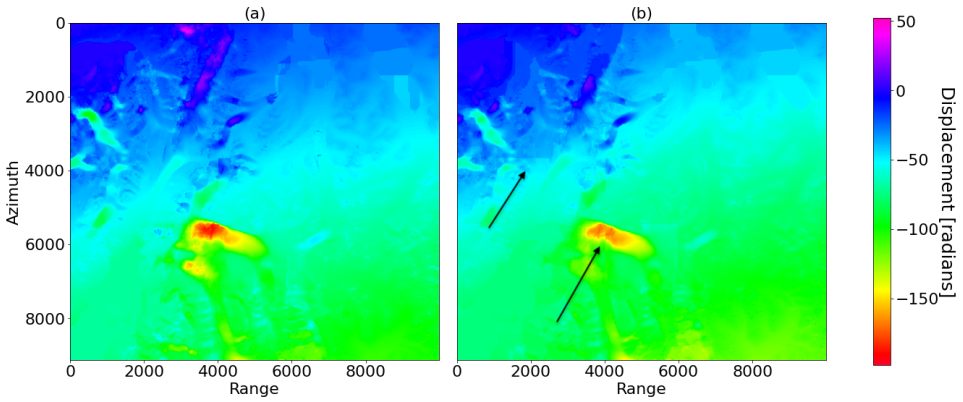

Figure 6.7: The unwrapped interferograms from pair 4 (February 2019) produced with the two different statistical cost modes, DEFO (a) and SMOOTH (b). The number of row and column tiles was 5, the initialization mode was MCF and the TCT was 500. The images are displayed in radar coordinates.

Initialization Mode

Both initialization methods produced similar unwrapped interferograms that were generally smooth, see Figure 6.8. Overall, the results from the two initialization methods were consistent. This can be seen from Figure 6.8 (c), which shows the difference between the unwrapped interferograms computed with each initialization mode. The difference was equal or close to 0 for most of the image, indicating that they produce similar results. The MCF was therefore selected as the initalization mode, as this is the default mode in SNAP.

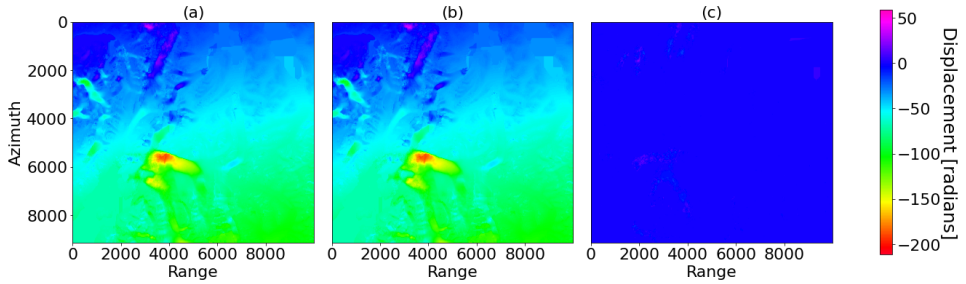

Figure 6.8: Unwrapped interferograms from pair 4 (February 2019) using the two initialization methods, MCF (a) and MST (b), as well as the difference between the two results (c). The number of tiles was 5, the statistical cost mode was DEFO and the TCT was 500. The images are displayed in radar coordinates.

6.1.5 Orbital Error Correction

As the orbit data contained in ALOS-2 data is not precise, but calculated from the raw on board GPS data, orbital fringes were present in the interferograms [68]. Orbital error corrections were therefore applied, as no precise orbit data was available. There is no built-in function for performing orbital error correction in SNAP, so the corrections were applied externally in Python. The methods for computing the phase ramps introduced by the orbital errors described in section 3.4 were implemented in Python based on descriptions from [36, 37, 38]. The corrected unwrapped interferograms were then imported to SNAP for georeferencing. For both techniques, the whole unwrapped phase image was used for estimating the ramp coefficients.

To aid in determining which model produced the best results, the performance over stationary ground, such as mountains, was evaluated. This was done by masking out the glaciers in the deramped images, and assessing to what degree displacement occurred over stable features. The glacier mask used was a subset of the glacier shapefile from the S100 Map Data from NPI [69]. As the mask was geocoded, the deramped images were georeferenced before the mask was applied. The performance over stable ground from both methods is shown in Figure 6.10.

Some regions of significant displacement over stable ground are marked in Figure 6.10. Relatively large displacements over stable ground could be seen in the bottom corners and the top right corner in Figure 6.10 (b) which were not present in Figure 6.10 (a). There were however larger displacements in the centre part of Figure 6.10 (a) than in Figure 6.10 (b), but overall the performance over stable ground appeared better for the linear spatial method than for the quadratic method. The linear spatial method was therefore selected

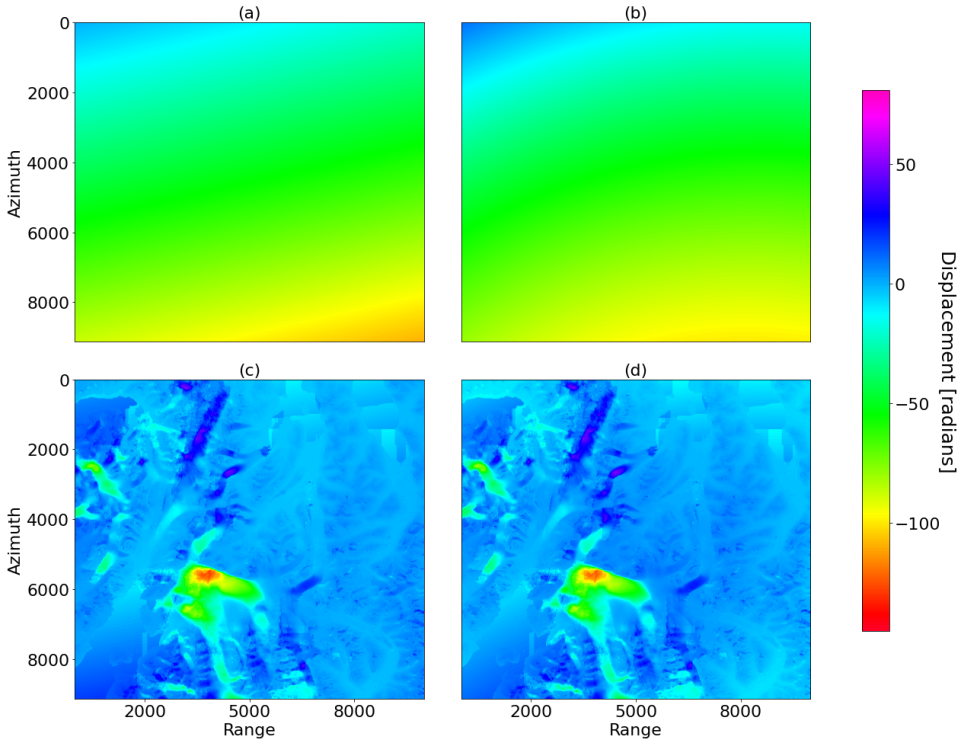

Figure 6.9: The phase ramps (top row) and corresponding corrected unwrapped interferograms (bottom row) using the linear (a, c) and quadratic (b, d) spatial methods on pair 4 (February 2019). The images are displayed in radar coordinates.

as the orbital error removal method for all image pairs. In addition to errors in orbital error correction, some of the displacement over stable ground is also likely attributable to the remaining topographic phase component. This will be discussed further in section 8.2.1.

6.1.6 Georeferencing

After the orbital error correction was applied, the unwrapped phase measurements were georeferenced using the Range Doppler Terrain Correction operator in SNAP. By georeferencing the measurements, they were converted from radar coordinates to geographical coordinates. This was necessary for comparisons between displacement measurements from the different image pairs, as well as for the comparison with the in-situ data. The ArcticDEM [66] projected to WGS 84 (EPSG:4326) was used for the RD terrain correction.

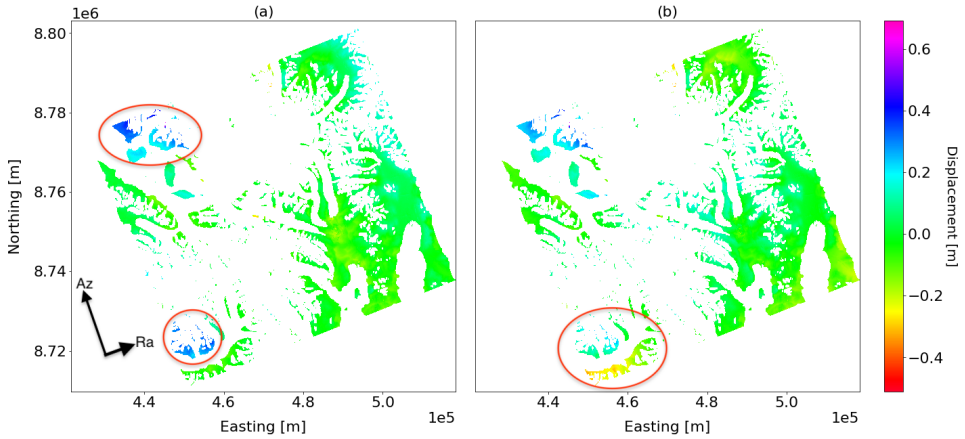

Figure 6.10: Performance over stable ground using the linear spatial method (a) and quadratic spatial method (b) on pair 4 (February 2019). Regions of significant displacement are marked. The images are georeferenced and displayed in geographical coordinates.

6.1.7 Phase to Displacement

The unwrapped, orbit corrected and georeferenced phase was converted from phase values to slant range displacement using Eq. 3.11.

6.2 Multiple Aperture InSAR

For generating the azimuth velocity component the coregistered SLCs were bandsplit in azimuth to create backward- and forward looking interferograms. These were subtracted to create an MAI-interferogram as described in [43][1]. Multi-looking was applied to the MAI interferograms to increase the SNR, with the added drawback of a lower spatial resolution. The SNR of the interferograms was estimated as

$$SNR = \frac{\mu^2}{\sigma^2} \tag{6.1}$$

where μ and σ is the mean and standard deviation over a given region. To get a good estimate of the noise presence, a region assumed to contain a constant phase value was selected.

1. The data processing of SLC pairs to MAI interferograms was carried out by Jelte van Oostveen at the Norwegian Research Centre (NORCE).

MAI measurements were only included for pairs 1, 2 and 4 (see section 7.1). Image pairs 1, 2 and 4 were multi-looked 8×16, 7×18 and 8×16 times respectively, which produced square pixels with resolutions $63.23 \times 63.23\,\mathrm{m}^2$, $60.93 \times 60.93\,\mathrm{m}^2$ and $63.24 \times 63.24\,\mathrm{m}^2$. A different number of looks was applied to pair 2 to achieve a similar spatial resolution as pairs 1 and 4. The multi-looked MAI interferogram from pair 4 can be seen in Figure 6.11 (b). The multi-looked greatly reduced the amount of noise in the interferograms, increasing the SNR from $SNR_{\mathrm{raw}} = 0.010$ in the unfiltered interferogram to $SNR_{\mathrm{ML}} = 0.207$ in the multi-looked interferogram. The island in the region of open water in the bottom left corner of Figure 6.11 (a) and Figure 6.11 (b) was used to calculate the SNR, as the island should be stable ground such that movement within the scene was separated from the SNR estimation. After multi-looking, the azimuth velocity component from MAI was georeferenced.

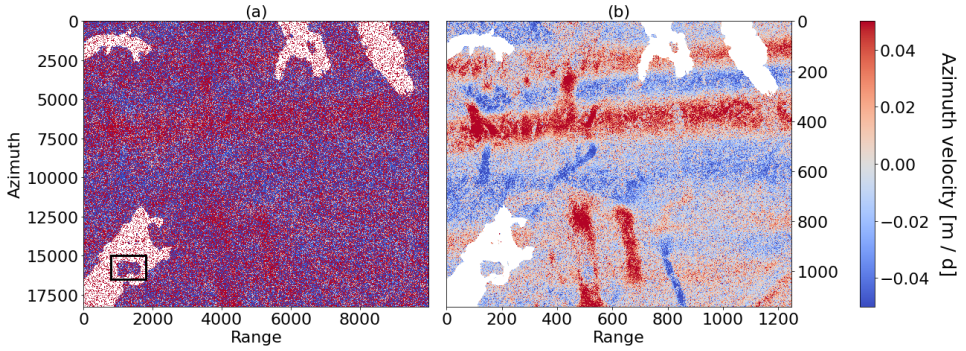

Figure 6.11: Azimuth velocity measurements from the unfiltered MAI interferogram (a) and azimuth velocity measurements multi-looked with 8×16 looks (b) from pair 4 (February 2019). Note the difference in the y-axis of the images. The black rectangle in (a) marks the region used for SNR estimation. Both images are displayed in radar coordinates. Note the difference in the x- and y-axes of the images.

6.3 Offset Tracking

The third method used in this thesis for displacement measurements was offset tracking. Offset tracking was performed on intensity images derived from the coregistered SLC stacks created in the interferogram processing chain (see section 6.1.1).The offset tracking software used in this study, *Icedrift*, was implemented in-house based on an offset tracking method developed at the Alfred Wegener Institute (AWI) [70][71][72]. The software was primarily developed to measure sea ice drift, but can also be used for measuring glacier flow.

Before the offset tracking algorithm was applied to the image pairs, the intensity images were converted to dB scale to enhance surface features. For performing offset tracking, a modified version of *Icedrift* was used, where NCC was used to find the maximum correlation peak.

As the offset tracking was performed on the images in radar coordinates, the resulting velocity measurements had to be georeferenced in order to be compared to the InSAR measurements. Georeferencing was performed using the *Georeferencer* plugin in QGIS, where pixels are assigned coordinates in the unprojected raster, specifying a target coordinate system and using a transformation function to project the raster. The corners of the unprojected rasters and the scene outlines shown in Figure 5.2 were used for assigning coordinates to pixels. The corners were selected as the geographical coordinates were extracted manually, and corners are easily identifiable features. A first degree polynomial was used for projecting the raster. This is in essence the same procedure as the resampling procedure in the CC based coregistration method. The georeferencing was not of high precision, as only four points were used for determining the projection parameters, but as the offset tracking results has a significantly coarser resolution than the original SAR images and the InSAR results, high precision was not required.

After the displacement measurements were made, unrealistic measurements, from here on referred to as outliers, were removed. This was done in two steps: an initial removal of values exceeding a set threshold, followed by a 3×3 median filter. The initial threshold was set significantly higher than any expected glacier movement (9999 pixels), while the median filter was used for removing local discontinuities. If the filtered velocity field still contained some isolated outliers, these were removed manually by a second threshold.

For all pairs, a 50 % overlap between adjacent patches was used. A threshold on the correlation between matches was set to 0, meaning that as long as there was a positive correlation between patches the match was accepted. The patch sizes for each pair had to be determined individually, as factors such as temporal baselines and image resolution had to be taken into consideration for this. A patch size of 50×50 was used on pairs 1, 2 and 4. For these pairs, this patch size was deemed to be a reasonable compromise between spatial resolution and coverage of matches. To achieve approximately square images, the measurements were averaged 2 times in azimuth, which resulted in a spatial resolution of $184.8 \times 184.8\,\mathrm{m}^2$, for pairs 1 and 4, and $180.1 \times 180.1\,\mathrm{m}^2$ for pair 2. For pairs 5-8, a larger patch size of 100×100 was used. The resulting measurements were averaged 4 times in azimuth to produce approximately square pixels, with a spatial resolution of $444.4 \times 444.4\,\mathrm{m}^2$.

As the offset tracking was applied to the images in radar coordinates, the

resulting velocity field could be written as

$$\boldsymbol{V} = V_{\text{OT-sr}}\hat{\boldsymbol{a}}_{Ra} + V_{\text{OT-az}}\hat{\boldsymbol{a}}_{Az} \tag{6.2}$$

where $(\hat{\boldsymbol{a}}_{Ra}, \hat{\boldsymbol{a}}_{Az})$ are the unit vectors in range and azimuth and $(V_{\text{OT-az}}, V_{\text{OT-sr}})$ are the azimuth and slant range components of the velocity field from offset tracking. The flow speeds from offset tracking could then be calculated as

$$V_{\text{OT}} = \sqrt{V_{\text{OT-az}}^2 + V_{\text{OT-sr}}^2} \tag{6.3}$$

Offset tracking was attempted to measure the slant range and azimuth components of the velocity field for the image pairs with low coherence. It was also applied to the image pairs with sufficiently high coherence for DInSAR and MAI measurements, for comparisons between the techniques.

6.4 Generating the Velocity Field

The azimuth - slant range velocity field was generated in two different ways, the combination of DInSAR and MAI, and offset tracking. For the image pairs with sufficiently high coherence, DInSAR was used to measure the slant range component of the velocity field and MAI was used to measure the azimuth component. This combination is from here on referred to as DInSAR - MAI. A 3-D velocity field can be estimated if the slant range and azimuth components from ascending and descending orbits are available. As no coincident ascending and descending acquisitions were available in this project, this method could not be used to measure the 3-D velocity field. The 3-D velocity field can also be estimated using DInSAR - MAI combined with constraints on the assumed flow of the glacier, but this was beyond the scope of this study. The DInSAR measurements are therefore given in slant-range throughout this project.

The combination DInSAR - MAI resulted in a velocity field on the form

$$\boldsymbol{V} = V_{\text{DInSAR}}\hat{\boldsymbol{a}}_{Ra} + V_{\text{MAI}}\hat{\boldsymbol{a}}_{Az} \tag{6.4}$$

where V_{DInSAR} is the slant range velocity from DInSAR and V_{MAI} is the azimuth velocity from MAI. The flow speeds from DInSAR - MAI could then be calculated

as

$$V_{\text{InSAR}} = \sqrt{V_{\text{DInSAR}}^2 + V_{\text{MAI}}^2} \tag{6.5}$$

The flow speeds from DInSAR - MAI and offset tracking were sampled along a line connecting the sampling points corresponding to the stake locations shown in Figure 4.2. The number of sampling points along this line was determined by the spatial resolution of the velocity measurements. For the DInSAR measurements, the line was upsampled into evenly spaced points with 15 m separation. A separation of 15 m was chosen to avoid sampling the same point multiple times. For sampling the MAI and offset tracking measurements, a lower number of sampling points was used. The number of sampling points was determined by the amount of multi-looking performed on the MAI measurements and the patch size of the offset tracking measurements.

6.5 Error Assessment

The displacement of stable features in offset tracking flow speed measurements can be used to provide an indication of errors in the coregistration [8]. This can be achieved by georeferencing the velocity measurements, and masking out non-stable ground in the image. A mask covering stable ground was generated by combining the glacier, water, river plain and ocean shapefiles from NPI [69]. Residual glacier movement due to the coarse georeferencing was removed manually.

As the ability to successfully unwrap an interferogram is closely linked to the coherence image, the coherence was used as an indication of the quality of the InSAR measurements. Similarly, the quality of the matches in offset tracking could be used to get an idea of how reliable the velocity measurements from this technique were.

7 Results

This chapter presents the main results obtained and will be split into three main parts. Section 7.1 contains an evaluation of the produced interferograms and coherence images. This is used to determine which image pairs are suited for DInSAR measurements. In section 7.2, the obtained results from DInSAR, MAI and offset tracking will be presented. Finally, in section 7.3 the measurements from DInSAR - MAI and offset tracking will be compared to the in-situ measurements.

7.1 Evaluation of the Interferograms

Interferograms and coherence images were produced for all 8 image pairs (see Table 5.2 and Table 5.3). The filtered and multi-looked interferograms can be seen in Figure 7.1. High quality interferograms were generated from pairs 1, 2 and 4 (Figure 7.1 (a), (b) and (d)), while the interferograms from pairs 3 and 5-8 were largely dominated by noise (Figure 7.1 (c) and (e)-(h)) although some structure was present in the bottom part of the interferogram from pair 5. The orbital errors can be seen as large scale undulations in the interferograms from pairs 1-4.

Coherent phase structure could be seen in the interferograms from pairs 1, 2 and 4 (Figure 7.1 (a, b, d)), indicating that unwrapping could successfully be performed on these pairs. A band of phase decorrelation could be seen in the

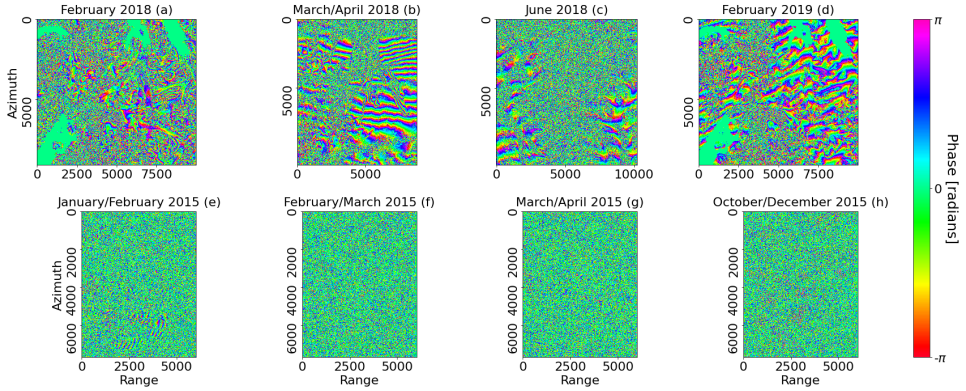

Figure 7.1: Multi-looked and filtered interferograms from pair 1 (a), pair 2 (b), pair 3 (c), pair 4 (d), pair 5 (e), pair 6 (f), pair 7 (g) and pair 8 (h). All images are displayed in radar coordinates. Note the difference in shape for the images.

bottom part of Figure 7.1 (b), which was caused by severe azimuth streaking. Some phase structure could also be seen in parts of the interferogram from pair 3 (Figure 7.1 (c)), but these regions correspond mostly to stable ground and were therefore not useful for displacement measurements.

The coherence image gives a good indication of the quality of an interferogram, and can therefore be used in combination with the interferograms to determine if performing phase unwrapping is feasible. Moreover, the coherence image is also useful for detecting the presence of azimuth streaking, which can be a major source of error in L-band InSAR (see section 3.2.1). The coherence images from all the image pairs can be seen in Figure 7.2.

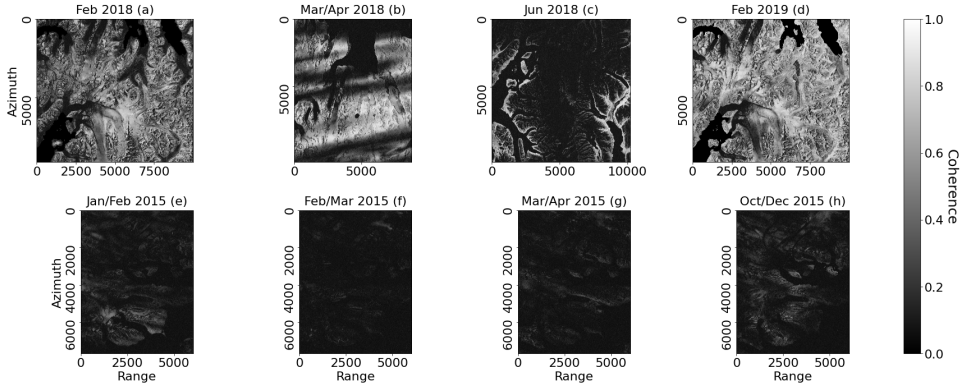

Figure 7.2: Coherence images from pair 1 (a), pair 2 (b), pair 3 (c), pair 4 (d), pair 5 (e), pair 6 (f), pair 7 (g) and pair 8 (h). All images are multi-looked, and displayed in radar coordinates. Note the difference in shape between the images.

Image pairs 1, 2 and 4 had generally high coherence, while the coherence of the remaining image pairs was low overall. Unsurprisingly, the interferograms corresponding to the low coherence images were dominated by noise. Based on the quality of the interferograms and the coherence images, only pairs 1, 2 and 4 were suitable for phase unwrapping and further interferometric analysis.

Azimuth streaking was observed in the coherence images for pair 1, pair 2 and pair 4. The streaking was most severe in pair 2, moderate in pair 4 and almost negligible in pair 1. Unfortunately, the streaking in the bottom part of the coherence image from pair 2 (Figure 7.2 (b)) covers the upper part of Kongsvegen. This limited the usefulness of this pair for measuring flow speeds on Kongsvegen using InSAR. As the overall coherence for pairs 5-8 was significantly lower than for pairs 1, 2 and 4, detecting azimuth streaking by visual inspection of the coherence images from these pairs was more challenging. Azimuth streaking appears to be present in pair 5, while pair 8 appears more or less unaffected (Figure 7.2 (e) and (h)). For pairs 6 and 7 the coherence was too low for visual detection of azimuth streaking. The effects of the azimuth streaking will be discussed in section 8.2.2.

7.2 Velocity Fields

For the pairs with a sufficiently high coherence (see Figure 7.2), the combination DInSAR - MAI was used for generating the slant range and azimuth components of the velocity field. As the coherence was too low for DInSAR measurements on pairs 5-8, offset tracking was attempted for measuring flow speeds from these pairs. Offset tracking was also applied to the pairs where the DInSAR - MAI combination was used, for comparison purposes.

7.2.1 DInSAR Measurements

For pairs 1, 2 and 4, the coherence, and therefore also the phase stability, was sufficiently high for successful phase unwrapping. DInSAR could thus be used to estimate the slant range velocity component from these pairs. The slant range velocity component estimated from pair 4 using DInSAR can be seen in Figure 7.3. Negative slant range velocities for these pairs corresponds to a South-West flow direction (see Figure 5.2). Non-glacier regions in this scene were removed using the glacier mask from section 6.1.5.

Pairs 1 and 4 were acquired from approximately the same viewing geometry (see Figure 5.2), with one year separation. The slant range velocity measurements from these pairs could therefore be directly compared, without requiring

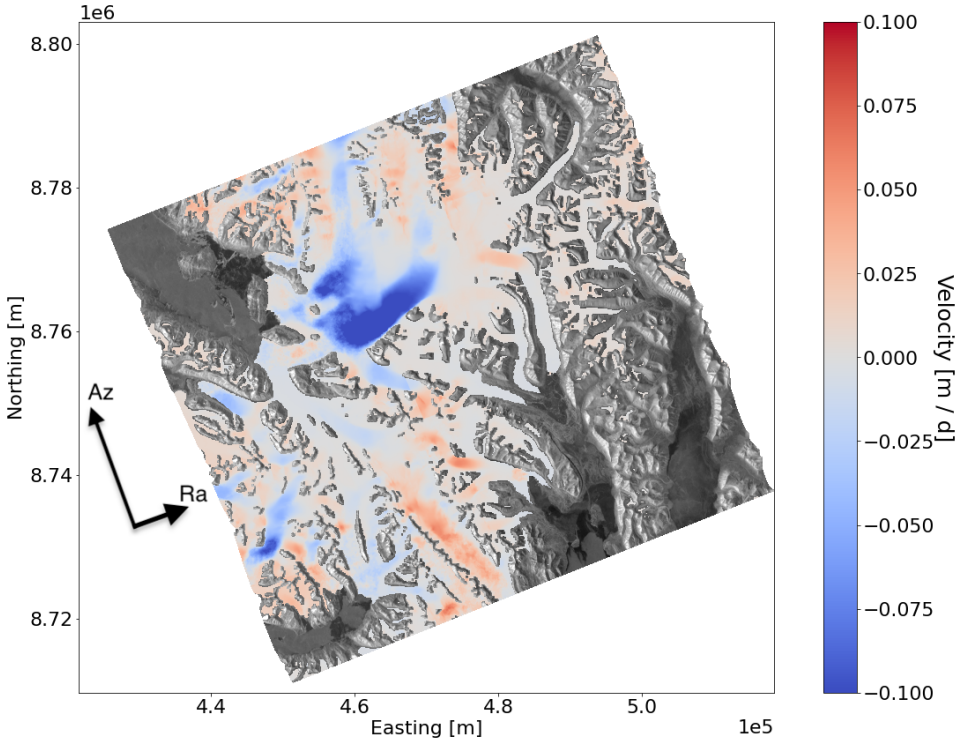

Figure 7.3: Multi-looked and georeferenced slant range velocity measurement over glaciers from pair 4 (February 2019) using DInSAR, overlayed an ALOS-2 GRD from 11.02.2019 displayed on dB scale. Displayed in geographical coordinates.

knowledge of the azimuth component. The slant range velocity profile, as well as the corresponding coherence values can be seen in Figure 7.4. An increase in the magnitude of the velocity measurements between pair 1 and pair 4 can be seen, while the shape of the profiles are similar. This is in agreement with the in-situ measurements, which show an increase in flow speed magnitude between 2018 and 2019, while the shape flow speed profile remained relatively consistent (see Figure 5.3).

As previously mentioned, the coherence for pair 4 was higher than for pair 1. This can also be seen in Figure 7.4. The velocities from the two pairs differ significantly in the lower part of Kongsvegen, as the measurements from pair 1 are heavily influenced by noise in this region. The coherence values from pair 1 were also low in this region, which indicates that the large difference between the velocities from pair 1 and pair 4 were a result of phase decorrelation.

DInSAR was also applied to pair 2. As this pair had regions with severe azimuth streaking (Figure 6.2 (b)) and subsequently low coherence, there was some

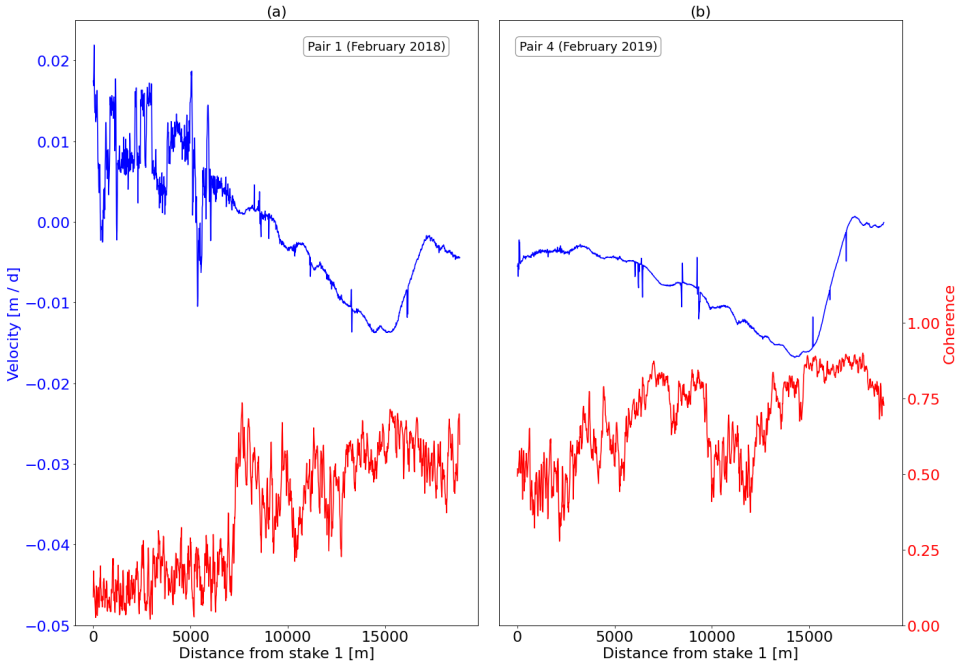

Figure 7.4: Slant range velocity profiles (blue lines) and coherence values (red lines) plotted against distance from stake 1 for pair 1 (a) and pair 4 (b).

uncertainty regarding to what degree the interferogram could be successfully unwrapped. The regions unaffected by ionospheric disturbances were however unwrapped successfully. A slant range velocity profile could then be extracted for pair 2, which can be seen in Figure 7.5. As a result of azimuth streaking, there were regions of low coherence in this profile. The velocity measurements from these regions were heavily influenced by noise ($\sim 5000-12500$ m from stake1). The influence and effects of the ionospheric disturbances on the InSAR measurements from pair 2 will be further discussed in 8.2.4.

Pair 2 partially overlapped pairs 1 and 4 and was acquired with similar viewing geometry (see Figure 5.2). The DInSAR velocity measurements from pair 2 could therefore be compared to the measurements from these pairs. This can be seen in Figure 7.6 (a). In this figure, the velocity measurements corresponding to coherence values below 0.4 were removed from pair 2. The coherence threshold of 0.4 was set empirically from Figure 7.5. These measurements were removed to improve the visual comparison between the velocity profiles, as they were heavily influenced by noise. The glacier bed topography, sampled at 275 m intervals along the sampling profile is shown in Figure 7.6 (b). This is included for evaluating the shape of the DInSAR profiles, which will be further discussed in section 8.1.1.

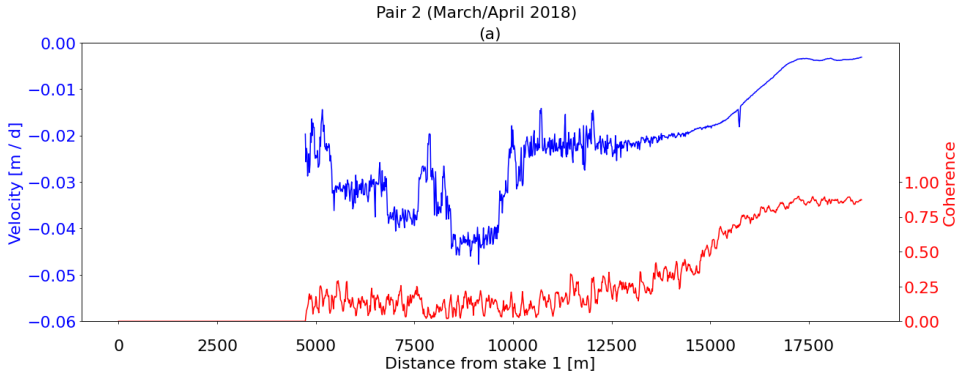

Figure 7.5: Slant range velocity profile (blue line) and coherence values (red line) plotted against distance from stake 1 for pair 2 (a).

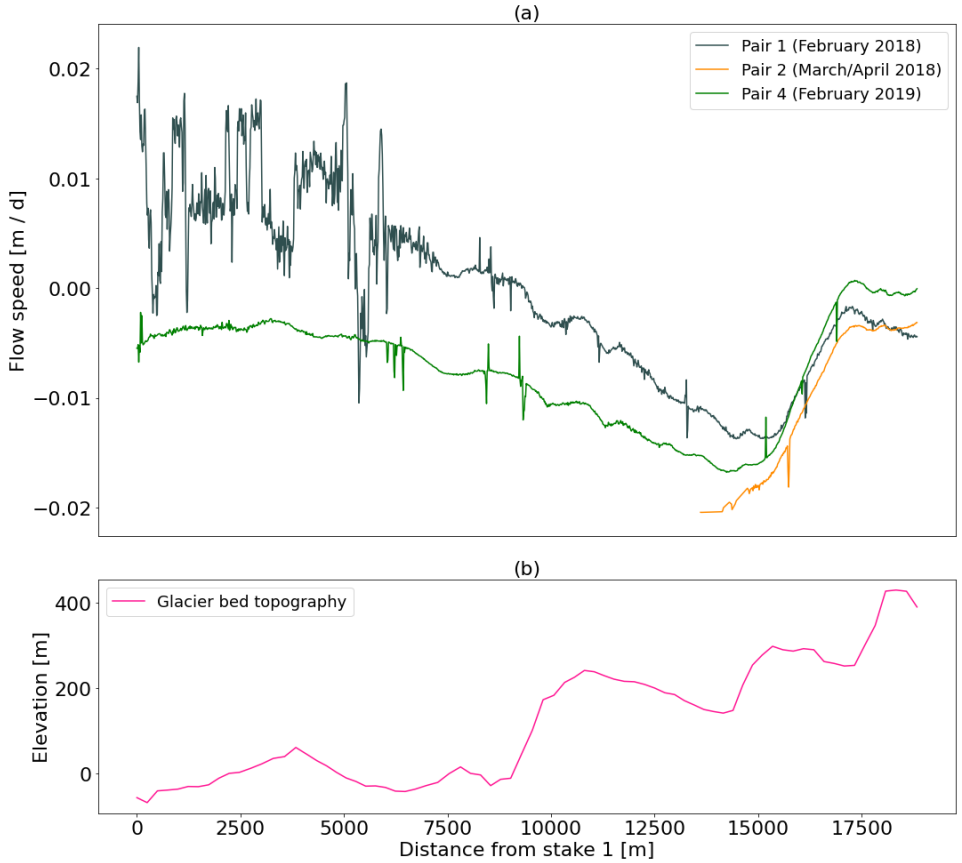

Figure 7.6: Slant range velocity profiles from pairs 1 (February 2018), 2 (March/April 2018) and 4 (February 2019) measured with DInSAR (a) and glacier bed topography (b). The velocity measurements corresponding to coherence values below 0.4 were removed from pair 2 for visualization purposes.

The slant range velocity profiles measured with DInSAR and the corresponding coherence values from pair 5 can be seen in Figure 7.7. Note the difference in range direction for pair 5 compared to pairs 1, 2 and 4 (see Figure 5.2). The profile was heavily influenced by noise, and showed an almost linear increase in velocity towards the upper section of Kongsvegen. There were also large discontinuities in the profile. As the corresponding coherence was also low, below ~ 0.3 for most of the profile, the poor quality of these measurements were likely a result of phase decorrelation. The results where similar for pairs 6 -8, but as the coherence was even lower for these pairs, a higher degree of noise was present. The DInSAR profiles from these pairs were therefore not included. Due to the large influence of noise on the DInSAR measurements from pairs 5-8, these were not included in any further interferometric analysis. Similarly, no reasonable measurements could be made with DInSAR from pair 3. This was as expected from the evaluation of coherence images and wrapped interferograms in section 7.1.

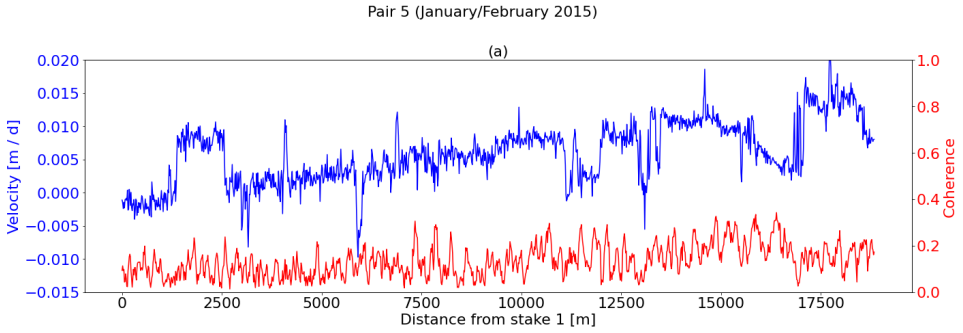

Figure 7.7: Slant range velocity profile (blue line) and coherence (red line) plotted against distance from stake 1 for pair 5 (January/February 2015).

MAI Measurements

As the main motivation behind using MAI was to construct the full velocity field in combination with DInSAR, the MAI results were only included for the pairs where satisfactory DInSAR measurements were obtained. MAI measurements were therefore only included for pairs 1, 2 and 4.

Flow speed maps estimated from the DInSAR - MAI combination can be seen in Figure 7.8. The effects of azimuth streaking on pairs 2 and 4 can be seen clearly in Figure 7.8 (b) and (c), as the blue/green banding. In contrast, only a few weak bands could be seen in Figure 7.8 (a), as pair 1 was affected to a much smaller degree by ionospheric interactions than pairs 2 and 4.

The velocity field from pairs 1, 2 and 4 over a subset covering Kongsvegen can

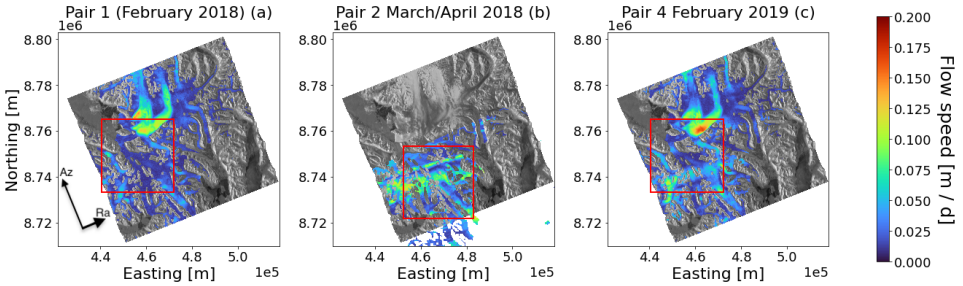

Figure 7.8: Flow speeds estimated from the combination DInSAR - MAI for pairs 1 (a), 2 (b) and 4 (c) overlayed an ALOS-2 GRD from 11.02.2019. Both the DInSAR and MAI velocities were multi-looked 8×16 times for pairs 1 and 4, and 7×18 times for pair 2. Subsets covering Kongsvegen are marked by red squares. The images are georeferenced and displayed in geographical coordinates.

be seen in Figure 7.9. A subset over Kongsvegen was selected for display to enhance the visual appearance of the velocity vectors over this region. The direction of the velocity vectors was dominated by the presence of azimuth streaking in the velocity measurements from pairs 2 and 4 (Figure 7.9 (b) and (c)). A smooth and uniform velocity field was obtained over the upper section of Kronebreen from pairs 1 and 4 (Figure 7.9 (a) and (c)). As the flow speeds on this glacier was higher compared to the flow speeds on Kongsvegen, the vectors from Kongsvegen were difficult to interpret visually, but they seem to follow the expected flow direction towards Kongsfjorden, particularly in the upper part. Due to the heavy azimuth streaking present, no useful information could be obtained from the velocity vectors in pair 2 (Figure 7.9 (b)).

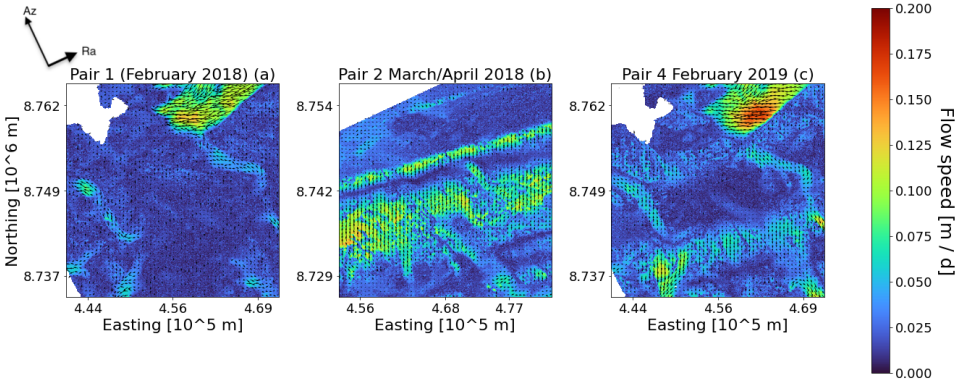

Figure 7.9: Velocity fields produced from the combination DInSAR - MAI over subsets covering Kongsvegen (see Figure 7.8) from image pairs 1 (a), 2 (b) and 4 (c). The images are georeferenced and georeferenced. Note that the vectors are displayed in an azimuth - slant range coordinate system.

7.2.2 Offset Tracking Measurements

Offset tracking was attempted on all pairs. For pairs 1, 2 and 4, InSAR measurements were successfully made, but offset tracking was still performed on these pairs for comparisons. As InSAR measurements were not possible on pairs 3 and 5-8, offset tracking was attempted for measuring velocities from these pairs.

As expected, reasonable results could also be achieved with offset tracking on the pairs with sufficiently high coherence for InSAR applications. The flow speed image derived from offset tracking applied to pair 4 can be seen in Figure 7.10. Vectors showing the glacier velocities in the scene were not included, as the large displacements from fast flowing glaciers like Kronebreen and erroneous matches made visual interpretation of the vectors difficult. For an indication of the direction of flow on some of the glaciers in the scene, see Figure 7.9.

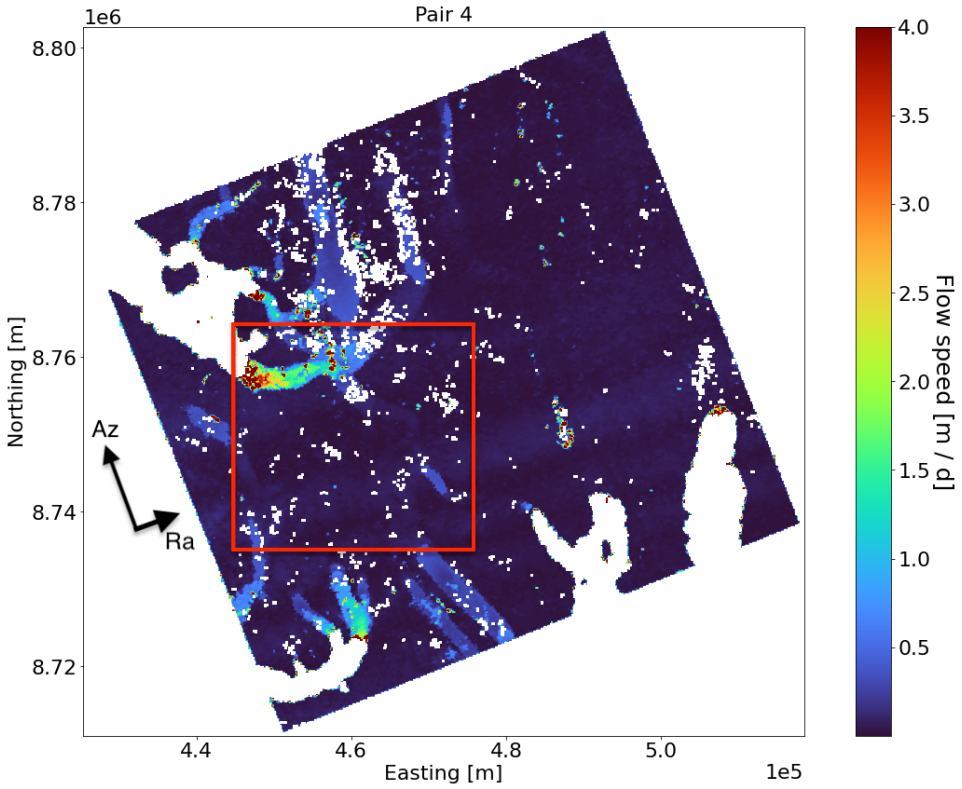

Figure 7.10: Georeferenced flow speed map produced from offset tracking on pair 4 (February 2019). A region covering Kongsvegen and the lower part of Kronebreen is marked by a red rectangle. The image is displayed in geographical coordinates. Note the difference in the flow speed range compared to the DInSAR - MAI measurements.

A comparison between the flow speed measurements from DInSAR - MAI and offset tracking can be seen in Figure 7.11. The DInSAR - MAI measurements were filtered with a 5×5 moving average filter to reduce noise. As the DInSAR - MAI measurements had significantly higher spatial resolution than the offset tracking measurements, the number of sampling points for the DInSAR - MAI data was also higher. Erroneous measurements were removed from the offset tracking profiles by setting a threshold of 2 times the maximum flow speed value from DInSAR - MAI. This threshold was set empirically based on the assumption that the DInSAR - MAI measurements were reasonable and should not deviate from the actual in-situ measured flow speeds by more than a factor 2. The root mean square error (RMSE) between the DInSAR - MAI and the filtered offset tracking flow speed measurements was then calculated. These scores can be found in Table 7.1. The RMSE was somewhat high for all pairs given the expected flow speed range on Kongsvegen $\left(\sim 10^{-2} \right)$, and was almost twice as high for pair 2 as for pairs 1 and 4. The relatively high RMSE values were likely caused by the large spikes present in the offset tracking profiles, as the methods can be seen to be in good agreement for some parts of the flow speed profiles. Good agreement between the DInSAR - MAI and offset tracking could especially be seen in the upper parts of Kongsvegen, apart from the regions affected by azimuth streaking (see Figure 7.11 (b) and (c)). This was also a region with high quality matches for all three pairs (see Figure 7.14).

Table 7.1: RMSE between the offset tracking and DInSAR - MAI measurements for pairs 1, 2 and 4.

Image pair	RMSE [m d^{-1}]
Pair 1	0.028
Pair 2	0.058
Pair 4	0.033

Offset tracking was also attempted on pair 3, as the coherence for this pair was too low for InSAR measurements to be made. However, the temporal decorrelation limited the performance of offset tracking as well, and no reasonable measurements on Kongsvegen could therefore be made from pair 3 with either technique. The flow speed image for pair 3, measured with patch size 40×40, was largely dominated by noise, which can be seen in Figure 7.12 (a). Low quality of matches was also found for most of the scene (Figure 7.12 (b)), except over stable ground. No flow speed measurements on Kongsvegen could therefore be made on pair 3. Reliable measurements could however be made in the lower part of Kronebreen, likely due to the presence of distinct surface features in the form of crevasses. The quality of matches was also somewhat higher in this region.

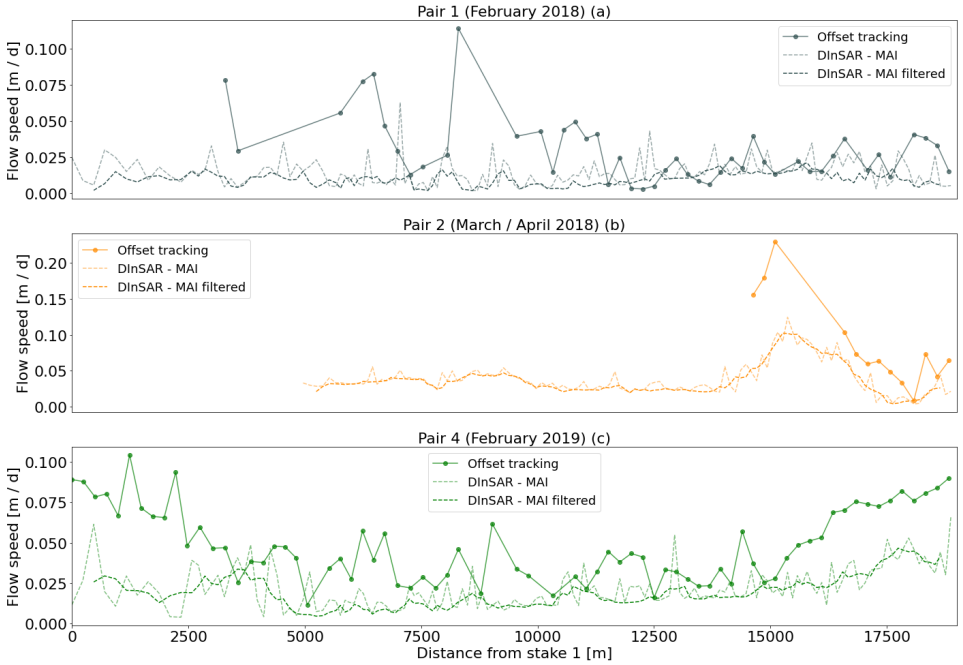

Figure 7.11: Flow speed profiles estimated with DInSAR - MAI and offset tracking for pair 1 (a), pair 2 (b) and pair 4 (c). The flow speed profiles from DInSAR - MAI were smoothed with a 5×5 moving average filter. Note the difference in the range of the y-axis for the figures.

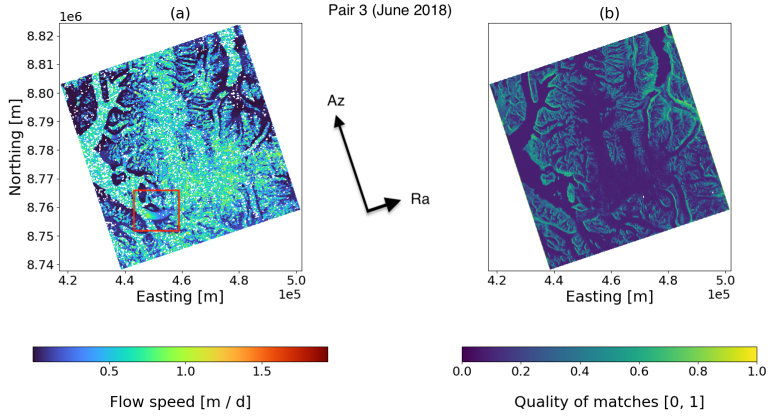

Figure 7.12: Flow speeds (a) and the corresponding quality of matches (b) from pair 3. Kronebreen is marked by a red rectangle. The images are displayed in geographical coordinates.

The flow speed images from offset tracking on pairs 5-8 can be seen in Fig-

ure 7.13. From this it can be seen that reasonable results were not achieved on Kongsvegen from this method either, as the flow speeds on Kongsvegen were several orders of magnitude larger than what was expected. As such, no flow speed profile or average flow speeds was extracted from offset tracking on pairs 5-8. Reasonable measurements could however be made on faster flowing glaciers in the area, such as Kronebreen and Aavatsmarkbreen which are highlighted in Figure 7.13 (a). This will be discussed further in section 8.1.2.

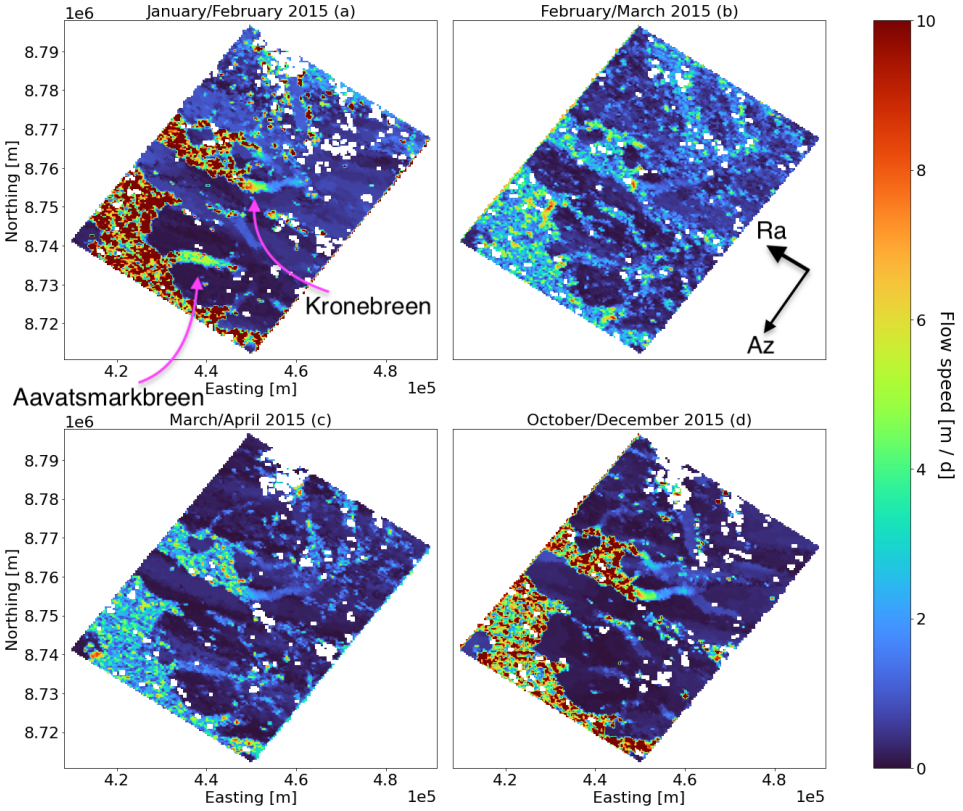

Figure 7.13: Flow speed measurements from offset tracking on pairs 5-8 (a-d), with the glaciers Kronebreen and Aavatsmarkbreen highlighted. The measurements were made with patch size 100 × 100 and averaged 3 times in azimuth. Displayed in geographical coordinates.

The quality of the matches for pairs 1, 2, 4 and 5-8 along the sampling profile is shown in Figure 7.14. For pairs 1, 2 and 4, the quality of the matches was relatively high ($\sim 0.3 - 0.7$) for large parts of the profile, particularly in the upper section of Kongsvegen. A region of low quality matches was however found around 6000 – 13000 m from stake 1 (the gray region in Figure 7.14). For pairs 5-8, the quality of the matches was close to 0 for most of the profile, except for the uppermost section of Kongsvegen where somewhat higher qualities

(~ 0.1 – 0.3) were found. This, in combination with the large magnitudes of the flow speeds on Kongsvegen from pairs 5-8 suggests that errors in matching likely occured.

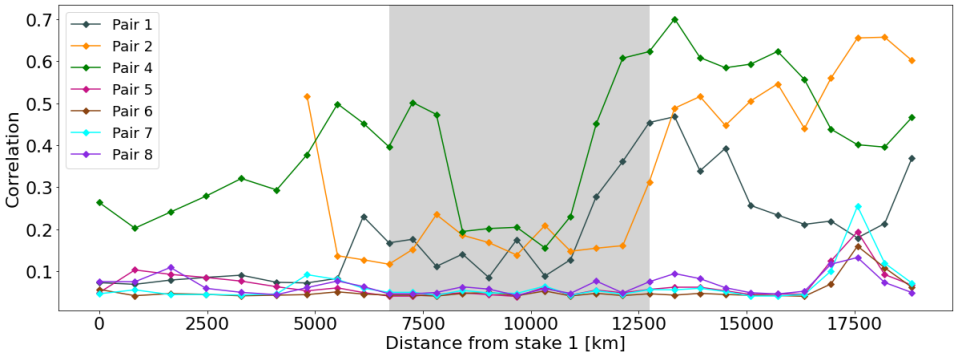

Figure 7.14: The quality of the matches for all pairs except pair 3 along the sampling profile, sampled at 1 km intervals. The gray section marks a region of low quality matches for most pairs.

Estimation of Coregistration Accuracy Using Offset Tracking

The displacement over stable ground from pair 4 can be seen in Figure 7.15. From this figure it can be seen that the displacement over stable ground was overall low (i.e. below ~ 0.2 pixels), indicating a relatively precise coregistration. There were however regions of large displacement present, for instance the region marked in Figure 7.15. Most of these regions were either regions close to the ocean, or smaller glacier valleys. These displacements could therefore be a result of imprecise masking. The average displacement over stable ground was 0.874 ± 2.32 pixels, but these values were skewed by the presence of the large displacements which were not representative of the general displacement over stable ground. This is further supported by the large SD. The median could therefore give a more accurate representation of the displacement over stable ground. The median displacement was 0.071 pixels, which was an order of magnitude less than the average displacement. The median displacement over stable ground was less than what was suggested as a criterion for precise coregistration by Zhou et al. (2009) [17], while the average exceeded this value. As the median was deemed to be a more representative measure, the coregistration was considered sufficiently accurate.

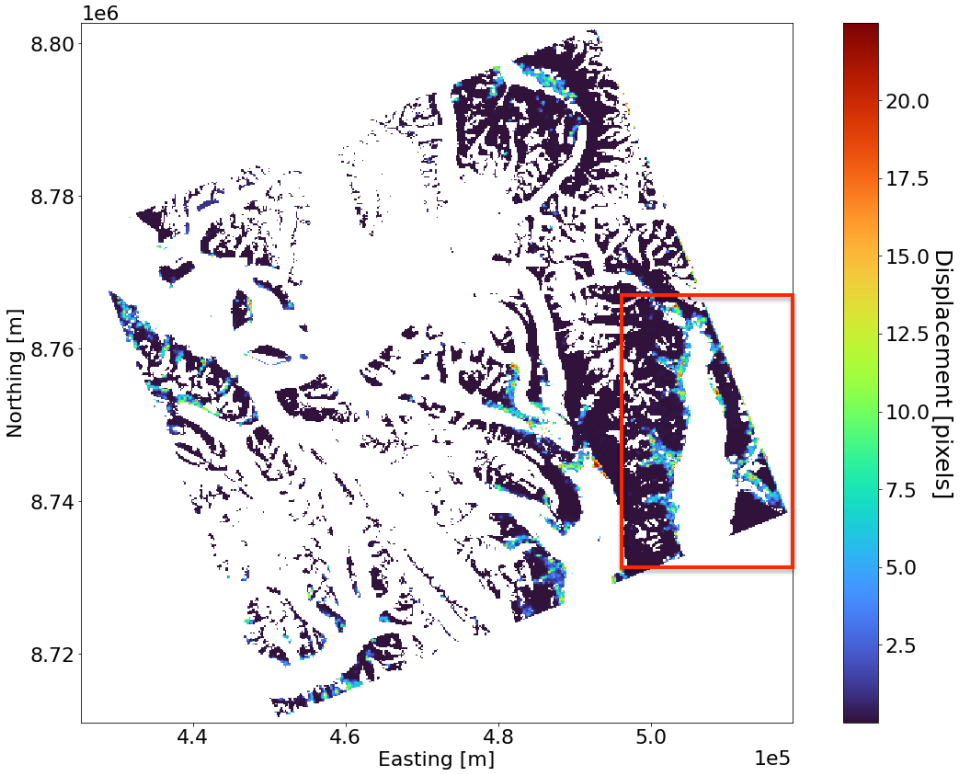

Figure 7.15: Displacement over stable ground from offset tracking on pair 4. The red box indicates a region of large displacement. The image is georeferenced and displayed in geographical coordinates.

7.3 Comparison With In-situ Data

After the velocity fields were generated for all pairs possible, the flow speeds could be calculated using Eq. 6.5 or Eq. 6.3. The flow speeds were then sampled along a line drawn between the sampling points shown in Figure 5.2 for comparisons with the in-situ data. The comparison between DInSAR - MAI and offset tracking flow speeds with the in-situ measurements could not be done one-to-one, as the in-situ measurements are yearly averages, while the DInSAR - MAI and offset tracking measurements covered time periods of only 14 days. In addition, the remote sensing measurements were in an azimuth - slant range coordinate system while the in-situ data was in geographical coordinates. The implications this had for the comparisons will be discussed in section 8.1. Nevertheless, the flow speed measurements could be used to determine if the acceleration of Kongsvegen seen in the in-situ data could be detected using the two different remote sensing techniques. Both the entire flow speed profiles and the average flow speed values were used for this purpose. The shapes of the measured flow speed profiles were also compared to the

shapes of the in-situ profiles, which could be used to verify the measured flow speeds to a certain degree.

The flow speed profiles produced from DInSAR - MAI for pairs 1, 2 and 4 and the in-situ data from 2017-2018 and 2018-2019 can be seen in Figure 7.16. As the DInSAR - MAI measurements contained some noise, they were filtered with a 5×5 moving average filter. The in-situ flow speed profiles show a characteristic bulge shape, highlighted in the gray region in Figure 7.16. This shape could to some degree also be seen in the profiles from pairs 1 and 4, but not from pair 2, as this profile was dominated by azimuth streaking. No comparison between the in-situ data and pairs 3 and 5-8 was made, as satisfactory results could not be obtained from InSAR or offset tracking from these pairs.

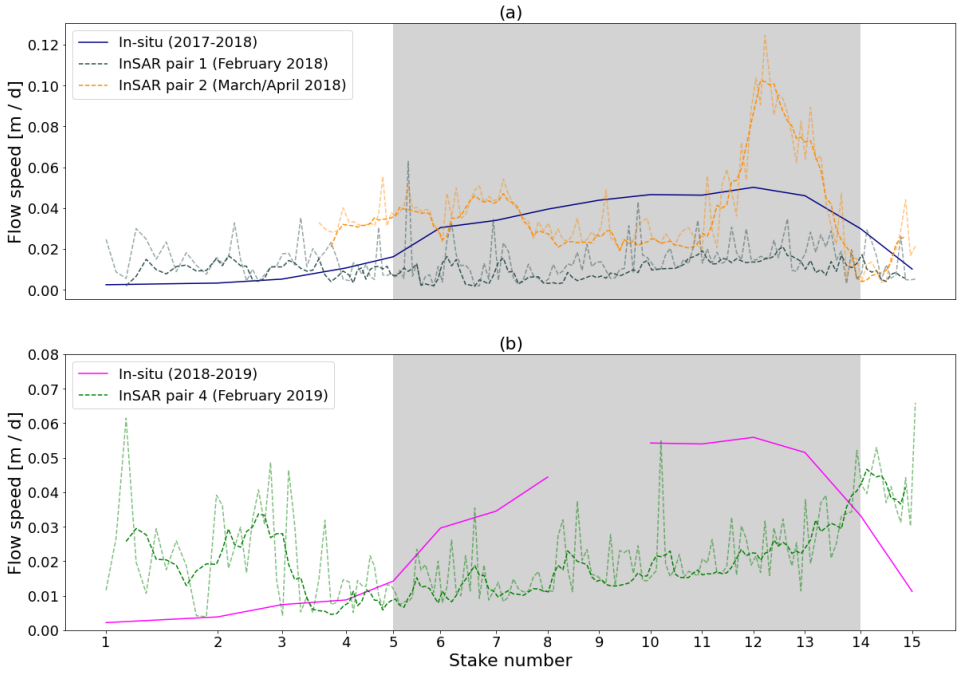

Figure 7.16: Flow speed profiles from the DInSAR-MAI combination filtered with a 5×5 moving average filter and in-situ data for the period 2017-2018 (a) and 2018-2019 (b). The unfiltered data is included as the translucent profiles. The gray region marks a characteristic increase in flow speed magnitudes in the in-situ profiles. Note the difference in the range of the y-axis for the figures.

In Table 7.2, the average flow speeds from the flow speed profiles measured with DInSAR - MAI and offset tracking can be found. Between pairs 1 and 4, which were acquired over the same region and with similar viewing geometry with one year separation (see Figure 5.2), an increase in the average flow speed can be seen. This is in agreement with the acceleration seen in the

in-situ measurements. The average flow speed from pair 2 was higher than the average flow speeds from pairs 1 and 4, likely a result of ionospheric streaking. This will be discussed further in section 8.1.3. Overall, the flow speed measurements from DInSAR - MAI and offset tracking indicates an acceleration on Kongsvegen.

Table 7.2: Flow speeds averaged over the sampling profile on Kongsvegen, ±1 SD $\left[\text{m d}^{-1}\right]$ for pairs 1, 2 and 4.

	Method	
Image Pair	InSAR	Offset Tracking
1	0.014 ± 0.009	0.030 ± 0.023
2	0.039 ± 0.022	0.087 ± 0.061
4	0.022 ± 0.012	0.049 ± 0.023

8

Discussion

This chapter contains two main sections. Section 8.1 contains an in-depth discussion of the results obtained from DInSAR, MAI and offset tracking and the comparison with the in-situ measurements. Particular attention will be given to the performance of DInSAR as this technique was the main focus of this study. In section 8.2, the sources of error in the measurements from DInSAR, MAI and offset tracking will be discussed. Limiting factors for the techniques will also be discussed.

8.1 Comparison Between Remote Sensing and In-situ Measurements

As the flow speed measurements from DInSAR - MAI and offset tracking were derived from azimuth - slant range measurements, they were not directly comparable to the in-situ data, which were measured in geographical coordinates. The evolution in time for the different measurements could however be compared, which was the main goal of this project. As the coherence was high for pairs 1, 2 and 4, the combination DInSAR - MAI could be used to estimate the velocity field and flow speeds on Kongsvegen successfully. The flow speeds measured with this combination can be seen in Figure 7.16. Pairs 1 and 4 were both acquired in February, from similar viewing geometries with one year separation. These pairs were therefore well suited for verifying the acceleration seen in the

in-situ measurements on Kongsvegen in recent years. The average in-situ flow speed increased from 0.028 ± 0.017 m d^{-1} in 2017-2018 to 0.029 ± 0.020 m d^{-1} in 2018-2019. The flow speeds from pair 4 were overall higher than the flow speeds from pair 1, which was in agreement with the evolution of the in-situ flow speeds. The average flow speed increased from 0.014 ± 0.009 m d^{-1} in February 2018 (pair 1) to 0.022 ± 0.012 m d^{-1} in February 2019 (pair 4). The higher SD for the measurements from pair 4 compared to pair 1 was likely due to the presence of azimuth streaking in this pair, which likely also accounted for some of the observed increase in average flow speed. Overall, the InSAR measurements from pairs 1 and 4 indicate a speed-up of Kongsvegen. An acceleration could also be seen in the offset tracking measurements from these pairs, where the average flow speed increased from 0.030 ± 0.023 m d^{-1} to 0.049 ± 0.023 m d^{-1}. The magnitudes of these measurements was however not in line with the in-situ and DInSAR - MAI measurements, as the average flow speeds from offset tracking were almost twice the magnitude of the DInSAR - MAI measurements, and exceeded the in-situ measurements as well. The SD of the offset tracking measurements was also larger than the SD of the in-situ and DInSAR - MAI measurements. This was likely caused by the presence of large spikes in the offset tracking flow speed profiles (Figure 7.11) which could be a result of mismatches.

It should be noted that the flow speeds measured from DInSAR - MAI were significantly lower than the in-situ measurements from the corresponding time periods (Figure 7.16). This was as expected, as the winter velocities on Kongsvegen are lower than the yearly average (see Figure 5.4), but the different coordinate systems of the measurements must also be taken into consideration for this. The characteristic bulge in the in-situ profiles (the gray region in Figure 7.16) could be observed in the smoothed DInSAR - MAI flow speed profile from pair 1 (Figure 7.16 (a)) to some degree, but not as distinct as in the in-situ measurements. The bulge also appeared to be present in the profile from pair 4 (Figure 7.16 (b)), but was obstructed by azimuth streaking in the uppermost part of the profile. The profile from pair 2 was dominated by azimuth streaking, except for the very uppermost section. As such, no bulge could be observed in this profile. The bulge was overall less distinct in the DInSAR - MAI profiles, which could indicate that the magnitude of the bulge relative to the remaining profile has a seasonal behaviour. Melvold et al. (1998) also found a seasonal variation in the shape of the flow speed profile on Kongsvegen, but this variation showed the opposite trend. In this study, the summer profile had a different shape than the annual profile, while the winter profile had a similar shape, only with lower magnitudes [57].

The in-situ measurements could also be seen as an upper limit for the DInSAR - MAI flow speed magnitudes. In regions affected by azimuth streaking, the flow speeds from pairs 2 and 4 exceeded the in-situ flow speeds. Flow speeds from

pair 1 were greater than the in-situ flow speeds near the front of Kongsvegen, which was a region of low coherence for this pair (see Figure 7.4 (a)). Apart from these low coherence regions, the DInSAR - MAI flow speed measurements did not exceed the in-situ flow speed measurements. This indicates that reasonable flow speed measurements can be made on Kongsvegen from DInSAR - MAI, given sufficiently high coherence.

The average flow speed from pair 2 was approximately twice the average flow speed from both pair 1 and 4 (see Table 7.2). This was likely caused by the significant amount of azimuth streaking present for this pair. The flow speed profile from pair 2 subsequently also showed greater magnitudes than the flow speeds from pairs 1 and 4 for most of the profile (see Figure 7.16), and even exceeded the in-situ measurements. At the uppermost section, from stake 14 and upwars, the flow speeds from pair 2 were however comparable to the flow speeds from pair 1. This region corresponded to the region of, low ionospheric interactions and subsequently high coherence for pair 2 (see Figure 7.5). This supports the claim that azimuth streaking was the cause of the high average flow speed for pair 2. The increase in average flow speed could also be explained by the difference in acquisition times for these pairs. Pair 2 was acquired in the March/April of 2018, while pairs 1 and 4 were acquired in February 2018 and 2019 respectively. As the average summer flow speeds from the in-situ data were higher than the average yearly flow speeds (Figure 5.4), an increase in flow speeds from winter to spring could be expected. Melvold et al. (1998) found that the increase in flow speeds on Kongsvegen had already begun in May, before the start of the melting season [57]. This further supports this claim. The magnitude of the increase is however not in line with this pattern, as the ratio between the spring 2018 flow speeds and winter 2018 flow speeds was ~ 2.79, which is approximately twice the ratio between the summer and annual flow speeds from the in-situ data (1.33 for 2018). This suggests that azimuth streaking was the dominant factor for the high average flow speed from pair 2. The uncertainty of these measurements was also high compared to the uncertainties from pairs 1 and 4 (see Table 7.2). Another contribution to the high average flow speed from pair 2 compared to pairs 1 and 4 could be that the flow speed profile from pair 2 did not cover the section near the front of Kongsvegen, where the flow speeds are generally the lowest.

A similar bulge as in the flow speed profile of Kongsvegen was found by Haga et al. (2021) on the Svalbard glacier Negribreen, which recently underwent a full surge cycle [73]. Prior to the surge, Negribreen was a slow moving glacier, with summer velocities in the range $0 - 0.2$ m d^{-1} and an almost stagnant front. The bulge was present prior to the phase leading up to the surge, but broke up as the surge initiated. This period was characterized by an increase in elevation over the bulge, and a decrease in elevation, accompanied by an increase in flow speeds, near the front. They also found that frontal flow speeds were

consistently high year round as the surge was initializing, indicating a change in flow speed dynamics. To evaluate if it could be expected that Kongsvegen follows a similar evolution during its surge cycle, the flow speed measurements could be combined with elevation data from the corresponding periods. If a similar pattern could be found from combining the flow speed measurements with elevation data, this could give an indication of how the surging event on Kongsvegen might proceed.

8.1.1 DInSAR Results

From the DInSAR profiles and corresponding coherence values (Figure 7.4 and Figure 7.5), good coherence was determined to be $\Delta\Omega > 0.4$. For the pairs with a temporal baseline of 14 days, the coherence was considered good for large parts of the images, except for pair 3 which had a coherence close to 0 for most of the scene. For the pairs with the longer temporal baselines (28 and 42 days) the coherence was significantly lower. There was therefore a significant amount of noise present in these DInSAR measurements (see Figure 7.7), and they were subsequently discarded from further interferometric analysis.

A wave-like structure could be seen in the DInSAR profiles, particularly from from pairs 1 and 4 (see Figure 7.16). This structure could also be observed in the uppermost part of the profile from pair 2, where the presence of noise was low (see Figure 7.6 (a)). As the same undulation was present in the profiles from both pair 1 and 4, it is unlikely that it was a result of ionospheric streaking. The wave-like structure could be related to the glacier bed topography, which can be seen in Figure 7.6 (b). While there were some peaks and bottoms in this profile that could account for some of the waviness, it did not match up completely with the flow speed profile. Another contribution to the undulation could be the relationship between the flow direction of Kongsvegen, the sampling points and the range direction. As Kongsvegen is not flowing in a straight direction, the slant range component of its velocity varies. As such, the amount of movement detected with DInSAR would vary. This is also a contributor to the significant bulge seen in the DInSAR measurements, as the range component for Kongsvegen is larger in the uppermost part (see Figure 7.3). The presence of noise in the profiles from pairs 5-8 made it impossible to determine if the wave-like structure could also be seen in these profiles. A higher frequency signal was however present in these profiles, which was likely an artifact introduced in the phase unwrapping.

The range direction for pairs 1, 2 and 4 was not ideal for DInSAR measurements on Kongsvegen, as the flow direction was almost parallel to the heading of the satellite in these scenes (see Figure 5.2). Pairs 5-8 had an ideal range direction for DInSAR measurements on Kongsvegen, but these were unfortunately not

usable for this purpose as a result of temporal decorrelation. The range direction in pairs 1 and 4 was however ideal for measurements on Kronebreen, where measurements could be made further up the glacier. This can be seen in Figure 7.3. Low velocities were however found near the front of Kronebreen, which was not in agreement with previous offset tracking studies made on this glacier [51] [56]. The reason for these low velocities was likely errors in phase unwrapping in this section, which was also observed in a previous InSAR study of Kronebreen by Eldhuset et al. (2003) [60]. This was further supported by the low coherence in this region (see Figure 7.2 (a) and (d)).

8.1.2 Offset Tracking Results

Overall, the performance of offset tracking on the 2018-2019 data was fairly good. As the coherence, and subsequently the temporal correlation, was high for pairs 1, 2 and 4, a patch size of 50×50 $\left(198 \times 362\,\mathrm{m}^2\right)$ could be used while still achieving a good coverage of matches. This patch size was relatively small compared to the patch size used for pairs 5-8, but large compared to patch sizes used in previous offset tracking studies [56]. The lack of features on Kongsvegen was likely the reason a large patch size was required to obtain a good coverage of matches. This resulted in flow speed and velocity maps with reasonably high spatial resolution. The measurements were also somewhat consistent with the DInSAR - MAI measurements, which will be discussed further in section 8.1.3.

Offset tracking was also attempted on pair 3, but was ultimately unsuccessful in retrieving satisfactory velocity measurements on Kongsvegen. This can be seen in Figure 7.12 (a). Similarly to the coherence image from pair 3, the quality of the matches were close to 0 for most of the scene (see Figure 7.12 (b)) except over bare ground. The performance was however better over Kronebreen, where a smooth flow speed image was obtained. This could be explained by the heavily crevassed front of Kronebreen, as the crevasses are prominent features which are largely unaffected by meteorological conditions, and as such could be tracked by the offset tracking algorithm. Such features are to a large degree absent from Kongsvegen, making its surface features more susceptible to meteorological interactions. This will be discussed further in section 8.2.4.

As the coherence was too low for InSAR to produce reasonable results on pairs 5-8, offset tracking was attempted as a means of retrieving flow speed measurements for these pairs. A large patch size was required to get a good coverage of matches over Kongsvegen on the pairs, due to temporal decorrelation. The need for a larger patch size for pairs 5-8 compared to pairs 1-4 could also be a result of the higher spatial resolution of these pairs. A larger patch size would

therefore be required to cover a sufficiently large region to contain significant surface features. For pairs 5-8, a patch size of 100×100 $(314 \times 844\,\mathrm{m}^2)$ was used. This resulted in a coarse flow speed map, but a reasonable coverage over Kongsvegen was achieved (see Figure 7.13). The measured flow speeds were however several orders of magnitude larger than the flow speeds from DInSAR - MAI and offset tracking on pairs 1, 2 and 4. These measurements were therefore discarded. As such, no flow speed measurements could be made from 2015. These measurements would have been useful for verifying the acceleration seen on Kongsvegen, as it had not yet initiated in 2015 (see Figure 5.4). While reasonable measurements could not be made on Kongsvegen from pairs 5-8, flow speeds that appeared to be in line with previous measurements near the front of Kronebreen $(\sim 1 - 3\,\mathrm{m\,d^{-1}})$ were made. This supports the claim that the lack of surface features on Kongsvegen was the reason behind the poor performance of offset tracking on pairs 5-8.

Reasonable results were also obtained on Aavatsmarkbreen from pairs 5-8, where an apparent deceleration throughout 2015 could be seen. As Aavatsmarkbreen had a surging event from 2013 to 2015, this deceleration is a result of the surging event ending. During the surge, flow speeds on Aavatsmarkbreen reached up to $\sim 5\,\mathrm{m\,d^{-1}}$ [74]. The deceleration is most clearly seen in pairs 5 and 8 (Figure 7.13 (a) and (d)). The flow speeds on Aavatsmarkbreen decreased dramatically between pair 5 (January/February 2015) and pair 8 (October/December 2015), from maximum values of $\sim 5\,\mathrm{m\,d^{-1}}$ to $< 2\,\mathrm{m\,d^{-1}}$.

8.1.3 Comparison Between DInSAR - MAI and Offset Tracking

Both DInSAR - MAI and offset tracking was applied to pairs 1, 2 and 4. This presented an opportunity to compare the performance of the two techniques. The offset tracking and DInSAR - MAI measurements were in good agreement for parts of the flow speed profile from pairs 1 and 4 (see Figure 7.11 (a) and (c)), but relatively high RMSE values were found for these pairs (0.028 and $0.033\,\mathrm{m\,d^{-1}}$ respectively). For pair 2, offset tracking produced significantly higher flow speed measurements than DInSAR - MAI for large sections of the flow speed profile. These were deemed to be erroneous measurements and subsequently removed (see Figure 7.11 (b)). This resulted in a higher RMSE value for pair 2 ($0.058\,\mathrm{m\,d^{-1}}$), approximately twice the RMSE for pairs 1 and 4. The difference between DInSAR - MAI and offset tracking was large for both pairs 1 and 4 near the front of Kongsvegen, where very high flow speeds $(> 0.1\,\mathrm{m\,d^{-1}})$ were measured from offset tracking.

Strozzi et al. (2008) observed that L-band offset tracking produced less accurate results than InSAR in regions where flow speeds were below $20\,\mathrm{m\,a^{-1}}$ $(\sim$

$0.05\,\mathrm{m\,d^{-1}}$) [9]. As the flow speeds on Kongsvegen are for the most part below this limit (see Figure 5.3), the poor performance of offset tracking compared to DInSAR - MAI over Kongsvegen was in agreement with this observation.

While being advantageous for InSAR, the slow movement and lack of surface features on Kongsvegen makes offset tracking challenging on this glacier. Finding matches proved to be particularly challenging in the middle part of Kongsvegen, which can be seen in Figure 7.10. In this part of Kongsvegen, several sections of missing data are present, which were a result of a lack of matches with sufficiently high quality (correlation between patches greater than 0). The quality of the matches was also low in this region for all pairs (Figure 7.14).

With offset tracking, it was possible to achieve a good coverage of matches near the front of Kronebreen, which was a region where InSAR failed to produce reasonable measurements (Figure 7.8). This illustrates how offset tracking and InSAR can complement each other, with InSAR being able to measure slower movement at a high spatial resolution and offset tracking being able to capture higher flow speeds, albeit at a coarser resolution. Similarly to Kongsvegen, in-situ measurements are being made regularly on Kronebreen by NPI. A more comprehensive, dedicated study of Kronebreen using a combination of DInSAR, MAI and offset tracking with ALOS-2 data could therefore be performed, with in-situ data as reference data. This would be useful for comparing the performance of the two techniques, but also for getting a better understanding of the flow dynamics of Kronebreen.

Another illustration of how InSAR and offset tracking can complement each other can be seen in the difference in the range of velocities measured by each method. The flow speeds from DInSAR - MAI ranged from $\sim 0 - 0.175\,\mathrm{m\,d^{-1}}$, while the flow speeds from offset tracking ranged from $\sim 0 - 4\,\mathrm{m\,d^{-1}}$. This shows how InSAR is limited to measuring slower movement than offset tracking, but can do so with better accuracy, as previously discussed.

8.2 Sources of Error and Limitations

In this section, the main sources of error in the flow speed measurements will be presented and discussed. The errors in the DInSAR measurements will be the main focus of this section, although MAI and offset tracking errors will also be discussed. Following this, the limitations of both DInSAR - MAI and offset tracking will be discussed.

8.2.1 Topographic Phase Errors

As an error was present in the topographic phase removal operator in SNAP, this step of the DInSAR processing chain was omitted. While the topographic phase contribution is small for repeat-pass interferometry, this introduces a source of error in the DInSAR measurements. The error consisted of a removal of topographic phase from a different area than what was covered by the interferogram. This is illustrated in Figure 8.1. An external topographic phase removal operator was not implemented as this would require radarcoding a DEM, which was beyond the scope of this study.

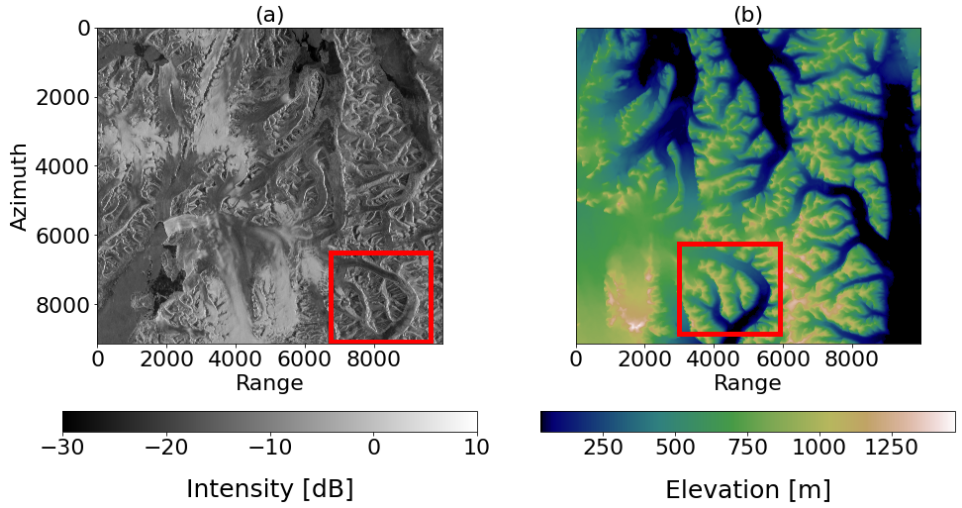

Figure 8.1: Multi-looked intensity image of the reference image on dB scale (a) and the topographic phase removed (b) from pair 4 (February 2019). The area marked by the red box highlights a distinct surface feature, from which it can be seen clearly that the two images do not cover the same region. The topographic phase is computed from the ArcticDEM [66] projected to WGS 84 (EPSG:4326). The images are multi-looked 2 times in azimuth and displayed in radar coordinates.

A rough estimate of the magnitude of the topographic phase component could however be made from Eq. 3.5 using values for the perpendicular baseline, which can be found in Table 5.2 and Table 5.3, the local incidence angle, $\theta(x, y)$ calculated in SNAP, as well as elevation data from a DEM. The elevation data used for estimating the topographic phase contribution for a pair was extracted from the region of the ArcticDEM [66] covered by that pair. The distance from the satellite to each scatterer in the scene was approximated as

$$\hat{R}(x, y) = H \cos\left(\theta(x, y)\right)$$

which assumes that all the scatterers in the scene are at the same distance to the satellite. In reality, this is not the case, but as the elevation differences in these scenes are on the order $10^0 - 10^3$ m while the altitude of the satellite is on the order 10^6 m, the differences in distance are negligible for this error assessment.

The estimated topographic phase contribution over Kongsvegen from pair 4 can be seen in Figure 8.2, displayed in m d^{-1}. A subset covering Kongsvegen was selected for this display to enhance the visibility of the error over this glacier, as it was the main focus of this project. The magnitude of the topographic phase contribution over Kongsvegen appears small from this estimate (< 0.01 m d^{-1}) for the most part, with a somewhat larger contribution in the uppermost section.

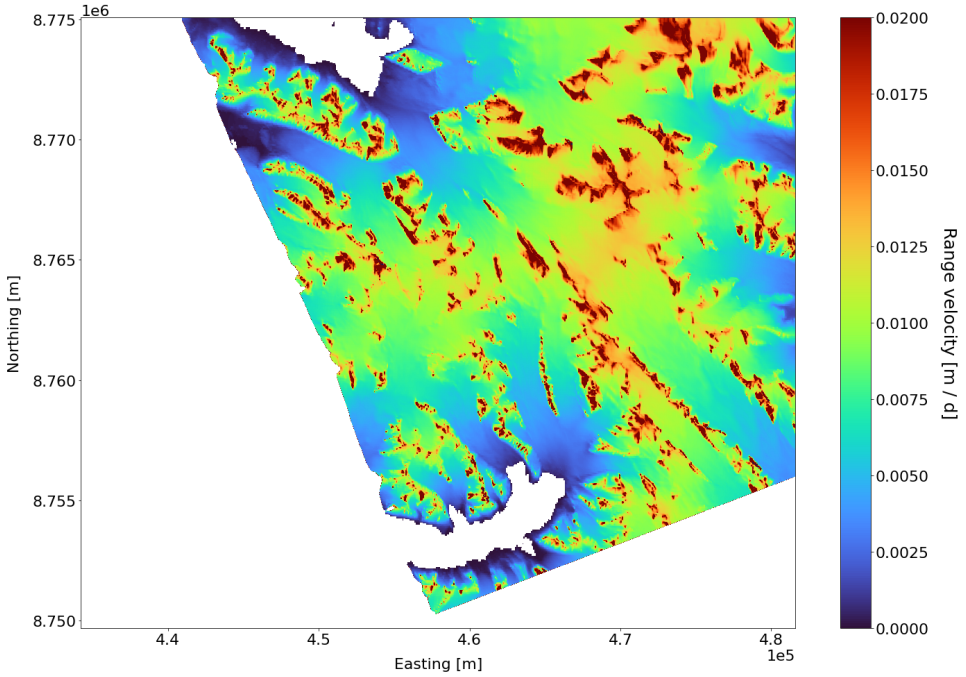

Figure 8.2: Estimated topographic phase contribution for a subset covering Kongsvegen from pair 4 (February 2019). A subset over Kongsvegen was used to enhance the visibility over this glacier. The image is displayed in geographical coordinates.

8.2.2 Ionospheric Interactions

In both the azimuth velocity component estimated from MAI (Figure 6.11) and the flow speed image from the DInSAR - MAI combination (Figure 7.8) for pair 4, the effects of azimuth streaking can be clearly seen. This effect was less

noticeable in the slant range velocity measurements from DInSAR for pair 4 (see Figure 7.3), but had a significant influence on the DInSAR profile from pair 2 (see Figure 7.5). The effect was more severe in the azimuth component as this was generated by splitting the bandwidth of the signal, making it sensitive to changes in the ionosphere occurring during acquisition of the image. As the interaction between the ionosphere and the radar pulses affects the travel time of the pulse, which is used for focusing in azimuth direction, this can cause misplacement of pixels in the images, causing decorrelation. In Figure 7.9, the direction of the velocity vectors was dominated by the azimuth streaking in the regions where this effect was present. The azimuth streaking can also be observed in the flow speed image from offset tracking (Figure 7.10), but not as significantly as in the flow speed image from DInSAR - MAI.

As previously mentioned, pair 2 was severely impacted by ionospheric disturbances. This resulted in a loss of coherence over several regions, which impacted the quality of the interferogram and caused artifacts in the unwrapped interferogram. This can be seen in Figure 8.3. An area of significant displacement in the unwrapped interferogram (Figure 8.3 (b)) is marked in red in all subfigures in Figure 8.3. The coherence in this region was close to zero, as can be seen in Figure 8.3 (a). From Figure 8.3 (c) it can be seen that for the most part this area is mountains and sea ice, which should not produce such a uniform region of displacement in the unwrapped interferogram. This displacement was therefore likely a result of unwrapping errors caused by phase decorrelation.

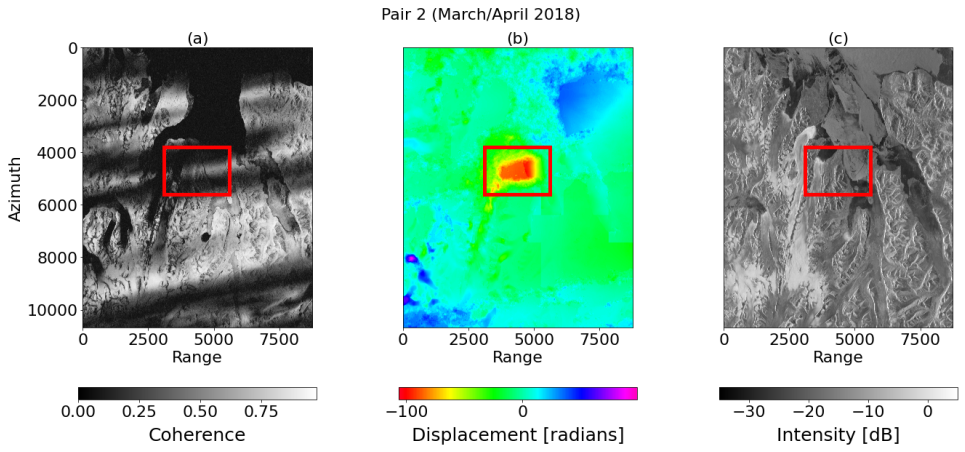

Figure 8.3: Coherence image (a), unwrapped interferogram with orbital correction (b) and the intensity image on dB scale (c), from pair 2 (March/April 2018). The red box highlights a region were a noticeable error in the unwrapping can be seen. The images are displayed in radar coordinates.

As pair 2 was acquired from a similar viewing geometry as pairs 1 and 4 (see Figure 5.2), only further south, the slant range velocity measurements from

pair 2 could be directly compared to the slant range velocity measurements from these pairs. In the regions with the lowest coherence in Figure 7.5 (a) (5 − 15 km from stake 1) the velocity measurements from pair 2 were significantly higher than the corresponding measurements from pairs 1 and 4. The shape of the profile from pair 2 also did not match the profile from pairs 1 and 4. These differences in velocity were therefore likely also a result of the phase decorrelation for pair 2 caused by ionospheric interactions.

8.2.3 Errors in Coregistration

By evaluating the displacement over stable ground from offset tracking, the accuracy of the coregistration was estimated (Figure 7.15). The median displacement over stable ground was used as the accuracy estimate, yielding a lower offset than the criterion for precise coregistration suggested by Zhou et al. (2009) [17]. In contrast, the average displacement over stable ground was almost an order of magnitude larger than this criterion, 0.874 ± 2.32 pixels, with an even larger SD. This was likely caused by errors in masking out moving features. The scale of Figure 7.15 ranges from 0 to over 20 pixels, but most of the data points are in the region < 1 pixels. The presence of these large displacements contributed to the large average pixel displacement. As this estimate was made on pair 4, the presence of azimuth streaking likely also influenced the average value. The median pixel displacement was therefore selected as the measure of coregistration accuracy, as this gave a more accurate representation of the pixel displacement over stable ground in the presence of the aforementioned outliers. The median pixel displacement was comparable to what was found by Strozzi et al. (2007), using L-band ALOS data covering arctic regions, including Svalbard [9]. They found a coregistration error of 1.17 ± 0.52 m when azimuth streaking was present but not compensated for. The median coregistration error was 0.071 pixels, which corresponds to ~ 0.561 m. This was deemed sufficiently accurate.

8.2.4 Meteorological Influence

The cause of the low coherence for pair 3 was likely warm temperatures or precipitation in the form of rain. From June 15th to June 28th 2018, there was a period of temperatures consistently above 0 °C in Ny-Ålesund. In this period there were also six precipitation events in the form of rain. Temperature and precipitation data from Ny-Ålesund can be seen in Figure 5.5. It is likely that Kongsvegen experienced similar meteorological conditions, as it is located in the vicinity of Ny-Ålesund. These meteorological factors therefore likely led to an increase in surface melt, which contributed to the low coherence for pair 3. This illustrates the limitations of InSAR during the summer melt season, due to

the sensitivity to changes in surface properties. Offset tracking is also sensitive to changes in surface properties, but if prominent surface features are present, measurements can still be made, as exemplified over Kronebreen.

8.2.5 Temporal Decorrelation

From Figure 6.2 it can be seen that the pairs from 2015 had significantly lower coherence values than the pairs from 2018-2019 (excluding pair 3 and the regions of pair 2 affected by azimuth streaking). This was likely a result of the larger temporal baseline for the 2015 data, which had 28 and 42 days separation compared to 14 days for the 2018-2019 data. As the temporal baseline increases, the likelihood of changes in the surface properties of scatterers increases. This leads to temporal decorrelation, which causes loss of coherence and phase stability. The low coherence of the 2015 greatly reduced the potential for successful phase unwrapping, and as such no InSAR measurements were made using the 2015 data.

Offset tracking also failed to produce reasonable results from these pairs. The changes in surface properties led to low quality of matches. While 28 and 42 days is a long temporal baseline for InSAR purposes, previous studies using L-band SAR data have obtained good results with even longer separation times between images [9]. The low coherence for these pairs can therefore not be attributed to the large separation in time between the acquisitions alone. While reliable measurements could not be made on Kongsvegen with these pairs, the measurements on Kronebreen and Aavatsmarkbreen were of high quality and in line with external measurements from these glaciers [56][74]. The lack of distinct surface properties of Kongsvegen was therefore likely a part of the reason why offset tracing failed for these pairs.

8.2.6 Orbital Errors

The residual flat Earth contribution in the interferograms is another potential another source of error in the velocity measurements. While these errors were compensated for by the linear spatial method described in section 3.4, residual errors not captured by this model could still be present. A more refined method, where both the coherence and elevation of the scene are included in the estimation of the ramp coefficients is described in [37]. This method would likely have produced better results in the orbital error correction, but was not implemented as this was beyond the scope of this study.

9

Conclusion

The main objective of this project was to investigate if the recent flow speed acceleration seen in the in-situ measurements on Kongsvegen also could be observed with remote sensing techniques. Three remote sensing methods for measuring surface displacement were used for this purpose, using 8 ALOS-2 image pairs from both ascending and descending orbits. The methods used were InSAR, MAI and offset tracking, with the results from InSAR being the main focus of this study. MAI was used to measure the azimuth velocity component, as InSAR is only sensitive in slant range direction, while offset tracking was mainly used for comparisons with the InSAR and MAI results. Offset tracking was also used as an alternative for measuring flow speeds in cases where InSAR failed to produce accurate results. In-situ data provided by NPI was used for comparisons with both the InSAR, MAI and offset tracking measurements were suitable.

For the 2018-2019 data, there was a 14 day difference in acquisition times. These pairs produced InSAR measurements with high coherence, and subsequently high phase stability, except for the pair that was acquired in June 2018. The high coherence meant that InSAR measurements could be made and thereby produce flow speed measurements with high spatial resolution and accuracy. Overall, high quality measurements were obtained with InSAR from these image pairs, apart from regions in the images affected by ionospheric disturbances of the SAR signals. This effect was most severe in the azimuth velocity measurements from MAI, but could also be observed in the DInSAR measurements in cases where the degradation was particularly strong. Offset tracking was also applied

to these pairs for comparing with the DInSAR - MAI results. The results from offset tracking and DInSAR - MAI were in fairly good agreement, although the offset tracking measurements had a significantly coarser resolution than both the InSAR and MAI measurements, which is inherent to the technique.

The pairs acquired in 2015 were acquired with longer separations in time, 28 days for pair 5 and 42 days for pairs 6-8. As a result, the coherence was significantly lower for these pairs and InSAR failed to produce useful results. Offset tracking was therefore attempted on these pairs as a means of retrieving velocity measurements, but this did not result in reasonable results on Kongsvegen from these pairs either. This could also be explained by the longer separation in time leading to the signals decorrelating. As such, no velocity measurements on Kongsvegen could be made from 2015. Reasonable offset tracking measurements could however be made on other glaciers within these scenes, suggesting that the lack of surface features on Kongsvegen was the cause of the low quality measurements.

The final conclusion from these results is that L-band InSAR could successfully be used to measure flow speeds on the slow moving glacier Kongsvegen, but a short separation in time between image acquisitions was required to avoid phase decorrelation. For answering the question whether the flow speed acceleration seen in the in-situ data could also be observed from remote sensing techniques applied to ALOS-2 data, more data would be needed. As the data from 2015 failed to produce satisfactory results, only results from the period 2018-2019 was in essence available. Pairs 1 and 4 were however acquired with one year separation, and could therefore to some extent be used to verify the acceleration seen in the in-situ data. An increase in flow speeds was observed between February 2018 and February 2019, with the averages along the InSAR profiles being 0.014 ± 0.009 m d^{-1} and 0.022 ± 0.012 m d^{-1} respectively. This is in agreement with the observed acceleration of Kongsvegen, but more InSAR measurements would be required to make a definitive conclusion from this method exclusively. Additionally, only measurements from pairs acquired in the winter/spring were available, resulting in significantly lower averages than the in-situ measurements, which were yearly averages. If more data from different periods of the year were available, this would have given a more complete picture of the evolution of flow speeds on Kongsvegen. Ideally, data from both ascending and descending orbits should have been available, as this would allow higher resolution and more accurate flow speed measurements and would have allowed the 3-D velocity field of the glacier flow to be derived. Data from a descending orbit would have been especially beneficial, as the flow direction of Kongsvegen is almost parallel to the azimuth direction for ascending passes, limiting the usefulness of DInSAR for this configuration.

9.1 Future Work

While the use of InSAR to measure flow speeds on Kongsvegen was successful, more data with a 14 day separation in time is required for a more thorough analysis of its flow dynamics. This would allow a more thorough investigation of the evolution of flow speeds on Kongsvegen to be made. It would also be beneficial to have data acquired from ascending and descending orbits from roughly the same time periods, to evaluate both range- and azimuth velocities using only DInSAR. While it certainly is possible to combine DInSAR with techniques such as MAI and offset tracking, these techniques produce measurements at a lower accuracy and spatial resolution than DInSAR. Having both the range and azimuth component from DInSAR would therefore allow measurements with high accuracy and resolution to be made. More data would therefore allow a more comprehensive study of the flow dynamics of Kongsvegen, and Svalbard glaciers in general, to be conducted.

A source of error in the DInSAR measurements made in this study was the presence of the topographic phase component. This signal was not removed, due to an error in the topographic phase removal operator in SNAP. For more precise InSAR measurements, this contribution must be removed. This would require removing the error in SNAP, but fixing this bug was beyond the scope of this project. Alternatively, a different InSAR software could be used.

Another source of error in the InSAR measurements was azimuth streaking as a result of ionospheric interactions. Designated methods for correcting these effects exists, but were not implemented in this study. Implementing and applying an azimuth streaking correction could improve the InSAR results, particularly from pairs 2 and 4. This would also be desirable if a more comprehensive study with more L-band data was to be conducted on Kongsvegen, as L-band signals are highly susceptible to ionospheric interactions.

Promising results were also obtained for other glaciers covered by the scenes, most notably Kronebreen. As regular in-situ measurements are also made on Kronebreen by NPI, this presents an interesting opportunity for evaluating the performance of ALOS-2 InSAR and offset tracking on a faster flowing glacier. These measurements could also be valuable for improving our understanding of the dynamics of Kronebreen.

Within this thesis L-band SAR images were used and proved that they could be used to measure displacement on a slow flowing glacier through the use of InSAR. Upcoming L-band missions include ALOS-4 Palsar-3 [75] (JAXA, to be launched in 2022), NASA-ISRO SAR (NISAR, to be launched in 2022) and ROSE-L (ESA, planned launched for 2028). Additionally, ALOS-4 and ALOS-2 are planned to be flown as a tandem mission, enabling also along-track

intereferometric measurements. As the main conclusion of this project was that L-band InSAR could successfully be used for measuring flow speeds on Kongsvegen, but that more data was required for a complete analysis, this could be enabled by the launch of these additional L-band SAR missions.

Bibliography

[1] M. Allen, P. Antwi-Agyei, F. Aragon-Durand, M. Babiker, P. Bertoldi, M. Bind, S. Brown, M. Buckeridge, I. Camilloni, A. Cartwright, *et al.*, "Technical summary: Global warming of 1.5° c. an ipcc special report on the impacts of global warming of 1.5° c above pre-industrial levels and related global greenhouse gas emission pathways, in the context of strengthening the global response to the threat of climate change, sustainable development, and efforts to eradicate poverty," 2019.

[2] Meredith, M., M. Sommerkorn, S. Cassotta, C. Derksen, A. Ekaykin, A. Hollowed, G. Kofinas, A. Mackintosh, J. Melbourne-Thomas, M.M.C. Muelbert, G. Ottersen, H. Pritchard, and E.A.G. Schuur, 2019: Polar Regions. In: IPCC Special Report on the Ocean and Cryosphere in a Changing Climate [H.-O. Pörtner, D.C. Roberts, V. Masson-Delmotte, P. Zhai, M. Tignor, E. Poloczanska, K. Mintenbeck, A. Alegría, M. Nicolai, A. Okem, J. Petzold, B. Rama, N.M. Weyer (eds.)]. In press.

[3] R. Hugonnet, R. McNabb, E. Berthier, B. Menounos, C. Nuth, L. Girod, M. Huss, D. Farinotti, I. Dussaillant, F. Brun, *et al.*, "Accelerated global glacier mass loss in the early twenty-first century," in *AGU Fall Meeting 2020*, 2020.

[4] T. A. Scambos, M. J. Dutkiewicz, J. C. Wilson, and R. A. Bindschadler, "Application of image cross-correlation to the measurement of glacier velocity using satellite image data," *Remote sensing of environment*, vol. 42, no. 3, pp. 177–186, 1992.

[5] T. Strozzi, A. Luckman, T. Murray, U. Wegmuller, and C. L. Werner, "Glacier motion estimation using sar offset-tracking procedures," *IEEE Transactions on Geoscience and Remote Sensing*, vol. 40, no. 11, pp. 2384–2391, 2002.

[6] R. M. Goldstein, H. Engelhardt, B. Kamb, and R. M. Frolich, "Satellite radar interferometry for monitoring ice sheet motion: application to an antarctic ice stream," *Science*, vol. 262, no. 5139, pp. 1525–1530, 1993.

[7] J. J. Mohr, N. Reeh, and S. N. Madsen, "Three-dimensional glacial flow and surface elevation measured with radar interferometry," *Nature*, vol. 391, no. 6664, pp. 273–276, 1998.

[8] A. Luckman, T. Murray, and T. Strozzi, "Surface flow evolution throughout a glacier surge measured by satellite radar interferometry," *Geophysical research letters*, vol. 29, no. 23, pp. 10–1, 2002.

[9] T. Strozzi, A. Kouraev, A. Wiesmann, U. Wegmüller, A. Sharov, and C. Werner, "Estimation of arctic glacier motion with satellite l-band sar data," *Remote Sensing of Environment*, vol. 112, no. 3, pp. 636–645, 2008.

[10] W. S. B. Paterson, *Physics of glaciers*. Butterworth-Heinemann, 1994.

[11] C. Elachi and J. J. Van Zyl, *Introduction to the Physics and Techniques of Remote Sensing*. John Wiley & Sons, 2 ed., 2006.

[12] J. B. Campbell and R. H. Wynne, *Introduction to Remote Sensing*. The Guilford Press, 5 ed., 2011.

[13] T. R. Lauknes, "Rockslide mapping in norway by means of interferometric sar time series analysis," 2011.

[14] D. Massonnet and K. L. Feigl, "Radar interferometry and its application to changes in the earth's surface," *Reviews of geophysics*, vol. 36, no. 4, pp. 441–500, 1998.

[15] `https://dragon3.esa.int/web/sentinel/user-guides/sentinel-1-sar/product-types-processing-levels/level-1`.

[16] A. Moreira, P. Prats-Iraola, M. Younis, G. Krieger, I. Hajnsek, and K. P. Papathanassiou, "A tutorial on synthetic aperture radar," *IEEE Geoscience and remote sensing magazine*, vol. 1, no. 1, pp. 6–43, 2013.

[17] X. Zhou, N.-B. Chang, and S. Li, "Applications of sar interferometry in earth and environmental science research," *Sensors*, vol. 9, no. 3, pp. 1876–1912, 2009.

[18] E. Rignot, K. Echelmeyer, and W. Krabill, "Penetration depth of interferometric synthetic-aperture radar signals in snow and ice," *Geophysical Research Letters*, vol. 28, no. 18, pp. 3501–3504, 2001.

[19] P. C. Dubois-Fernandez, J.-C. Souyris, S. Angelliaume, and F. Garestier, "The compact polarimetry alternative for spaceborne sar at low frequency,"

IEEE Transactions on Geoscience and Remote Sensing, vol. 46, no. 10, pp. 3208–3222, 2008.

[20] F. Filipponi, "Sentinel-1 grd preprocessing workflow," in *Multidisciplinary Digital Publishing Institute Proceedings*, vol. 18, p. 11, 2019.

[21] D. Small and A. Schubert, "Guide to asar geocoding," *ESA-ESRIN Technical Note RSL-ASAR-GC-AD*, vol. 1, p. 36, 2008.

[22] H. A. Zebker and R. M. Goldstein, "Topographic mapping from interferometric synthetic aperture radar observations," *Journal of Geophysical Research: Solid Earth*, vol. 91, no. B5, pp. 4993–4999, 1986.

[23] P. A. Rosen, S. Hensley, I. R. Joughin, F. K. Li, S. N. Madsen, E. Rodriguez, and R. M. Goldstein, "Synthetic aperture radar interferometry," *Proceedings of the IEEE*, vol. 88, no. 3, pp. 333–382, 2000.

[24] G. Moholdt and A. Kääb, "A new dem of the austfonna ice cap by combining differential sar interferometry with icesat laser altimetry," *Polar Research*, vol. 31, no. 1, p. 18460, 2012.

[25] `http://www.esa.int/esapub/tm/tm19/TM-19_ptA.pdf`.

[26] European Space Agency (ESA), "SNAP - ESA Sentinel Application Platform."

[27] Z. Li and J. Bethel, "Image coregistration in sar interferometry," *The International Archives of the Photogrammetry, Remote Sensing and Spatial Information Sciences*, vol. 37, pp. 433–438, 2008.

[28] D. O. Nitti, R. F. Hanssen, A. Refice, F. Bovenga, and R. Nutricato, "Impact of dem-assisted coregistration on high-resolution sar interferometry," *IEEE Transactions on Geoscience and Remote Sensing*, vol. 49, no. 3, pp. 1127–1143, 2010.

[29] M. Arikan, F. van Leijen, L. Guang, and R. Hanssen, "Improved image alignment under the influence of elevation," in *Proceedings of FRINGE*, 2007.

[30] `http://www.esa.int/esapub/tm/tm19/TM-19_ptB.pdf`.

[31] R. M. Goldstein and C. L. Werner, "Radar interferogram filtering for geophysical applications," *Geophysical research letters*, vol. 25, no. 21, pp. 4035–4038, 1998.

[32] W. Milczarek, A. Kopeć, and D. Głąbicki, "Estimation of tropospheric and ionospheric delay in dinsar calculations: case study of areas showing (natural and induced) seismic activity," *Remote Sensing*, vol. 11, no. 6, p. 621, 2019.

[33] D. Bekaert, R. Walters, T. Wright, A. Hooper, and D. Parker, "Statistical comparison of insar tropospheric correction techniques," *Remote Sensing of Environment*, vol. 170, pp. 40–47, 2015.

[34] J. Chen and H. A. Zebker, "Ionospheric artifacts in simultaneous l-band insar and gps observations," *IEEE transactions on geoscience and remote sensing*, vol. 50, no. 4, pp. 1227–1239, 2011.

[35] A. L. Gray, K. E. Mattar, and G. Sofko, "Influence of ionospheric electron density fluctuations on satellite radar interferometry," *Geophysical Research Letters*, vol. 27, no. 10, pp. 1451–1454, 2000.

[36] X. Tian, R. Malhotra, B. Xu, H. Qi, and Y. Ma, "Modeling orbital error in insar interferogram using frequency and spatial domain based methods," *Remote Sensing*, vol. 10, no. 4, p. 508, 2018.

[37] B. Xu, Z.-w. Li, Q.-j. Wang, M. Jiang, J.-j. Zhu, and X.-l. Ding, "A refined strategy for removing composite errors of sar interferogram," *IEEE Geoscience and Remote Sensing Letters*, vol. 11, no. 1, pp. 143–147, 2013.

[38] M. Shirzaei and T. R. Walter, "Estimating the effect of satellite orbital error using wavelet-based robust regression applied to insar deformation data," *IEEE transactions on geoscience and remote sensing*, vol. 49, no. 11, pp. 4600–4605, 2011.

[39] R. Bamler and P. Hartl, "Synthetic aperture radar interferometry," *Inverse problems*, vol. 14, no. 4, p. R1, 1998.

[40] C. W. Chen and H. A. Zebker, "Phase unwrapping for large sar interferograms: Statistical segmentation and generalized network models," *IEEE Transactions on Geoscience and Remote Sensing*, vol. 40, no. 8, pp. 1709–1719, 2002.

[41] `https://web.stanford.edu/group/radar/softwareandlinks/sw/snaphu/`.

[42] `https://web.stanford.edu/group/radar/softwareandlinks/sw/snaphu/snaphu_man1.html`.

[43] N. B. Bechor and H. A. Zebker, "Measuring two-dimensional movements using a single insar pair," *Geophysical research letters*, vol. 33, no. 16, 2006.

[44] U. Wegmuller, C. Werner, T. Strozzi, and A. Wiesmann, "Ionospheric electron concentration effects on sar and insar," in *2006 IEEE International Symposium on Geoscience and Remote Sensing*, pp. 3731–3734, IEEE, 2006.

[45] M. Debella-Gilo and A. Kääb, "Sub-pixel precision image matching for measuring surface displacements on mass movements using normalized cross-correlation," *Remote Sensing of Environment*, vol. 115, no. 1, pp. 130–142, 2011.

[46] K. Briechle and U. D. Hanebeck, "Template matching using fast normalized cross correlation," in *Optical Pattern Recognition XII*, vol. 4387, pp. 95–102, International Society for Optics and Photonics, 2001.

[47] P. Sánchez-Gámez and F. J. Navarro, "Glacier surface velocity retrieval using d-insar and offset tracking techniques applied to ascending and descending passes of sentinel-1 data for southern ellesmere ice caps, canadian arctic," *Remote Sensing*, vol. 9, no. 5, p. 442, 2017.

[48] T. Murray, T. Strozzi, A. Luckman, H. Jiskoot, and P. Christakos, "Is there a single surge mechanism? contrasts in dynamics between glacier surges in svalbard and other regions," *Journal of Geophysical Research: Solid Earth*, vol. 108, no. B5, 2003.

[49] I. Joughin, "Ice-sheet velocity mapping: a combined interferometric and speckle-tracking approach," *Annals of Glaciology*, vol. 34, pp. 195–201, 2002.

[50] J. Hu, Z. Li, X. Ding, J. Zhu, L. Zhang, and Q. Sun, "Resolving three-dimensional surface displacements from insar measurements: A review," *Earth-Science Reviews*, vol. 133, pp. 1–17, 2014.

[51] A. Luckman, D. I. Benn, F. Cottier, S. Bevan, F. Nilsen, and M. Inall, "Calving rates at tidewater glaciers vary strongly with ocean temperature," *Nature communications*, vol. 6, no. 1, pp. 1–7, 2015.

[52] `https://nsidc.org/cryosphere/glaciers/`.

[53] `https://www.nps.gov/glba/learn/nature/anatomy-of-a-glacier.htm`.

[54] W. R. Farnsworth, Ó. Ingólfsson, M. Retelle, and A. Schomacker, "Over 400 previously undocumented svalbard surge-type glaciers identified,"

Geomorphology, vol. 264, pp. 52–60, 2016.

[55] http://www.mosj.no/no/klima/land/massebalanse-isbreer.html.

[56] T. Schellenberger, T. Dunse, A. Kääb, J. Kohler, and C. H. Reijmer, "Surface speed and frontal ablation of kronebreen and kongsbreen, nw svalbard, from sar offset tracking," *The Cryosphere*, vol. 9, no. 6, pp. 2339–2355, 2015.

[57] K. Melvold and J. O. Hagen, "Evolution of a surge-type glacier in its quiescent phase: Kongsvegen, spitsbergen, 1964–95," *Journal of Glaciology*, vol. 44, no. 147, pp. 394–404, 1998.

[58] J. Hagen, K. Melvold, T. Eiken, E. Isaksson, and B. Lefauconnier, "Mass balance methods on kongsvegen, svalbard," *Geografiska Annaler: Series A, Physical Geography*, vol. 81, no. 4, pp. 593–601, 1999.

[59] C. Nuth, T. V. Schuler, J. Kohler, B. Altena, and J. O. Hagen, "Estimating the long-term calving flux of kronebreen, svalbard, from geodetic elevation changes and mass-balance modeling," *Journal of Glaciology*, vol. 58, no. 207, pp. 119–133, 2012.

[60] K. Eldhuset, P. H. Andersen, S. Hauge, E. Isaksson, and D. J. Weydahl, "Ers tandem insar processing for dem generation, glacier motion estimation and coherence analysis on svalbard," *International Journal of Remote Sensing*, vol. 24, no. 7, pp. 1415–1437, 2003.

[61] https://eoportal.org/web/eoportal/satellite-missions/a/alos-2.

[62] https://www.eorc.jaxa.jp/ALOS-2/en/calval/JAXA_PI_workshop_ALOS2CalVal_20180124.pdf.

[63] JAXA EORC and ALOS-2 Project Team, "Alos-2/palsar-2 calibration and validation results ver. 2021.1," tech. rep., 2021.

[64] Norwegian Polar Institute, "S100 raster," 1990.

[65] https://seklima.met.no/. Accessed 05/05-2021.

[66] P. Morin, C. Porter, M. Cloutier, I. Howat, M.-J. Noh, M. Willis, B. Bates, C. Willamson, and K. Peterman, "Arcticdem; a publically available, high resolution elevation model of the arctic," in *EGU General Assembly Conference Abstracts*, EGU General Assembly Conference Abstracts, pp. EPSC2016–8396, Apr. 2016.

[67] https://forum.step.esa.int/t/issues-in-topographic-phase-removal-using-external-dem/29655/17. Last accessed 20/04-2021.

[68] R. Natsuaki, H. Nagai, T. Motohka, M. Ohki, M. Watanabe, R. B. Thapa, T. Tadono, M. Shimada, and S. Suzuki, "Sar interferometry using alos-2 palsar-2 data for the mw 7.8 gorkha, nepal earthquake," *Earth, Planets and Space*, vol. 68, no. 1, pp. 1–13, 2016.

[69] Norwegian Polar Institute, "Kartdata svalbard 1:100 000 (s100 kartdata) / map data," 2014.

[70] T. Hollands, S. Linow, and W. Dierking, "Reliability measures for sea ice motion retrieval from synthetic aperture radar images," *IEEE Journal of selected topics in applied earth observations and remote sensing*, vol. 8, no. 1, pp. 67–75, 2014.

[71] T. Hollands and W. Dierking, "Performance of a multiscale correlation algorithm for the estimation of sea-ice drift from sar images: initial results," *Annals of Glaciology*, vol. 52, no. 57, pp. 311–317, 2011.

[72] M. Thomas, C. Kambhamettu, and C. A. Geiger, "Motion tracking of discontinuous sea ice," *IEEE transactions on geoscience and remote sensing*, vol. 49, no. 12, pp. 5064–5079, 2011.

[73] O. N. Haga, R. McNabb, C. Nuth, B. Altena, T. Schellenberger, and A. Kääb, "From high friction zone to frontal collapse: dynamics of an ongoing tide-water glacier surge, negribreen, svalbard," *Journal of Glaciology*, vol. 66, no. 259, pp. 742–754, 2020.

[74] I. Sobota, P. Weckwerth, and M. Nowak, "Surge dynamics of aavatsmarkbreen, svalbard, inferred from the geomorphological record," *Boreas*, vol. 45, no. 2, pp. 360–376, 2016.

[75] https://www.eorc.jaxa.jp/ALOS/en/ALOS-4/ALOS-4_top.htm. Accessed 30/05-2021.